The Dissertation Committee for Mir Mohammad Sadeghi Certifies that this is the approved version of the following dissertation:

Experimental and Theoretical Investigations of Thermal Transport in Graphene

Committee:

Li Shi, Supervisor

Jayathi Murthy

John Howell

Yaguo Wang

Deji Akinwande

Zhen Yao

Experimental and Theoretical Investigations of Thermal Transport in Graphene

by

Mir Mohammad Sadeghi, B.E.; M.E.

Dissertation

Presented to the Faculty of the Graduate School of

The University of Texas at Austin

in Partial Fulfillment

of the Requirements

for the Degree of

Doctor of Philosophy

The University of Texas at Austin

August 2015

To my parents

and

Maryam

Acknowledgements

First of all I would like to thank Professor Li Shi, my advisor, who guided me through the world of research and supported me during various stages of this work. He gave me the opportunity to explore the world of nanoscale science and technology. Also I would like to thank Professors Jayathi Murthy, John Howell, Yaguo Wang, Deji Akinwande, and Zhen Yao for serving on my committee and their valuable feedback on my dissertation.

I would like to thank my fellow lab members especially Jae Hun Seol, Michael Pettes, Insun Jo, Jaehyun Kim, Annie Weathers, and Xi Chen who made my experience in graduate school enjoyable by providing a friendly and collaborative working environment. I would like to thank Annie Weathers, Evan Fleming, and Sean Sullivan for useful comments on my dissertation draft. I also wish to thank the National Science Foundation and Nanomanufacturing Systems for Mobile Computing and Energy Technologies for their financial support. I am also thankful to the faculty and staff of the Center for Nanoscale and Molecular Science and Technology, Microelectronics Research Center, and Texas Advanced Computing Center at The University of Texas at Austin for providing the facilities to accomplish this research.

My infinite gratitude goes to my dear mother, for her unconditional love and support, and to the memory of my dear father who will always remain in my heart as someone who tried to give me the roots from which to grow and the wings to fly. Their sacrifices, devotions, and encouragement will always be appreciated. Finally, I would

like to express my special thanks and deep appreciation to my dear wife and my best friend, Maryam, for her endless love and support, and for the wonderful life that we share together. Without her sacrifices and devotions, I would not have been able to accomplish this much.

Experimental and Theoretical Investigations of Thermal Transport in Graphene

Mir Mohammad Sadeghi, Ph.D.

The University of Texas at Austin, 2015

Supervisor: Li Shi

Graphene has been actively investigated because its unique structural, electronic, and thermal properties are desirable for a number of technological applications ranging from electronic to energy devices. The thermal transport properties of graphene can influence the device performances. Because of the high surface to volume ratio and confinement of phonons and electrons, the thermal transport properties of graphene can differ considerably from those in graphite. Developing a better understanding of thermal transport in graphene is necessary for rational design of graphene-based functional devices and materials.

It is known that the thermal conductivity of single-layer graphene is considerably suppressed when it is in contact with an amorphous material compared to when it is suspended. However, the effects of substrate interaction in phonon transport in both single and multi-layer graphene still remains elusive. This work presents sensitive in-plane thermal transport measurements of few-layer and multi-layer graphene samples on amorphous silicon dioxide with the use of suspended micro-thermometer devices. It is

shown that full recovery to the thermal conductivity of graphite has yet to occur even after the thickness of the supported multi-layer graphene sample is increased to 34 layers, which is considerably thicker than previously thought. This surprising finding is explained by the long intrinsic scattering mean free paths of phonons in graphite along both the basal-plane and cross-plane directions, as well as partially diffuse scattering of phonons by the graphene-amorphous support interface, which is treated by an interface scattering model developed for highly anisotropic materials. In addition, an experimental method is introduced to investigate electronic thermal transport in graphene and other layered materials through the measurement of longitudinal and transverse thermal and electrical conductivities and Seebeck coefficient under applied electric and magnetic fields.

Moreover, this work includes an investigation of quantitative scanning thermal microscopy measurements of electrically biased graphene supported on a flexible polyimide substrate. Based on a triple scan technique and another zero heat flux measurement method, the temperature rise in flexible devices is found to be higher by more than one order of magnitude, and shows much more significant lateral heat spreading than graphene devices fabricated on silicon.

Table of Contents

List of Tables

List of Figures

Chapter 1: Introduction

1.1 BACKGROUND

Nanostructures have started to emerge in a wide range of scientific research fields and technological applications, as a result of recent advances in synthesizing and processing materials at nanoscale dimensions. Nanostructures have been extensively used or hold promises in integrated circuits, sensors, composites, and medicine, among others. In a number of these applications, such as thermal barriers, heat-assisted magnetic recording, high efficiency thermoelectrics, phase-change memory, and renewable energies, to name a few,[1-4] thermal transport properties of these nanostructures play an important role in the performance and reliability. In particular, another well-known example is electronic devices. As the semiconductor devices in integrated circuits become smaller and faster because of device miniaturization, power density increases and heat removal grows to be a primary issue in further device downscaling.[5-7]

As the size of structures shrinks toward the nanoscale regime and becomes comparable to the mean free path of energy or charge carriers (~10-100 nm), their transport properties are affected by scattering of the energy or charge carriers at the boundaries. However, the situation is different for two-dimensional graphene and one-dimensional carbon nanotubes (CNT) where the carriers move in the basal plane with a vanishing group velocity component along the cross-plane direction. Since the advent of mechanical exfoliation of graphene,[8] a two-dimensional sheet of sp^2-bonded carbon atoms in hexagonal structure, on a dielectric substrate many researchers have been intrigued by its exceptional electronic, mechanical, and thermal properties, based on

which a number of applications have been devised.[9,10] For example, graphene has been investigated as a potential candidate to replace the silicon active layers or metal interconnects in electronic devices.[11] The extreme thinness and very high mobility of graphene can result in high device speed.[10,11] Moreover, graphene is one of the strongest known materials,[12] can be stretched elastically by 20%,[13] and offers intrinsic thermal conductivity of ~3000 W m^{-1} K^{-1} at room temperature.[14,15] These exceptional properties have motivated researchers to incorporate graphene in a broad range of applications.[9,10,16]

The basal-plane thermal conductivity of freestanding single-layer graphene (SLG) is amongst the highest reported at room temperature.[14,15] However, the thermal conductivity of graphene supported on a SiO_2 substrate or in contact with an organic matrix is reduced well below the basal-plane value of high quality pyrolytic graphite.[17,18] It is suppressed even further when SLG or few-layer graphene (FLG) is encased between SiO_2 layers.[19] However, the thermal conductivity of supported SLG is still higher than all metals including copper and silver, and the thermal conductivity of encased FLG increases with increasing thickness. In suspended graphene, the suppression of thermal conductivity with increasing thickness has been explained based on the rapid expansion of the phase space for three-phonon scattering.[15] However, the mechanism for the thickness-dependence of the thermal conductivity of supported graphene has remained elusive and has been attributed to defects, substrate-induced roughness and stress, phonon leakage across the interface, or other phenomena such as modification of phonon dispersion.

In addition, there have been very few investigations on electronic thermal transport in graphene. The electronic thermal conductivity is often neglected as compared

to the lattice thermal conductivity in graphene. Upon the application of a gate field, however, the electronic contribution to thermal transport in graphene can increase considerably with increasing charge carrier concentration and can become a significant component. Moreover, thermal energy in electronic devices may be transferred by hot carriers that are not in equilibrium with the lattice.[20,21]

Despite the rich physics behind the basal-plane thermal conductivity of graphene, this property is not the only factor that influences the operating temperature of graphene electronic devices. Besides the interfacial thermal conductance of graphene, the thermal conductivity of the supporting dielectric layer or substrate can dominate the temperature rise in operating graphene electronic devices. In particular, graphene has received increasing interest for use in flexible electronic devices fabricated on a flexible substrate.[16,22-24] Compared to silicon substrates, the very low thermal conductivity of the flexible substrate is expected to increase the operating temperature of the graphene device and may lead to distinct heat dissipation pathways. Coupled with the relatively low glass transition temperature of flexible substrates, the high operating temperature can result in thermomechanical failure of the flexible graphene electronic devices.

Mapping the temperature distribution with high spatial resolution on operating nanoelectronic devices can provide useful insights into the device performance and reliability. A number of optical and scanning probe microscopy methods have been developed for high-resolution mapping of the temperature distribution in electronic devices.[3,25] In recent years, these techniques have been employed to reveal coupled electro-thermal phenomena in carbon nanotube and graphene electronic devices fabricated on a silicon substrate.[26-30] However, the temperature distribution on flexible

graphene devices have remained elusive, despite more significant thermomechanical reliability issues expected in flexible graphene devices than in devices fabricated on silicon. The lack of such experimental data is associated with additional challenges present in high-resolution thermal mapping of flexible graphene devices with a high temperature rise and large heated area.

1.2 SCOPE OF WORK

The aim of this work is to establish a better understanding of thermal transport in supported graphene. A combination of experimental and theoretical approaches are developed to investigate the basal-plane thermal conductivity in supported graphene and to probe the temperature distribution on electrically biased graphene devices, especially graphene devices fabricated on a flexible substrate.

Chapter 2 reports on experimental and theoretical investigations of the thickness-dependence of the basal-plane thermal conductivity of supported graphene. Graphene samples are obtained by exfoliation of natural graphite flakes. With the use of suspended micro-thermometer devices, the thermal conductivity of the graphene samples are measured and compared to the measured thermal conductivity of the graphite sample used as the source for the exfoliation. The measurement results show a trend of increasing thermal conductivity with thickness as the thickness increases from 1 to 34 layers. These results are analyzed by examining various potential mechanisms for thermal conductivity suppression in supported graphene, and extracting the in-plane and cross-plane mean free path of phonons in graphite based on the graphite thermal conductivity, and calculating the phonon transmission coefficient at the interface between graphene or

graphite and SiO_2 based on the reported values for interface thermal conductance. Furthermore, a theoretical model is developed to investigate phonon-interface scattering in highly anisotropic materials. Such a comparison between the measurement results and theoretical calculation is used to explain the phonon transport in multi-layer graphene supported on an amorphous support.

Chapter 3 reports the exploration of an experimental approach that can be used to probe electronic thermal transport in graphene and other layered materials. Suspended micro-thermometer devices are designed and fabricated to measure longitudinal and transverse thermal conductivity, longitudinal and transverse electronic conductivity, and Seebeck coefficient in a supported graphene sample in presence of a perpendicular magnetic field. Thermogalvanomagnetic effects are also investigated by measuring the transverse electrostatic potential or temperature gradient caused by longitudinal electric current or heat flow and a perpendicular magnetic field. An attempt is made to employ these measurements to investigate the electronic thermal conductivity and Seebeck coefficient in a bilayer graphene sample.

Chapter 4 reports an investigation on high-resolution, quantitative scanning thermal microscopy (SThM) measurements of flexible graphene devices. Challenges of performing quantitative SThM measurements are discussed and the effect of parasitic heat transfer through the air conduction is eliminated by a triple scan technique. The SThM measurement is calibrated by performing SThM measurements on a heater-thermometer metal line. The accuracy of the calibrated SThM measurements is investigated by a detailed discussion of the measurement parameters and the measured thermal resistance of the liquid meniscus at the tip-device contact area as a function of

temperature. In addition, a laser-heated SThM method is introduced as a measurement technique to obtain quantitative temperature measurements under zero heat transfer across the tip-sample contact. The triple-scan SThM and laser-heated SThM methods are employed to study the thermal response of flexible graphene devices on polyimide substrates.

The major findings of this work are summarized in Chapter 5.

Chapter 2: Experimental and Theoretical Investigation of Thickness-Dependent Thermal Conductivity of Supported Graphene†

2.1 INTRODUCTION

Graphene, a monoatomic layer of carbon atoms arranged in a hexagonal lattice, is the building block of graphite and carbon nanotubes (CNTs), which can be envisioned as a stack of a large number of graphene layers and rolled up cylinders of graphene sheets, respectively. Thermal transport in these graphitic materials has intrigued researchers for several decades. The industrial use of graphite in high-temperature or high-heat flux applications motivated a number of initial studies on its thermal properties. These studies have found highly anisotropic thermal transport properties in graphite, where the basal-plane thermal conductivity is among the highest found in solids and nearly two orders of magnitude larger than the value measured along the c-axis.[31-33] The recent rediscoveries of CNTs and single-layer graphene (SLG) have expanded the applications of these graphitic nanomaterials for electronic devices, sensors, and light-weight composite materials, among others.[9,34] The performance and reliability of CNT and graphene devices are often closely related to the thermal properties of these nanoscale building blocks, similar to the situation in silicon nanoelectronic devices where localized heating

† Reproduced in part with permission from Sadeghi, M. M., Jo, I. & Shi, L. Phonon-Interface Scattering in Multilayer Graphene on an Amorphous Support. *Proc Natl Acad Sci USA* **110**, 16321-16326 (2013). Copyright 2013 National Academy of Sciences of the United States of America. M.M.S. and L.S. designed research and developed theoretical analysis; M.M.S. carried out measurements and performed theoretical calculations; I.J. performed density functional theory calculations; M.M.S. and L.S. analyzed data and wrote the paper.

has become a major challenge.[35] Hence, there have been a number of studies of thermal transport in these carbon nanostructures. Some of the studies have yielded higher thermal conductivity values in suspended CNTs and graphene than the largest reported graphite value.[36,37] Because of the ultrahigh thermal conductivity and the large surface to volume ratio, there have been a large number of efforts in the development of thermal management materials utilizing these carbon nanomaterials.[14,38] However, in most of these applications, graphene and CNTs are either supported on a substrate or embedded in a medium, instead of being suspended. Hence, the effect of interface interaction on phonon transport in and across graphene and CNTs must be understood.

Recently, it has been found that the basal-plane thermal conductivity of SLG or bilayer graphene (BLG) in contact with an amorphous inorganic or organic layer is a factor of three to five lower than those found in high-quality graphite and suspended graphene at room temperature.[17,18] The suppression has been attributed to interface scattering or damping of phonons in graphene, especially the flexural modes that may make a large contribution to the basal-plane thermal conductivity in suspended graphene.[39] Another measurement of few-layer graphene (FLG) encased in amorphous oxide has yielded decreasing basal plane thermal conductivity with decreasing FLG layer thickness,[19] opposite to the finding for suspended FLG.[15,37] However, the uncertainty in the experimental data makes it difficult to determine accurately the layer thickness needed for the encased FLG to recover the basal plane thermal conductivity of graphite. Better understanding of this layer thickness dependence is needed for sensible design of FLG lateral heat spreaders for high-power density nanoelectronic devices and high-surface area FLG fillers to enhance the thermal conductivity of polymeric composites,

among other applications. In addition, there remain questions regarding whether the thermal conductivity reduction is mainly caused by transmission or leakage of phonons across the interface,[17,40] phonon scattering by interface roughness,[17,19] or defects created in the FLG in the sample fabrication processes.[14,19]

Molecular dynamics (MD) simulations have provided insights into the effects of interface interactions on phonon transport in graphene. For instance, MD results have verified that flexural phonons make an important contribution to the thermal conductivity in suspended graphene, and this contribution is considerably suppressed by an amorphous support.[41-43] In addition, a recent MD simulation has shown increasing thermal conductivity with increasing layer thickness of FLG supported on amorphous SiO_2.[43] The results suggest a rapid increase of the basal-plane thermal conductivity to approach 90% of the graphite value when the FLG thickness increases to about 6 layers. However, the accuracy in classical MD simulation results has been limited by the lack of effective quantum correction methods and high-fidelity interatomic potentials for graphitic systems,[44] where the specific heat is still considerably lower than the classical Dulong and Petit limit even at room temperature because of high Debye temperature of graphite. In addition, although one reported MD simulation suggests such role is negligible for a single-wall CNT supported on an amorphous support,[45] the role of phonon leakage[17,40] across the interface in the thermal conductivity of supported graphene remains to be elusive.

2.1.1 Present Work

To clarify these outstanding questions, here we report results from temperature-dependent thermal conductivity measurements of FLG and multi-layer graphene (MLG) supported on SiO_2 and the natural graphite (NG) source used to exfoliate the FLG and MLG samples. Compared to the measurement values for encased FLG[19] and MD simulation data for supported FLG,[43] the measurement results suggest a rather gradual convergence of the MLG basal-plane thermal conductivity to the graphite value when the MLG layer thickness is increased, especially at low temperatures. A shift of the peak thermal conductivity towards a higher temperature is observed in the thinner supported MLG samples. Accounting for the highly anisotropic phonon dispersion in MLG, solutions of phonon Boltzmann Transport Equation (BTE) are developed to analyze the measurement results of the basal plane thermal conductivity and interface thermal conductance of MLG on an amorphous oxide support and the anisotropic thermal conductivities of graphite. Based on the analysis, the observed gradual convergence and peak shift can be well explained by long intrinsic phonon scattering mean free paths in graphite and partially diffuse phonon-interface scattering in the supported MLG. Moreover, such partially diffuse interface scattering process is influenced by a rather large transmission component, especially for low-frequency phonons which provide a large contribution to the peak thermal conductivity of graphite at low temperatures and possess high interface transmission coefficient in supported graphene.

2.2 EXPERIMENTAL METHODS

2.2.1 Thermal Conductance Measurement using Symmetric Micro-Thermometer Devices

Thermal conductivity of graphene samples with thickness of less than few layers are measured using suspended resistance thermometer devices following a method reported for measuring thermal conductivity of single-layer graphene (SLG).[17] In this method, the resistance thermometer (RT) lines are symmetrically designed and their thermal conductance values are assumed to be similar for the analysis of the measurement results. Schematics of a symmetric device are shown in Figure 2.1(a,b). For the measurement, a direct current is passed through RT_1, which generates heat at the rate of Q_1 and induces temperature gradients all over the device. The average temperature of RT_i changes by $\overline{\Delta T_i}$ which can be measured through the known correlation between temperature and resistance of the RT lines. Based on the corresponding thermal circuit model shown in Figure 2.1(c) and a one-dimensional solution of thermal conduction in RT_1, the thermal conductance of the RT lines (R_b) and thermal conductance of the FLG/SiO_2 bridge (R_s) can be measured according to [17]

$$R_b = 2(\Delta T_{1m} + \Delta T_{2m} + \Delta T_{3m} + \Delta T_{4m}){Q_1}^{-1} \quad (2\text{-}1)$$

$$R_s = R_b(\Delta T_{2m} - \Delta T_{3m})(\Delta T_{3m} + \Delta T_{4m})^{-1} \quad (2\text{-}2)$$

where

$$\Delta T_{1m} = \frac{3}{2}\overline{\Delta T_1} - \frac{1}{2}\left(\overline{\Delta T_2} + \overline{\Delta T_3} + \overline{\Delta T_4}\right) \quad (2\text{-}3)$$

$$\Delta T_{im} = 2\overline{\Delta T_i} \quad ; \; i = 2,3,4 \quad (2\text{-}4)$$

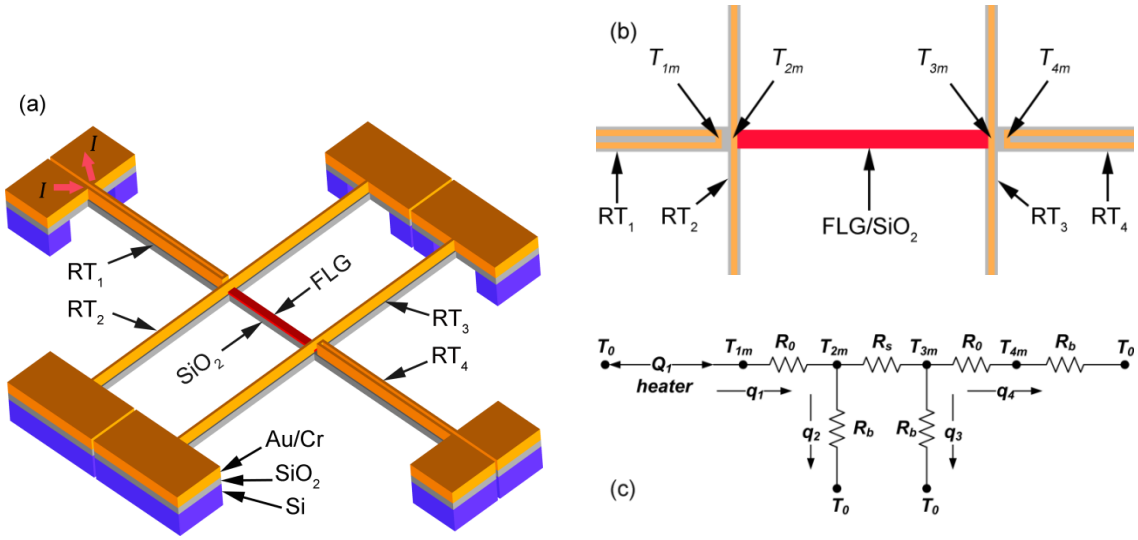

Figure 2.1: Symmetric resistance thermometer device. Schematic of the device (a), top view of the central bridge (b), and the corresponding thermal circuit model (c) when RT_1 is used as the heater line. R_b and R_s are the thermal resistances of the RT_i beams and the center FLG/SiO_2 bridge, respectively. T_{im} and q_i are the midpoint temperature of the metal line and the heat flow through RT_i when RT_1 is electrically heated at a rate of Q_1, respectively, where the subscript i is 1, 2, 3, or 4. T_0 is the ambient temperature. R_0 is the thermal resistance between the midpoints of RT_1 and RT_2 and that between RT_3 and RT_4. The dimensions are not to scale.

After the thermal conductance of the FLG/SiO_2 bridge is measured over the desired temperature range, the FLG sample is etched away in oxygen plasma and the measurement is repeated to obtain thermal conductance of the SiO_2 bridge. The thermal conductance of the FLG sample (G) is obtained as the difference between the thermal conductance of the SiO_2 bridge and the thermal conductance of the FLG/SiO_2 bridge. The

thermal conductivity of the supported FLG is obtained as $\kappa = GL/Wt$, where L, W, and t are the length between the two straight RT_2 and RT_3, width, and thickness of the FLG sample.

2.2.2 Thermal Conductance Measurement using Non-Symmetric Micro-Thermometer Devices

Although the device fabrication is based on those reported by Seol et al.[17] for thermal measurements of supported SLG samples, several notable changes have been made in the device design and measurement procedure in order to further reduce the relative error caused by contact thermal resistance, which is expected to increase with the MLG layer thickness. As shown in Figure 2.2(a,b,c), the area for heat transfer across the two ends of the MLG ribbon is increased by extending each end of the MLG ribbon by 20 μm into the region between the straight RT line and the adjacent U-shape RT line. The ends are also clamped between a top Cr/Au metal layer and the underlying SiO_2 beam to allow for heat conduction into all surfaces of the MLG ribbon at the two ends. In addition, the error caused by the contact thermal resistance can be further reduced by increasing the thermal resistance of the two straight resistance thermometer (RT) lines relative to the contact thermal resistance between these two temperature sensors and the MLG sample. These two RTs are used for measuring the temperature drop along the central MLG/SiO_2 beam. The thermal resistance of these two straight RT lines can be increased to be larger than that of the U-shape RTs by more than an order of magnitude by decreasing the width and increasing the length of the straight RTs.

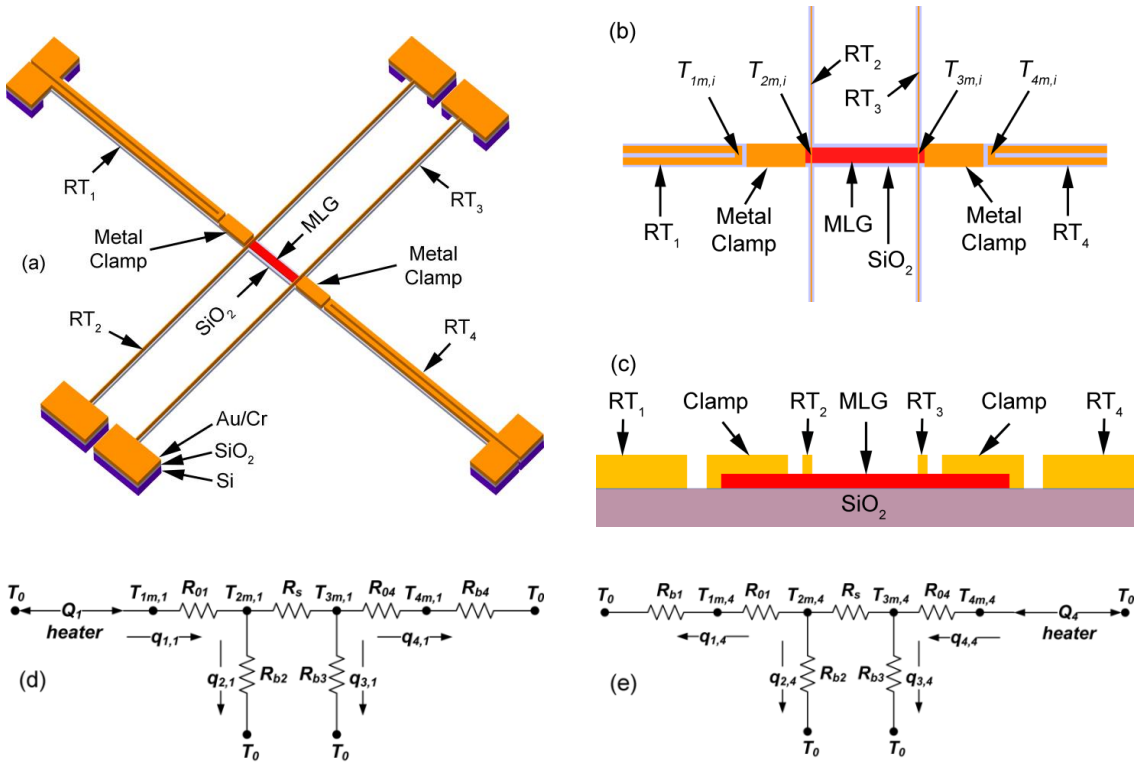

Figure 2.2: Non-symmetric resistance thermometer device. Schematic of the device (a), top view (b) and cross section (c) of the central bridge. The corresponding thermal circuit model when RT_1 (d) or RT_4 (e) is used as the heater line. R_{bi} and R_s are the thermal resistances of the RT_i beam and the center MLG/SiO_2 bridge, respectively. $T_{im,j}$ and $q_{i,j}$ are the midpoint temperature of the metal line and the heat flow through RT_i when RT_j is electrically heated at a rate of Q_j, respectively, where the subscripts i and j are 1, 2, 3, or 4. T_0 is the ambient temperature. R_{01} and R_{04} are the thermal resistances between the midpoints of RT_1 and RT_2 and that between RT_3 and RT_4, respectively. The dimensions are not to scale.

In addition, a measurement technique has been established in this work to measure the thermal conductance values of suspended beams of a non-symmetric suspended device without needing to assume device symmetry. In the schematic of a non-symmetric micro-thermometer device shown in Figure 2.2(a,b,c), the four RT lines are referred as RT_1, RT_2, RT_3, and RT_4 in a left-to-right order. The corresponding thermal circuit model is shown in Figure 2.2(d,e). In the measurement of Seol et al.,[17] the measurement device was assumed to be symmetric. Here, this assumption is removed, so there are seven unknown thermal resistances in the thermal circuit.

During the thermal measurement, the sample is placed in the evacuated sample space of a cryostat. To obtain the seven thermal resistances, one outer U-shape metal line (RT_1) is electrically heated at different rates (Figure 2.2(d)), and the electrical resistances of the four RT lines are measured and used to obtain the average temperature rises in the metal lines. Subsequently, the measurement is repeated by using the other U-shape metal line (RT_4) as the heater line (Figure 2.2(e)). The two measurements generate eight sets of data relating the average temperature rise in each metal line RT_i, $\overline{\Delta T_{i,j}}$, to the heating power in one of the two U-shape lines, RT_j. When there is no heat generation in a metal line, $\Delta T_{im,j} = 2\,\overline{\Delta T_{i,j}}$ where $\Delta T_{im,j}$ is the corresponding temperature rise at the midpoint of the metal line of RT_i. Based on the thermal circuit model and heat conduction analysis of the heater line,[46] all seven thermal resistances shown in Figure 2.2(d,e) can be determined from the measured data:

$$R_{b1} = 6\left(2(\alpha_1 + 1)\overline{\Delta T_{1,1}} - \alpha_1 \Delta T_{2m,1}\right)(\alpha_1 + 4)^{-1} {Q_1}^{-1} \tag{2-5}$$

$$R_{01} = {\alpha_1}^{-1} R_{b1} \tag{2-6}$$

$$R_{b4} = 6\left(2(\alpha_2 + 1)\overline{\Delta T_{4,4}} - \alpha_2 \Delta T_{3m,4}\right)(\alpha_2 + 4)^{-1} {Q_4}^{-1} \quad (2\text{-}7)$$

$$R_{04} = {\alpha_2}^{-1} R_{b4} \quad (2\text{-}8)$$

$$R_s = R_{01}\left(\frac{\Delta T_{3m,4}}{\Delta T_{2m,4}} - \frac{\Delta T_{3m,1}}{\Delta T_{2m,1}}\right)\left(\frac{\Delta T_{1m,1}}{\Delta T_{2m,1}} - \frac{\Delta T_{1m,4}}{\Delta T_{2m,4}}\right)^{-1} \quad (2\text{-}9)$$

$${R_{b2}}^{-1} = {R_s}^{-1}\frac{\left(\Delta T_{3m,1} - \Delta T_{2m,1}\right)}{\Delta T_{2m,1}} - {R_{01}}^{-1}\frac{\left(\Delta T_{2m,1} - \Delta T_{1m,1}\right)}{\Delta T_{2m,1}} \quad (2\text{-}10)$$

$${R_{b3}}^{-1} = {R_s}^{-1}\frac{\left(\Delta T_{2m,1} - \Delta T_{3m,1}\right)}{\Delta T_{3m,1}} - {R_{04}}^{-1}\frac{\left(\Delta T_{3m,1} - \Delta T_{4m,1}\right)}{\Delta T_{3m,1}} \quad (2\text{-}11)$$

where

$$\alpha_1 = \frac{\Delta T_{1m,4}}{\left(\Delta T_{2m,4} - \Delta T_{1m,4}\right)} \quad (2\text{-}12)$$

$$\alpha_2 = \frac{\Delta T_{4m,1}}{\Delta T_{3m,1} - \Delta T_{4m,1}} \quad (2\text{-}13)$$

$$\Delta T_{1m,1} = 2\overline{\Delta T_{1,1}} - \frac{Q_1}{6G_{b1}} \quad (2\text{-}14)$$

2.2.3 Exfoliation and Layer-Counting of Graphene Samples

Graphene samples are obtained by exfoliation of natural graphite flakes (NGS Naturgraphit GmbH) onto a Si substrate covered by ~290 nm thermally-grown SiO_2 using the scotch-tape method.[8] Thin graphitic flakes are located using an optical microscope based on the color contrast.[47] Raman spectroscopy is used to distinguish single-layer and bilayer graphene flakes based on the shape and linewidth of the 2D peak.[48,49] For FLG and multi-layer graphene (MLG) samples, the layer number is

determined using a combination of Raman spectroscopy and atomic force microscopy (AFM). After exfoliated on SiO_2, the original flake for the MLG samples often contains a SLG or BLG edge based on Raman spectra. AFM is used to measure the step height between the edge and the rest of the flake. Based on the interlayer spacing of 3.35 Å of graphite, this combined measurement is used to determine the layer thickness of the MLG. In addition, the ratio of the G peak intensity of the flake to that of the adjacent SLG or BLG is used to re-measure the thicknesses for the flakes thinner than 10 layers.[50,51]

2.2.4 Micro-Thermometer Device Fabrication

As described in section 2.2.3, the layer number of graphene samples is determined using a combination of Raman spectroscopy and AFM. The fabrication process for an 8-layer graphene sample (G8) is shown in Figure 2.3. The edge of the exfoliated graphene is trimmed using oxygen plasma to pattern the graphene into the desired shape. Resistance-thermometer metal lines and metal contacts are fabricated through electron-beam lithography (EBL) process with poly(methyl methacrylate) (PMMA) resist followed by e-beam evaporation of Au with Cr adhesion layer and a lift-off process in acetone. Using another EBL process, windows are opened in the PMMA resist and the graphene flake is further trimmed using oxygen plasma to etch the unwanted connections. Subsequently, Zep 520A is spin-coated on the substrate and patterned using EBL. The pattern is transferred through the SiO_2 layer using a reactive ion etching (RIE) process with CF_4 gas. The SiO_2 beams of the measurement device are designed to be at an angle to the (111) etching stop plane of Si, so that the silicon underneath the beams could be

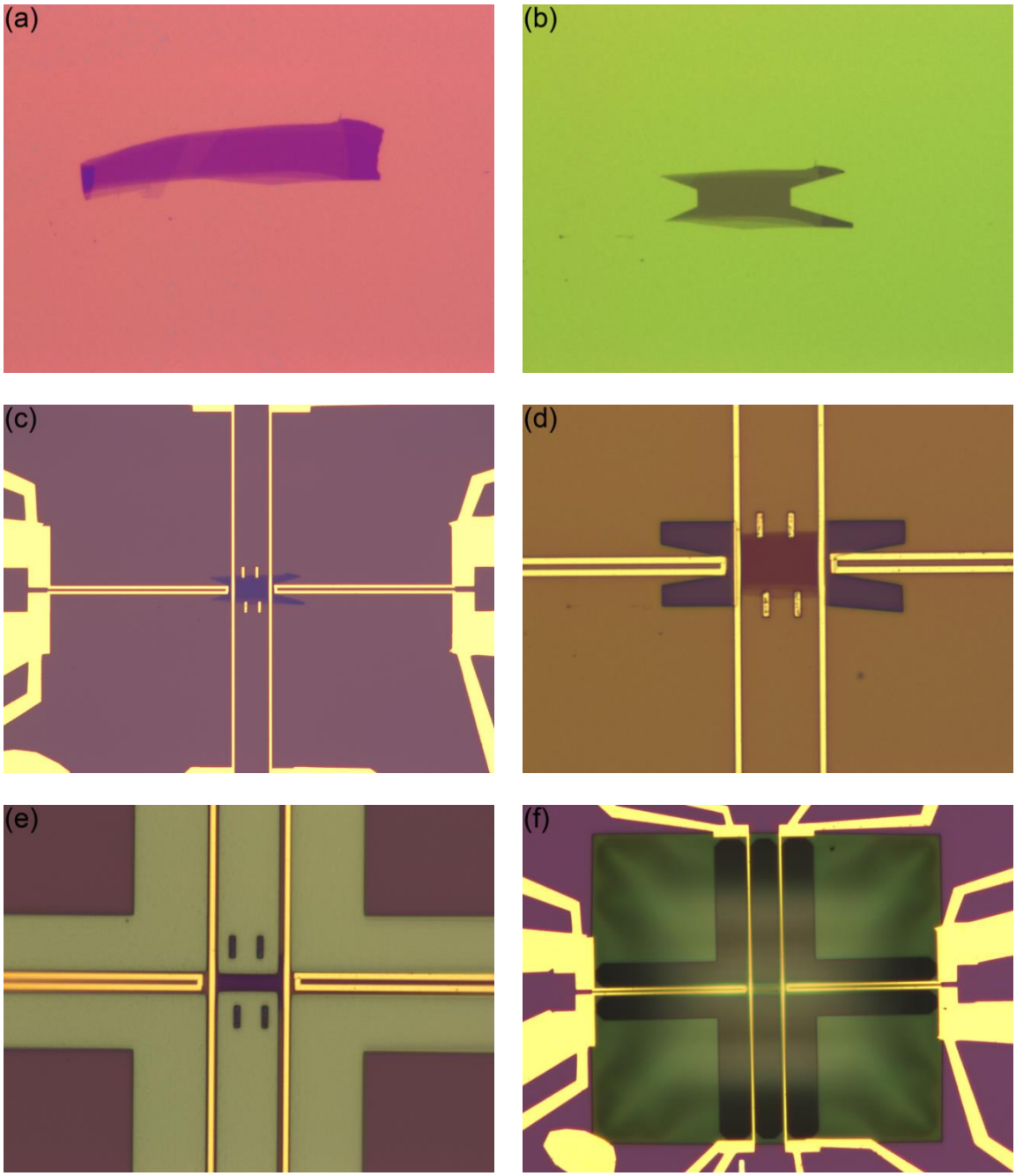

Figure 2.3

Figure 2.3: Fabrication of a symmetric suspended micro-thermometer device for an 8-layer graphene sample (G8). (a) Optical micrograph of the graphene flake exfoliated on Si substrate with 300 nm thermally-grown SiO_2 is shown. Also shown are optical micrographs of the device after cleaning the substrate and trimming graphene using oxygen plasma (b), after deposition of the metal resistance-thermometers (c), after the second step of trimming graphene (d), after etching windows in the SiO_2 layer to expose the Si underneath (e), and after etching the Si to suspend the device (f).

undercut during the last fabrication step by an anisotropic Si etchant, which is 4% tetramethylammonium hydroxide (TMAH) in water at a temperature of about 85 ^{o}C. The TMAH solution also cleans the e-beam resist from the top MLG surface, which is subsequently cleaned thoroughly in deionized water, methanol, and acetone. It is worth noting that some commercial resist removals contain TMAH. In addition, the TMAH solution does not etch graphene, as shown in a transmission electron microscopy (TEM) characterization of suspended single layer graphene (SLG),[52] as well as an earlier Raman spectroscopy, scanning electron microscopy (SEM), and mobility measurement results of supported SLG.[17]

2.2.5 Thermal Conductivity of Natural Graphite

A steady-state comparative method is established in this work to measure the thermal conductivity of the natural graphite (NG) source from which the graphene samples are exfoliated. The measurement setup is illustrated in Figure 2.4. The measurement setup consists of a graphite bar of 8 x 1.6 x 0.28 mm^3 dimension bonded to a reference copper bar of 9.3 x 1.8 x 0.6 mm^3 dimension using silver epoxy. A thin film

resistor attached to one end of the copper bar is used to generate temperature gradients in the copper bar and the graphite bar, which are measured using two constantan-copper differential thermocouples of 0.003 inch diameter. All thermocouples are thoroughly connected to make sure they are in thermal equilibrium with the bars at the contact points and located far from the contact ends to minimize measurement errors. The setup is placed inside a high vacuum cryostat surrounded by a radiation shield. The thermal conductivity of the graphite bar is obtained from the ratio of the thermovoltage differences (ΔV), dimensions of the bars, and literature thermal conductivity of copper according to

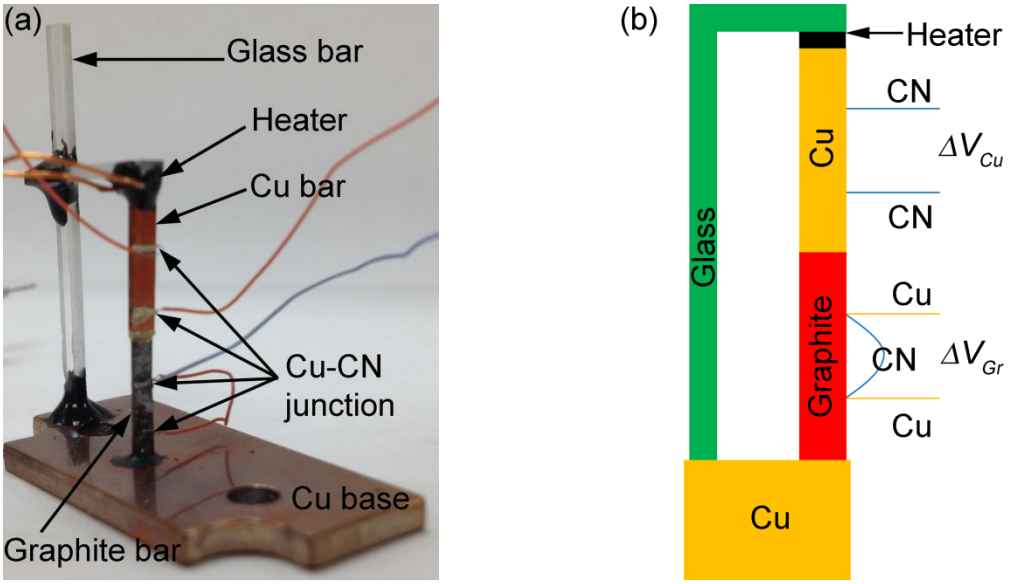

Figure 2.4: Measurement setup (a) and schematic of the measurement setup (b) for thermal conductivity measurement of graphite using comparative method with reference of copper and constantan-copper differential thermocouples.

$$\kappa_{Gr} = \kappa_{Cu} \frac{A_{Cu}}{A_{Gr}} \frac{L_{Gr}}{L_{Cu}} \frac{\Delta V_{Cu}}{\Delta V_{Gr}} \tag{2-15}$$

where κ, A, and L are the thermal conductivity, cross section area, and the length of the measurement sections, respectively. The uncertainty of this measurement by the heat losses via the thermal radiation and heat conduction through the thermocouple wires can be estimated by assuming the measurement bar as a one-dimensional fin with uniform cross section temperature. For a fin with thermal conductivity κ, uniform cross section area A and perimeter P, length L, and heat transfer coefficient h to ambient at temperature T_0, heat conduction rates through the hot end (Q_h) at temperature T_h and cold end (Q_c) at temperature T_c can be calculated according to[53]

$$Q_h = \frac{\sqrt{hP\kappa A}(T_h - T_0)}{\sinh mL}\left(\cosh mL - \frac{(T_c - T_0)}{(T_h - T_0)}\right) \tag{2-16}$$

$$Q_c = \frac{\sqrt{hP\kappa A}(T_h - T_0)}{\sinh mL}\left(1 - \frac{(T_c - T_0)}{(T_h - T_0)}\cosh mL\right) \tag{2-17}$$

where $m = \sqrt{hP/\kappa A}$. Each measurement bar is divided to 3 segments using the thermocouple contact points. Radiation heat loss is considered using the radiation heat transfer coefficient ($h = \varepsilon\sigma(T_s + T_0)(T_s^2 + T_0^2)$) based on the average temperature of each segment (T_s) where ε is the surface emissivity and $\sigma = 5.67 \times 10^{-8}\, Wm^{-2}K^{-4}$. A heat conduction rate comparable to that of the measurement is applied to the hot end of the copper bar. Using equations (2-16) and (2-17) and assuming a value for T_h, the temperature and the heat conduction rate at the cold side of the segment, which is the contact point of the copper bar with the constantan wire closer to the heater, are

calculated. This heat conduction rate subtracted by the calculated heat loss through the constantan wire gives the heat conduction rate applied to the hot side of the middle segment of the copper bar. This procedure is repeated for all 6 segments in the measurement bar. The temperature of the hot end of the copper bar is adjusted and the calculations are repeated until the temperature of the copper base next to the graphite bar converges to T_0. The obtained temperatures are used to calculate $\Delta V_{Cu}/\Delta V_{Gr}$ in equation (2-15). The results show that the measurement overestimates the thermal conductivity of the graphite bar at room temperature by less than 4% because of the heat losses via radiative heat transfer and heat conduction through the thermocouple wires. This overestimation becomes more negligible at lower temperatures.

2.3 Thermal Conductivity Measurements from 2D Graphene to 3D Graphite

Five MLG samples have been measured in this work, and are referred hereafter as G2, G6, G8, G27, and G34, where the number represents the layer thickness. Table 2.1 lists the dimensions of graphene samples measured in this work. These MLG samples are supported on 300 nm thick suspended SiO_2 bridges. Scanning electron micrographs (SEM) of G8 and G34 devices are shown in Figure 2.5. In addition, the basal-plane thermal conductivity of the NG source used to exfoliate the MLG samples has also been measured using a steady-state comparative method, as described in section 2.2.5.

Figure 2.6(a) shows the correlation between the temperature responses of the RT lines when RT_4 is the heater. The slope of a linear fit to the data is used to obtain α_1 according to equation (2-12). Figure 2.6(b) shows the temperature response of the RT

lines as a function of the heating rate Q_1 in RT_1. The slope of a linear fit to the data is used to obtain R_{b1} according to equation (2-5). The other thermal resistances can be obtained similarly. These measurements verify that for a device with symmetric design, the earlier measurement method reported in ref. 17 is sufficient without the need of switching the heater line in the measurement.

Sample	Layers	Width (μm)	Length (μm)
G2	2	3.0	9.8
G6	6	3.0	12.0
G8	8	2.9	12.4
G27	27	2.8	40.2
G34	34	5.3	35.8

Table 2.1: Dimensions of the measured MLG samples

In addition to the thermal conductance of the central MLG/SiO_2 beam, the thermal conductance of the center SiO_2 beam is measured after the graphene samples for several devices are etched away by oxygen plasma. The obtained SiO_2 thermal conductivity agrees well with the literature value in the temperature range of this measurement. In addition, the thermal conductance of the SiO_2 beam is about an order of magnitude smaller than the measurement value of G34. The thermal conductance (G) of the MLG alone can be obtained after the thermal conductance of the center SiO_2 beam is subtracted from the measured thermal conductance of the MLG/SiO_2. The thermal

conductivity of the supported MLG is obtained as $\kappa = GL/Wt$, where L, W, and t are the length between the two straight RT_2 and RT_3, width, and thickness of the MLG sample.

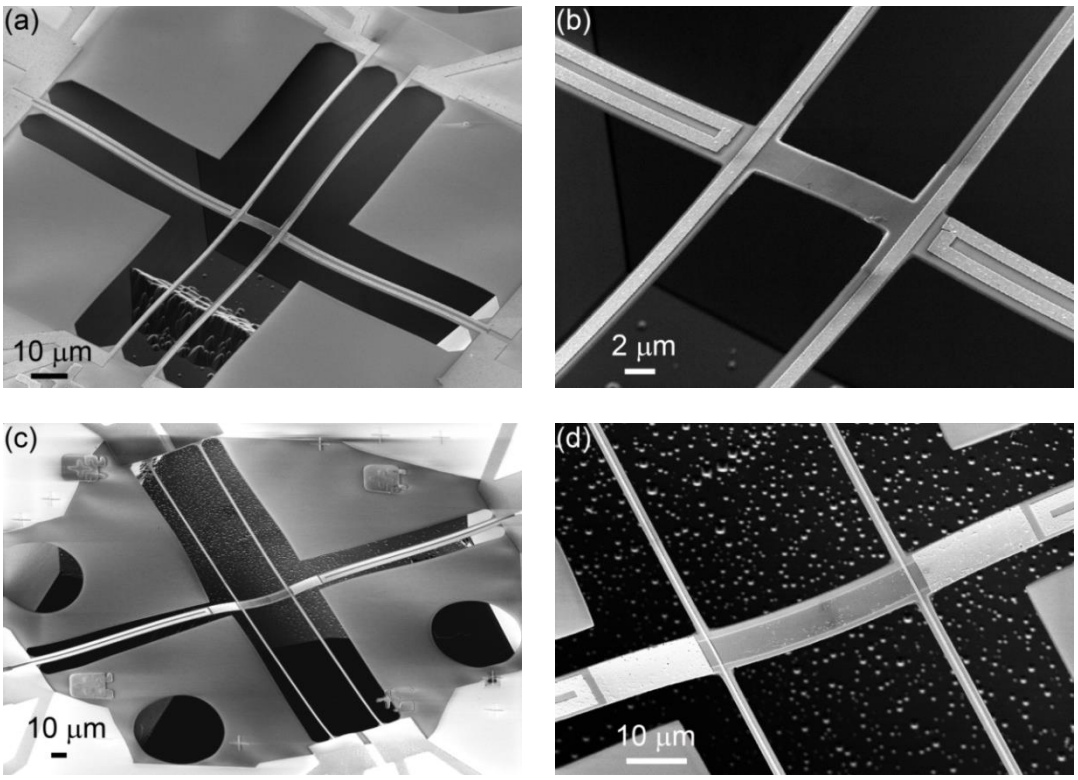

Figure 2.5: Scanning electron micrographs (SEM) of the micro-thermometer devices. Full view of the G8 device (a) and its central graphene region (b) at 45º view angle are shown. Also shown are the full view of the G34 device at 45º view angle (c) and its central graphene region at 30º view angle (d). The graphene can be seen on the central bridge between the straight metal lines.

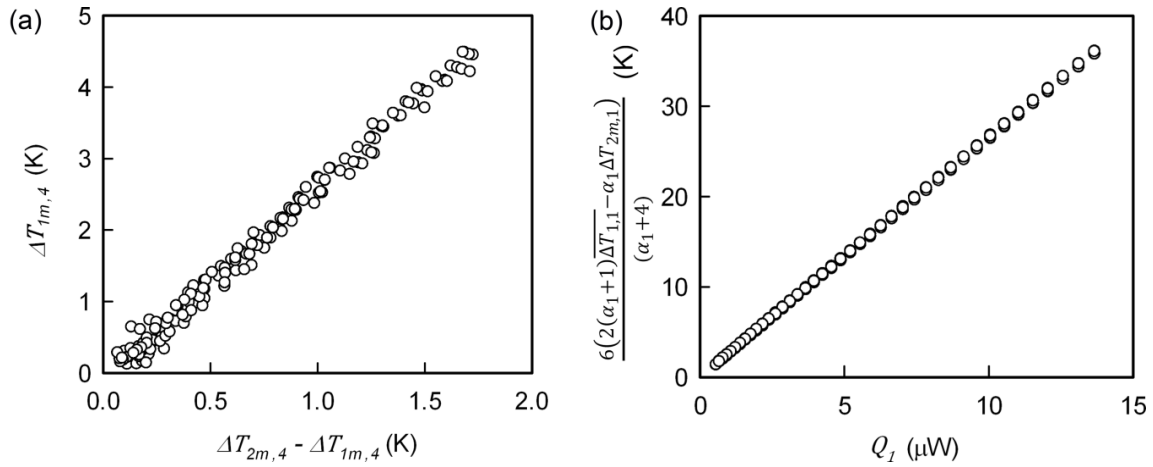

Figure 2.6: Analysis of the measurement results of G34 at 300 K to calculate R_{b1} based on equation (2-5). (a) The correlation between the measured temperature responses in RT_1, RT_2, and RT_4 when RT_4 is the heater. (b) The correlation between a combination of the measured temperature responses according to equation (2-5) and the electrical heating rate Q_1 in RT_1.

Three-dimensional finite element models of the measurement devices are used here to investigate the accuracy of the measurement method by systematic errors caused by neglecting thermal contact resistances and thermal resistance of the substrate, and the assumption of uniform temperature across the thickness of the supporting SiO_2 beam. With the use of the largest thermal interface resistance value reported for different MLG and SLG samples[44] as well as the lowest reported cross-plane thermal conductivity and the highest reported in-plane thermal conductivity of graphite at different temperatures,[32] the largest relative uncertainty is found in sample G27 at 100 K, where the basal-plane thermal conductivity is underestimated by no more than 9%. The details of the

simulations are discussed in Appendix A. Moreover, the symmetry of the fabricated device is verified by two measurements each with a different U-shape RT line as the heater line.

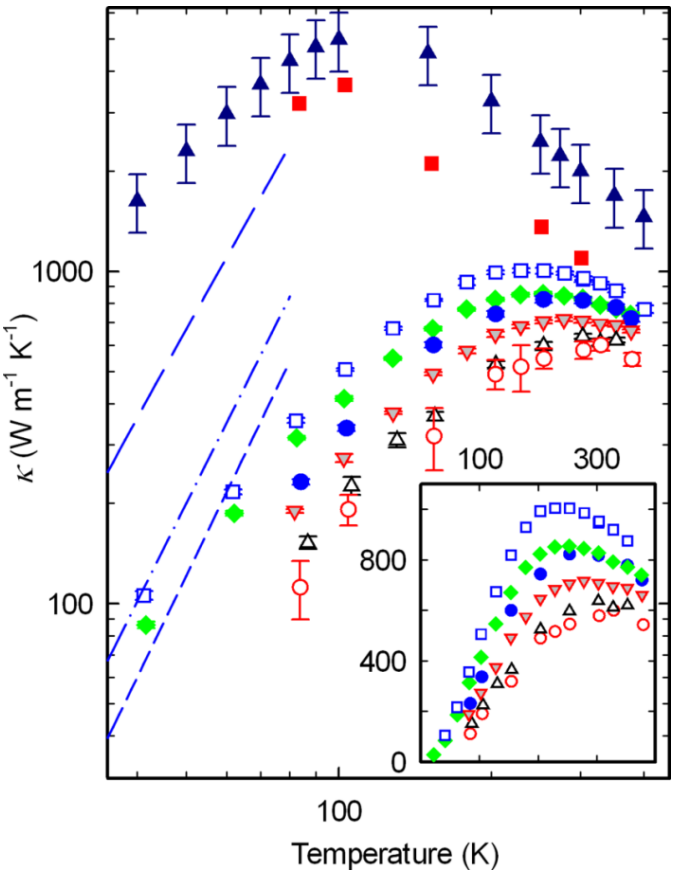

Figure 2.7

Figure 2.7: Measured thermal conductivity as a function of temperature for single-layer[17] (red unfilled circles), bilayer (black unfilled triangles), 6-layer (gray-filled inverted red triangles), 8-layer (blue filled circles), 27-layer (green filled diamonds), and 34-layer (blue unfilled squares) graphene supported on SiO_2. Also shown for comparison are the thermal conductivity of the NG source of the MLG samples (red filled squares) and the highest reported graphite thermal conductivity values included in Touloukian[32] (dark blue filled triangles). The lines are the calculated low-temperature thermal conductivity of a 34-layer MLG with dimensions similar to the 34-layer MLG sample with diffuse top and bottom surfaces (blue dashed line), specular top surface and diffuse bottom surface (blue dot-dashed line), and partially diffuse top and bottom surfaces with the same specularity parameter of 0.36 (blue dot-dashed line) or 0.9 (blue long dashed line). The two side edges are treated as diffuse and other scattering mechanisms are ignored in the calculation. The inset shows that the measured thermal conductivity of the supported MLG increases with increasing thickness, with the peak value shifted to a lower temperature for a thicker sample.

As shown in Figure 2.7 and Figure 2.8, the thermal conductivity of the FLG and MLG samples supported on SiO_2 increases with the layer thickness in the thickness range between 1 and 34 atomic layers, and has not yet reached the basal plane thermal conductivity of the NG source used to exfoliate the MLG samples. The convergence to the graphite value is considerably more gradual than the prediction of a recent MD simulation,[43] as shown in Figure 2.9. Figure 2.8 shows that the convergence rate becomes even more gradual at lower temperatures. The observed thickness dependence is opposite and qualitatively similar to the reported behaviors of suspended FLG[15,37] and FLG

encased in SiO_2,[19] respectively (see Figure 2.8). For suspended FLG, results from a micro-Raman measurement[37] and a theoretical calculation[15] both suggest that inter-layer phonon scattering decreases the thermal conductivity to approach the basal plane value of graphite when the suspended FLG layer thickness is increased to only about 4 layers.

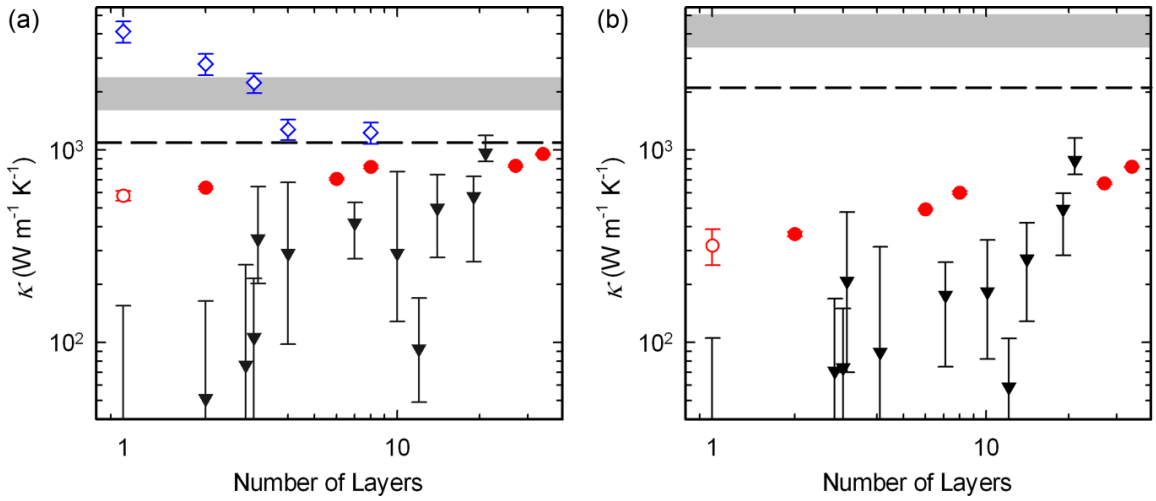

Figure 2.8: Basal-plane thermal conductivity of single-layer (red unfilled circle)[17] and multi-layer graphene supported on SiO_2 (red filled circles) as a function of layer thickness at 300 K (a) and 160 K (b). Also shown for comparison are the thermal conductivities of suspended single-layer and few-layer graphene samples (blue unfilled diamonds) reported by Ghosh et al.,[37] FLG samples encased in SiO_2 (black filled inverted triangles) reported by Jang et al.,[19] the NG source of the MLG samples (dashed line), and the highest reported graphite thermal conductivity values (grey shaded area) included in Touloukian et al.[32]

Moreover, the thermal conductivity peak is shifted to a lower temperature for a thicker supported FLG sample. Such peak shifts have not been resolved in the earlier studies of suspended FLG[37] and encased FLG.[19] In comparison, the peak thermal conductivity occurs at an even lower temperature of ~100 K for high quality pyrolytic graphite (PG)[32] and the NG source used to exfoliate the graphene samples. As the temperature increases to above room temperature, the thermal conductivity of G34 becomes comparable to that of the NG source (see Figure 2.7).

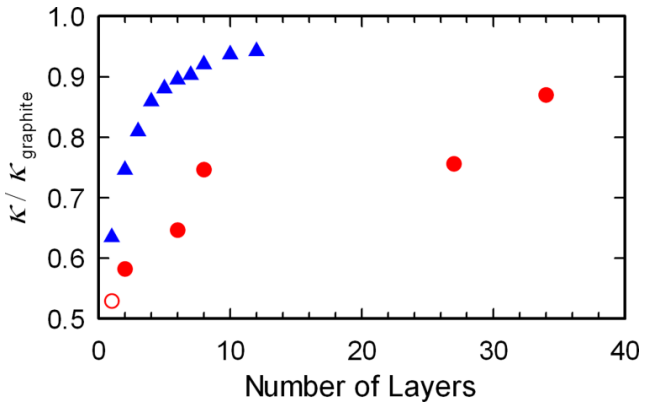

Figure 2.9: Measured room-temperature thermal conductivity of SLG (red unfilled circle)[17] and MLG samples supported on SiO_2 (red filled circles) normalized by their corresponding basal-plane thermal conductivity of the graphite source as a function of thickness. Shown for comparison is the MD simulation result (blue filled triangles) from ref. 43.

2.4 Mechanisms of Thermal Conductivity Suppression in Supported Multi-layer Graphene

To identify the causes of the observed thickness and temperature dependences in the thermal conductivity of supported MLG, we have examined a number of possible mechanisms. We first rule out phonon scattering by the lateral edges of the MLG flakes as the main cause for the suppressed thermal conductivity. The smallest lateral dimension of the MLG flakes is as large as 3 μm, which would have yielded much higher thermal conductivity than the measurement results if diffuse edge scattering was the dominant mechanism, as shown in ref. 18 and the calculation discussed below. Similarly, scattering by point defects inside the graphene lattice cannot explain the thickness dependence, because the D band associated with point defects[54] cannot be observed in the Raman spectra of all the MLG samples, which were exfoliated from the same graphite source and underwent the same sample preparation steps. Hence, the experimental result needs to be attributed to the interaction between the MLG and the underlying SiO_2 support, and also possibly polymer residue left on the top surface from the device fabrication process.[18,55] The van der Waals (vdW) interaction between graphene and an amorphous layer can result in perturbation of the atomic bonding in the graphene layers near the interface. Such vdW interaction is known to be short-range. For example, the interface adhesion energy between FLG and SiO_2 was found to saturate for FLG samples thicker than two layers,[56] suggesting that the static force interaction at the interface only affects the layer adjacent to the substrate. The short-range perturbation can modify the group velocities of phonons in the graphene layer next to the interface. For strong interfacial bonding between SLG and Ni(111)[57,58] or Ru,[59] softening of the optical branches and

modification of the flexural phonon (ZA) branch have been observed. However, as the interface bonding was weakened by intercalation of another layer of Cu or Ag at the interface[58,60] or for the case of SLG physisorbed on a Pt substrate,[61] the phonon dispersion of supported SLG becomes similar to that of pristine graphite. The adhesion energies for SLG–SiO_2 and FLG–SiO_2 interfaces were determined to be 0.45 J m^{-2} and 0.31 J m^{-2}, respectively,[56] smaller than the 0.72 J m^{-2} value reported for SLG–Cu interface.[62] Hence, we expect that the weak and short-range vdW interaction is insufficient to cause appreciable reduction of the group velocities of those phonon modes that dominate the thermal conductivity in suspended MLG. Therefore, static perturbation of the atomic bonding and modification of the phonon dispersion in the few graphene layers near the interface alone cannot explain the observed long range effect, namely the reduced thermal conductivity in the 34 layer MLG sample, especially the pronounced reduction at low temperatures.

Nevertheless, the short-range vdW interaction at the interface can still result in ripples throughout the supported MLG. Single-layer graphene was found to be rather conformal to the surface roughness of a SiO_2 support.[63,64] The roughness of graphene supported on SiO_2 was found to decrease from 185 pm to 125 pm when the thickness increases from single-layer to 15 layers.[56] Fitting of the thickness-dependent surface roughness data yields a surface roughness of 123 pm for graphite of an infinite number of graphene layers. In addition, with increasing thickness from SLG to BLG and three-layer graphene, the substrate induced surface roughness decreases by 50% and 70%, respectively. Such substrate-induced surface roughness for the supported FLG is comparable in amplitude and wavelength to the intrinsic ripples[52] in suspended SLG and

FLG, where both the ripple amplitude[65] and thermal conductivity[37] decrease with increasing layer thickness. Hence, substrate-induced ripples cannot explain the greatly suppressed magnitude and opposite thickness dependence in the measured thermal conductivity of the supported MLG. Similarly, stress and adhesion energy variations in the MLG samples are not expected to play a major role, as discussed below.

In a previous work on supported SLG sample,[17] tilted SEM was used to characterize the bending of the suspended SiO_2 beam of similar measurement devices. The central SiO_2 beam was found to be rather flat for two of the three samples, whereas some bending observed for the other sample may cause a tensile strain of less than 0.8% in the supported SLG. A linear perturbation analysis was used to examine the effect of the tensile strain on morphology of the supported SLG. Although the tensile strain can make the supported graphene less conformal to the substrate roughness, the effect is small for 1% tensile strain and the ~30 nm correlation length and ~0.3 nm amplitude of the SiO_2 surface roughness. Consequently, very similar thermal conductivity values were measured on the three supported SLG samples. Based on this finding, it is expected that stress in the MLG samples is not an important factor in the observed thermal conductivity.

It has been reported in ref. 56 that the measured work of adhesion is about 0.45 J m^{-2} between SLG and SiO_2 and saturates to 0.3 J m^{-2} when the layer thickness of FLG on SiO_2 increases to be two or more. Because the work of adhesion shows more significant and abrupt layer thickness dependence than the observed gradual change in the thermal conductivity of the supported MLG samples, it does not explain the thermal conductivity dependence on the layer thickness. The interface phonon transmission coefficient

depends on the adhesion energy. For 0.3 J m $^{-2}$ adhesion energy, Prasher has calculated that the transmission coefficient is about 0.7 for Si/Si and Si/Pt interfaces.[66] The value is on the same order of magnitude as the average interface transmission coefficient calculated in this work based on the measured interface thermal conductance between MLG and SiO_2.

The dynamic nature of the interface interaction is considered next. The average mean free path of phonons in graphite along a direction α can be calculated from

$$\langle \Lambda_\alpha \rangle^{-1} = \frac{1}{\kappa_\alpha} \sum_p \sum_{\vec{k}} |v_\alpha| \, k_B \, x^2 \frac{e^x}{(e^x - 1)^2} \frac{\Delta k^3}{8\pi^3} \quad , \qquad x \equiv \hbar\omega / k_B T \tag{2-18}$$

where the summations are over all phonon polarizations (p) and wave vector ($\vec{k}$) states in a discretized Brillouin zone, Δk^3 is the volume of each grid within the discretized Brillouin zone, $\hbar$ is the reduced Planck constant, ω is the angular frequency, k_B is the Boltzmann constant, T is the temperature, and κ_α and v_α are the thermal conductivity and phonon group velocity component along direction α, respectively. We have calculated the full phonon dispersion of graphite based on the density functional perturbation theory with the use of *ab initio* calculation package QUANTUM ESPRESSO[67] and employed a numerical approach to carry out the summation of equation (2-18) in the discretized Brillouin zone of graphite (see Appendix B). Based on the reported cross-plane thermal conductivity of graphite,[32] $\langle \Lambda_z \rangle$ was found to increase with decreasing temperature, from more than 60 atomic layers at 300 K to over 1000 atomic layers at temperatures lower than 70 K, as shown in Figure 2.10. The as-calculated $\langle \Lambda_z \rangle$ value at temperature 300 K, about 20 nm, is comparable to the 10 nm value estimated from the simplified kinetic

theory in a recent work.[68] In addition, the average basal plane mean free path calculated with this approach is even much longer than the cross-plane values and approaches about 240 nm at room temperature, which is about one third of the 775 nm value suggested for suspended graphene[14] based on the simplified kinetic theory and a graphene thermal conductivity value up to a factor of 2.6 higher than the graphite basal plane value used here. This calculation, based on equation (2-18) does not account for the frequency dependence of the phonon mean free path. According to Klemens,[69] the phonon-phonon scattering mean free path in the basal plane of graphene and graphite depends on ω and T according to $\Lambda \propto T^{-1}\omega^{-2}$. Because low-frequency acoustic phonons possess longer mean free paths and make larger contributions to the thermal conductivity than optical phonons, the average phonon mean free path weighted by the thermal conductivity contribution is expected to be even larger than the values found from equation (2-18). The large $\langle \Lambda_z \rangle$ values suggest that phonons originating from graphene layers far away from the interface can be scattered by the interface before other intrinsic scattering events occur. Such scattering at the top and bottom interfaces result in a reduction of the basal plane phonon mean free path. If the top and bottom surfaces are diffuse, the basal plane phonon mean free path because of scattering at the two surfaces is proportional to the MLG layer thickness and the ratio between the ab-plane component (v_a) and c-axis component (v_z) of the phonon group velocity.[69]

Theoretical calculation was conducted to investigate whether the measurement results could be attributed to partially diffuse phonon scattering at the top and bottom surfaces. Phonon scattering at the MLG–SiO_2 interface is complicated by the highly anisotropic phonon dispersion in MLG and phonon transmission across the interface.

Because of the anisotropic structure, the phonon group velocity is not collinear with the phase velocity, and it has a much larger v_a component than the v_z component for most of the phonon modes. For thick MLG, the average phonon transmission coefficient from MLG to SiO_2 can be evaluated from the thermal interface conductance (G_c) according to[70,71]

$$\langle \tau_{MLG \to SiO_2} \rangle = G_c \left(\sum_p \sum_{\vec{k}, k_z<0} |v_z| \, k_B \, x^2 \frac{e^x}{(e^x-1)^2} \frac{\Delta k^3}{8\pi^3} \right)^{-1} \qquad (2\text{-}19)$$

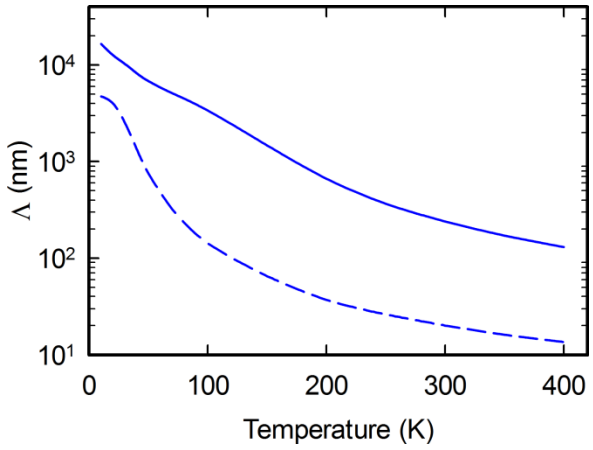

Figure 2.10: Calculated average phonon mean free path ($\langle \Lambda_z \rangle$) in graphite along the basal plane (solid line) and cross-plane (dashed line) directions. The mean free path of phonons that dominates the thermal conductivity is expected to be longer than the shown average mean free path.

Based on the reported G_c value measured for FLG supported on SiO_2,[72] this calculation yields a $\langle \tau_{MLG \to SiO_2} \rangle$ value of about 0.2 near room temperature. The use of the measured G_c value reported by Chen et al.[73] for encased FLG yields even higher $\langle \tau_{MLG \to SiO_2} \rangle$ values, which increase with decreasing temperature, as shown in Figure 2.11. This calculation is not applicable for SLG and thin FLG supported on SiO_2, where v_z vanishes because of the absence of cross-plane modes. However, the measured G_c value for SLG–SiO_2 interface is comparable to that for MLG–SiO_2,[72] suggesting coupling between some in-plane modes in SLG and surface and bulk modes in SiO_2.

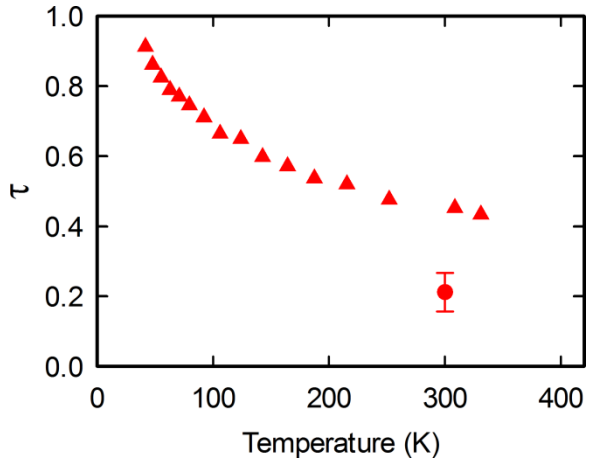

Figure 2.11: Calculated average interface phonon transmission coefficient from FLG to SiO_2 ($\langle \tau_{MLG \to SiO_2} \rangle$) based on the measured FLG–SiO_2 thermal interface conductance values reported by Chen et al.[73] for a 3 nm thick FLG (filled triangles) and Mak et al.[72] (filled circle).

Because of phonon scattering across the interface, MLG phonons emerging from the interface consist of a reflection component and a transmitted component from the adjacent amorphous layer. Because the temperature gradient is parallel to the interface, the transmitted component from the amorphous layer into the MLG is balanced by phonons scattered from MLG into the amorphous layer, so that the net interface heat flux is zero. In addition, phonons transmitted from or into the amorphous layer are expected to be highly diffuse because of atomic scale mean free path in the amorphous layer.

2.5 Thermal Conductivity of Multi-layer Graphene in the boundary scattering regime

We have derived an analytical model for thermal conductivity of supported MLG in the boundary scattering regime, which cannot be treated by existing models established for an isotropic thin film.[74] In the following, the temperature gradient is along the x-axis that is parallel to the basal plane, and the z-axis is along the c-axis of graphite. In this coordinate, θ and φ are the polar angle with x-axis and its corresponding azimuthal angle in the yz-plane, respectively (see Figure 2.12).

When only phonon-boundary scattering is considered, the Boltzmann transport equation (BTE) for the phonon distribution function f yields

$$\overrightarrow{v_g}.\nabla f = v\cos\theta_g \frac{\partial f}{\partial x} + v\sin\theta_g \frac{\partial f}{\partial s} = -\frac{f - f_0}{\tau} = 0 \qquad (2\text{-}20)$$

where $\overrightarrow{v_g}$ is the group velocity, s represents the spatial coordinate in the yz-plane along the projection of the phonon path into the plane, τ is the relaxation time, and f_0 is the

local equilibrium distribution. Based on the assumption that $\frac{\partial f}{\partial x} = \frac{\partial f_0}{\partial x}$, equation (2-20) is simplified to

$$\frac{\partial f}{\partial s} = -\frac{\cos\theta_g}{\sin\theta_g}\frac{\partial f_0}{\partial x} \tag{2-21}$$

In addition, for point B on the boundary with distance Δx from the cross section containing point A, the local equilibrium distribution can be found as

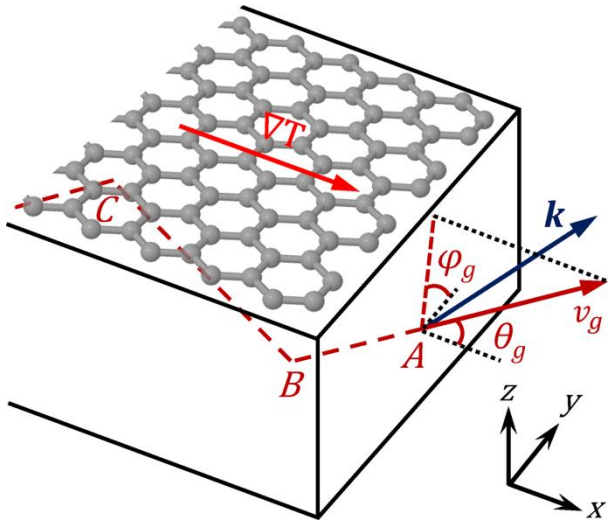

Figure 2.12: Schematic used to derive the phonon-boundary scattering model in a MLG ribbon where the group velocity and wave vector are not collinear because of the highly anisotropic structure. In this schematic, θ and φ are the polar angle with x-axis and the corresponding azimuthal angle in the yz-plane, respectively. The subscript g is used to denote the group velocity.

$$f_{B0} = f_{A0} - \Delta x \frac{\partial f_0}{\partial x} = f_{A0} - t_{BA} \cos\theta_g \frac{\partial f_0}{\partial T} \frac{dT}{dx} \tag{2-22}$$

where $f_{\Psi 0}$ is the local equilibrium distribution at point Ψ and $t_{\Psi\Omega}$ is the path length between any two points Ψ and Ω, which can be point B and A in equation (2-22). It is straightforward to use equation (2-21) and equation (2-22) to show that $f_A(\vec{k}) = f_B(\vec{k})$, where $\vec{k}$ is the wave vector that yields a group velocity vector parallel to the BA direction. This result is consistent with the intuition that phonon distribution does not vary along the path before phonons encounter a boundary when other scattering mechanisms are absent.

Phonons leaving B into the MLG consist of a specularly reflected component and a diffusely scattered component. Because of the amorphous structure of the SiO_2 support at the bottom interface and possibly polymer residue on the top surface, phonons scattered across the interface from the amorphous layer into the MLG are expected to contribute to the diffuse component and are balanced by phonons transmitted from MLG into the amorphous layer. In addition, because the temperature gradient is parallel to the interface, the net heat flux across the interface is zero. Hence, the interface condition can be described with an expression similar to that used in ref. 74 for an adiabatic solid-vacuum boundary

$$f_A = f_{A0} + g_A = (1 - P_B) f_{B0} + P_B f_C \tag{2-23}$$

where g_A is the deviation of f_A from the local equilibrium distribution f_{A0}, and the specularity parameter P_Ψ represents the probability that MLG phonons incident on interface point Ψ undergo mirror reflection. For incident phonons from C, the fraction

$(1-P_B)f_C$ is either diffusely reflected back into the MLG or transmitted across the interface into the amorphous layer. The latter transmitted component from MLG into the amorphous layer is cancelled by phonons scattered from the amorphous layer into the MLG, so that there is no net loss of phonons across the interface. Because the local equilibrium distribution yields the same number of phonons as the incident phonons integrated over the incident angles in a hemisphere, equation (2-23) satisfies the adiabatic condition that the number of MLG phonons incident on the interface is the same as the number of phonons leaving the interface into MLG.

Similar relations can be written for previous reflections such as $f_C = (1-P_C)f_{C0} + P_C f_D$, where the subscript D denotes the reflection point prior to C. To calculate f at an arbitrary point A, phonons are traced back along their group velocity direction to find previous reflection points. These equations are combined to find

$$g_A = f_{A0}\big((1-P_B) + P_B(1-P_C) + P_B P_C(1-P_D) + \cdots - 1\big) - \cos\theta_g \frac{\partial f_0}{\partial T}\frac{dT}{dx} M_A \tag{2-24}$$

where

$$M_A = (1-P_B)t_{BA} + P_B(1-P_C)(t_{BA}+t_{CB}) + P_B P_C(1-P_D)(t_{BA}+t_{CB}+t_{DC}) + \cdots \tag{2-25}$$

In the right hand side of equation (2-24), the term that contains f_{A0} vanishes because g_A = 0 when $\frac{dT}{dx} = 0$. Hence,

$$g_A(\theta_g, \varphi_g) = -\cos\theta_g \frac{\partial f_0}{\partial T}\frac{dT}{dx} M_A \tag{2-26}$$

where M_A is a function of θ_g, φ_g, and the specularity parameter. Equation (2-26) can be used to determine g_A at every point on the cross section. In the calculation of M_A, the reflection points are determined numerically to continue the series until the path reaches a fully diffuse surface or the two end surfaces perpendicular to the x-axis. Based on equation (2-26), the basal-plane thermal conductivity of supported MLG in the boundary scattering regime is calculated through

$$\kappa_{BS} = \frac{1}{A_c} \sum_{p} \sum_{\vec{k}} |v_g| \, k_B \, x^2 \frac{e^x}{(e^x - 1)^2} \frac{\Delta k^3}{8\pi^3} \left(\cos\theta_g\right)^2 \int_{A_c} M \, dA_c \qquad (2\text{-}27)$$

where v_g is the group velocity and A_c is the cross section of the MLG.

Based on a numerical summation over the discretized Brillouin zone, this calculation has been carried out for a 34-layer thick, 5.3 μm wide, and 35.8 μm long MLG sample with two diffuse side edges. In calculation of the MLG thermal conductivity, $\int_{A_c} M dA_c$ depends on θ_g and φ_g. By calculation of M_A for every point in the cross section of a MLG ribbon with the dimensions similar to those of G34, we calculate $\int_{A_c} M dA_c$ for every wave vector in the discretized Brillouin zone. For the calculations, the two side edges are assumed to be diffuse because they were formed using oxygen plasma etching that can result in rough edges. The specularity parameters for the top and bottom surfaces of the MLG ribbon are varied in the calculation. This numerical model reproduces the result of an analytical expression[75] for the case of diffuse scattering on all surfaces.

As shown in Figure 2.7, the calculation result can match the measurement result in the low temperature limit when the specularity is set to be either the same value of 0.36

for the top and bottom surfaces of the MLG, or 1 for a specular top surface and 0 for a diffuse bottom surface. The higher calculated values than the measurement results at higher temperatures can be attributed to the ignorance of other scattering mechanisms in the calculation. Because the supported MLG samples underwent thorough cleaning process compared to suspended graphene and h-BN samples reported in refs. 18 and 55 (see section 2.2.3), the top surface is expected to be relatively cleaner and characterized with a higher specularity parameter than the bottom MLG–SiO_2 interface. Hence, the two sets of parameters presented here give the two limiting cases. The specularity parameter in the range between 0 and 0.36 found for the MLG–SiO_2 interface is in agreement with the high transmission coefficient shown in Figure 2.11 at low temperatures.

Partially diffuse interface-phonon scattering can also explain the shift of the peak thermal conductivity to a lower temperature for a thicker MLG supported on SiO_2. The very high peak thermal conductivity value in graphite consists of a dominant contribution of low-frequency acoustic phonons,[33] which possess considerably longer Umklapp scattering mean free paths than intermediate and high-frequency phonons. Even in the frequency-independent boundary scattering treatment presented above, the low-frequency phonons with longer umklapp mean free paths are subjected to a larger relative reduction in their mean free paths than would occur for higher-frequency phonons. Moreover, it has been suggested that the interface phonon transmission coefficient and scattering rate increases with decreasing phonon frequency.[66] This frequency dependence is also revealed by the increased $\langle \tau_{MLG \rightarrow SiO_2} \rangle$ value with decreasing temperature that we have calculated based on the G_c values reported for encased FLG.[73] Hence, interface scattering considerably reduces the thermal conductivity contribution from low-frequency phonons

in supported MLG. Consequently, the relative contribution from intermediate and high-frequency phonons is higher in thinner supported MLG. Because of increased populations of intermediate and high-frequency phonons with increasing temperature, their thermal conductivity contribution in thin MLG increases with increasing temperature until the temperature where the Umklapp scattering becomes equally important as interface scattering for these phonons. Corresponding to the peak thermal conductivity, this temperature increases with decreasing MLG thickness because of decreased mean free path for phonon scattering at the top and bottom interfaces.

2.6 SUMMARY

The measurement and analysis show that partially diffuse interface scattering results in considerable suppression of the basal-plane thermal conductivity of MLG supported on amorphous oxide. Because of the long intrinsic mean free path of phonons, the suppression can be observed in supported MLG as thick as 34 atomic layers, and is more pronounced in thinner supported MLG. In comparison to MLG, a relatively short intrinsic phonon mean free path in hexagonal Boron nitride (h-BN) can also explain a recent measurement,[55] which shows that the room-temperature basal-plane thermal conductivity of few-layer h-BN coated with polymer residue approaches the corresponding bulk value when the layer thickness is increased to be just 11 layers. In addition, based on the observed shift of the peak thermal conductivity to a higher temperature in thinner supported MLG, the interface scattering results in a large reduction of the mean free path of low-frequency acoustic phonons in supported MLG. Such reduction cannot be simply attributed to interface roughness scattering, which is

known to be more effective in scattering higher-frequency, shorter wavelength phonons.[74] Instead, the reduction is largely influenced by interface phonon transmission, which is found to be non-negligible based on the measured thermal interface conductance values and is known to increase with decreasing phonon frequency.[66] Such interface scattering bears a resemblance to that revealed by past studies in phonon transport in thin film superlattices,[76] where the phonon distribution in one layer is influenced by that of the adjacent layer when the interface is partially diffuse. Compared to thin film superlattices, the distinction lies in the highly anisotropic phonon structure in MLG, which gives rise to currently unknown mode coupling mechanisms across the interface, which may be influenced by interface roughness. This knowledge gap calls for further studies of phonon transport at the interface of highly anisotropic materials, where an adaptation to Snell's law awaits to be discovered. Advances along this direction may allow for sensible selection of the support materials to increase the basal-plane thermal conductivity of supported graphene.

Chapter 3: Investigation of Electronic Thermal Transport in Supported Graphene with Magneto-Thermal Measurements

3.1 INTRODUCTION

The total thermal conductivity in a conductor consists of an electronic component (κ_e) and a lattice component (κ_l). Transport of electrons in metals has been described with success by the Sommerfeld theory in which the elementary excitations are quasi-particles that obey the Fermi-Dirac distribution.[77] A robust feature of the Sommerfeld theory is the Wiedemann-Franz Law (W-F law) that relates κ_e and electrical conductivity (σ) via the dimensionless Lorenz number (L)

$$L \equiv \frac{\kappa_e}{\sigma T}\left(\frac{e}{k_B}\right)^2 \tag{3-1}$$

where T is the absolute temperature, e is the elementary charge, and k_B is the Boltzmann constant. For non-interacting electrons with impurity scattering being the dominant mechanism, L is reduced to the Sommerfeld value $L_0 = \pi^2/3$.[78] The W-F law fails in presence of inelastic scattering processes since, during such processes, the energy flux carried by electrons is altered differently as compared to the charge flux,[77] making the mechanism of thermal current degradation significantly different than electric current degradation. The inelastic processes for electrons can be neglected at very low temperatures because of negligible population of phonons. At higher temperatures, L approaches $L_0(l_s/l_e)$ in a metal, where l_s and l_e are the electron mean free paths for entropy transport and charge transport, respectively. At temperatures higher than the

Debye temperature (Θ_D), where energy loss of electrons in collisions is small compared to $k_B T$, L approaches L_0 to a good approximation. Therefore, the W-F law failure occurs at intermediate temperatures where electronic energy loss during inelastic collisions in comparable to $k_B T$, and $l_s < l_e$. In intrinsic semiconductors, it can be shown that L for a single electronic band approaches $(r + 5/2)$, where r is a parameter describing the dependence of the electron scattering mean free time (τ) on the electron energy, i.e. $\tau = \tau_0 E^r$ with τ_0 being a constant. When τ is dominated by electron-phonon scattering in an intrinsic semiconductor, r takes a value of $-1/2$ so that L equals 2. In doped semiconductors with charge transport dominated by conduction in a single band, L depends on the carrier concentration and often falls between the metallic limit of $\pi^2/3$ and the intrinsic limit of 2. If two or more bands contribute to charge transport in a semiconductor, there is an additional bipolar contribution to the electronic thermal conductivity. In this case, the net charge current carried by each of the bands is nonzero under a temperature gradient, even when the net current vanishes in the semiconductor during the thermal conductivity measurement. The charge current of each band carries a Peltier heat with it, increasing the effective L considerably.[79-81]

Violation of the W-F law for nanoscale conductors has been discussed by a number of theoretical studies[82-85] and also suggested based on several measurements of carbon nanotubes[86-89] and nanowires.[90] The violation is mainly attributed to the increased electron-electron interaction in low-dimensional conductors. Also, fluctuations in conductance of mesoscopic conductors may lead to deviations from the W-F law even in the absence of inelastic scattering.[91] In graphene, electrons are described as relativistic Dirac Fermions with a linear dispersion and vanishing mass near the charge-neutral Dirac

point. There is an intriguing question regarding the contribution of the Dirac Fermions to thermal and thermoelectric transport.[92] Recently, a theoretical work has suggested that the W-F law can be violated in graphene at finite magnetic field and chemical potential.[93] Currently, there exists a significant gap between theoretical and experimental studies of the validity of the W-F law in low dimensions, especially in graphene. On one hand, a number of theories have suggested the breakdown of the W-F law in nanoscale conductors because of increased electron-electron interaction and other intriguing phenomena. Theorists have called upon experimentalists to verify their findings.[92,94] On the other hand, there has been very limited experimental investigation of the W-F law in low-dimensional structures. Hence, it is scientifically important to conduct experimental investigations on electronic thermal transport in graphene to determine whether or not the W-F law is applicable. Furthermore, the high thermal conductivity of graphene can be useful for many envisioned applications for graphene, such as thermal interface materials and thermal management of nanoelectronics.[14,44,95] The electronic contribution to thermal transport can become an important component when the Fermi level is tuned away from the Dirac point.[96] In addition, the electronic thermal conductivity can play an important role in the performance of graphene electronic devices where the thermal energy can be transferred by the hot carriers that are not in thermal equilibrium with the lattice.[20,21]

3.1.1 Present Work

This chapter introduces an experimental method that can be employed to study electronic thermal transport in graphene and other layered materials under a temperature gradient in the presence of electric and magnetic fields. We designed and fabricated four-

probe suspended micro-heater thermometer devices with transverse resistance thermometers (RTs) that allow us to perform measurements on longitudinal and transverse thermal conductivity, longitudinal and transverse electrical conductivity, and thermogalvanomagnetic effects. Results from such a measurement can provide fundamental understanding on electronic thermal transport. Experimental study of all these properties in a single sample provides significant information for understanding electronic, thermoelectric, and magnetothermoelectric transport mechanisms by eliminating sample-to-sample and measurement-to-measurement variations.

3.2 Measurement of Electronic Thermal Conductivity in Graphene

3.2.1 Electric-Field Effect Measurement of Graphene Lorenz Number

Electric field effect measurements can be employed to separate the electronic thermal conductivity (κ_e) and lattice thermal conductivity (κ_l) and consequently determine the Lorenz number of graphene. The thermal conductivity of supported graphene can be measured as a function of the charge carrier concentration by introducing a back-gate to a suspended resistance thermometer device. Compared to micro-heater thermometer devices described in Chapter 2 that are used to measure thermal conductivity of supported graphene samples, a through hole should be etched in the silicon substrate so that a low thermal conductivity metal can be evaporated on the backside of the suspended beams and the silicon substrate. A polycrystalline Bi film ($\kappa < 3$ W m $^{-1}$ K $^{-1}$ [97,98]) can serve as a back-gate to tune the Fermi level and carrier concentration in the graphene sample. For a 300nm thick SiO_2 bridge covered with

single-layer graphene, the total thermal conductance of the bridge will increase by ~20 % with addition of 40 nm thick Bi film.

For a single layer of 3 μm x 3 μm graphene on a 300 nm SiO_2 film of a Si substrate that serves as the back-gate, Zhang et al. has shown that the electrical resistance (R) can be tuned from 4 kΩ to about 100 Ω when the Fermi energy (E_F) is moved from the charge-neutral Dirac point to either the conduction or valence band by applying a gate voltage on the order of ±40 volts.[99] The electronic thermal conductance can be calculated as $G_e = (k_B/e)^2 LT/R$. If $L = L_0$, G_e would increase from about 1.8 nW K^{-1} to 74 nW K^{-1} when R is reduced from 4 kΩ to 100 Ω and the equivalent $k_e = G_e l/wt$ would increase from 5.5 W m^{-1} K^{-1} to 220 W m^{-1} K^{-1}. For the ~10 μm long, 1.2 μm wide graphene ribbon reported by Seol et al.,[17] R was measured to be about 30 kΩ at zero gate voltage, yielding the 2D resistivity $\rho = Rw/l$ ~ 3.6 kΩ that is close to the value reported by Zhang et al. for the case that E_F is near the Dirac point.[99] When a ±40 volt gate voltage is applied to the Bi film on the back side of the SiO_2 beam, it can be expected that ρ and R of this sample would decrease to ~100 Ω and ~830 Ω, respectively. Correspondingly, G_e would increase from about 0.24 nW K^{-1} to 9 nW K^{-1}. This G_e increase (ΔG_e) is larger than the sensitivity of the measurement device. The Lorenz number can be obtained from the measured ΔG_e and measured change (Δg) in the electrical conductance ($g = 1/R$) upon the application of a gate voltage, i.e. $L = (e/k_B)^2 \Delta G_e/\Delta g T$.

3.2.2 Thermogalvanomagnetic Measurement of Graphene Hall Lorenz Number

Transverse thermogalvanomagnetic effects occur where motion of electrons is deflected by an external magnetic field perpendicular to the direction of current (heat) flow. Because of these effects, an electric field and a temperature gradient are induced in a direction perpendicular to the directions of the magnetic field and the current (heat) flow, and Hall coefficient (R_H), Nernst coefficient ($|N|$), Ettingshausen coefficient ($|P|$), Righi-Leduc coefficient ($|S|$) are defined as [81]

$$R_H \equiv \frac{E_y}{B_z\, j_x} \tag{3-2}$$

$$|N| \equiv \frac{E_y}{B_z\ dT/dx} \tag{3-3}$$

$$|P| \equiv \frac{dT/dy}{B_z\, j_x} \tag{3-4}$$

$$|S| \equiv \frac{dT/dy}{B_z\ dT/dx} \tag{3-5}$$

where B, j, and T represent magnetic field, current concentration, and temperature, respectively, and the subscripts denote components of a vector along coordinate axes according to Figure 3.1. Because of the applied magnetic field along the z-axis (B_z), an electric field along the y-axis (E_y) and a temperature gradient along the y-axis (dT/dy) are induced.

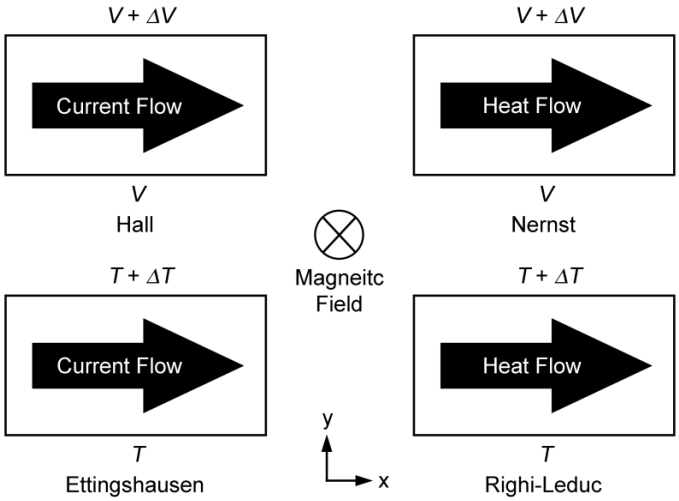

Figure 3.1: Transverse thermogalvanomagnetic effects. Presence of the magnetic field induces a temperature difference (ΔT) and a voltage difference (ΔV) in a direction perpendicular to the direction of magnetic field and direction of heat or current flow.[81]

In the absence of a magnetic field, the heat fluxes carried by electrons and phonons are parallel to the temperature gradient ∇T. With an external magnetic field, applied along the z-axis and perpendicular to the external temperature gradient $\nabla_x T$ applied along the x-axis, the Lorentz force acting on the electrons results in a transverse electronic heat flux $q_y = \kappa_{xy} \nabla_x T$ that is perpendicular to both B_z and $\nabla_x T$, where κ_{xy} is the transverse electronic thermal conductivity consisting of only the electronic contribution, because the phonon flux is unaffected by the external magnetic field. With adiabatic boundaries except at the two surfaces perpendicular to the x-axis, a transverse temperature gradient $\nabla_y T$ is established, resulting in a transverse heat flux of $-\kappa_{yy} \nabla_y T$ that cancels q_y, where κ_{yy} is the longitudinal thermal conductivity consisting of both electron and phonon contributions along the y direction. Hence, $\kappa_{xy} =$

$\kappa_{yy}\nabla_y T / \nabla_x T$. If the longitudinal thermal conductivity is isotropic in the xy plane as in the basal plane of graphene, $\kappa_{yy} = \kappa_{xx}$, κ_{xy} can be obtained by measuring κ_{xx}, $\nabla_y T$, and $\nabla_x T$. Similarly, for the Hall effect, the transverse electrical conductivity can be obtained as $\sigma_{xy} = \sigma_{yy} E_y / E_x$. If the longitudinal electrical conductivity is isotropic, i.e. $\sigma_{xx} = \sigma_{yy}$, $\sigma_{xy} = {\sigma_{xx}}^2 R_H B_z$ can be obtained by measuring σ_{xx} and R_H. The dimensionless Hall Lorenz number is defined as

$$L_{xy} \equiv \frac{\kappa_{xy}}{\sigma_{xy} T} \left(\frac{e}{k_B}\right)^2 \tag{3-6}$$

The Boltzmann Transport Equation can be used to show that $L_{xy} \approx L_0 (l_s / l_e)^2$ in a metal and approaches L_0 for $T > \Theta_D$ where $l_s = l_e$.[100] Experimentally, L_{xy} measured using the thermal Hall effect is close to L_0 in copper at room temperature, and falls faster than L with decreasing temperature since $L \approx L_0 (l_s / l_e)$.[100] Because κ_{xy} consists of only the electronic contribution, the thermal Hall measurement of L_{xy} provides an effective approach to investigate electronic thermal transport in some conductors where L is experimentally inaccessible because a large longitudinal κ_l prevents accurate measurement of a small longitudinal κ_e.

Measurements of thermogalvanomagnetic coefficients, κ, κ_{xy}, k_e, L, and L_{xy} can be conducted using back-gated suspended resistance thermometer devices (see Figure 3.2) that are designed to impose an electric field (temperature gradient) along a graphene sample and measure the transverse temperature difference and electric field induced by an external magnetic field perpendicular to the basal plane of graphene (B_z).

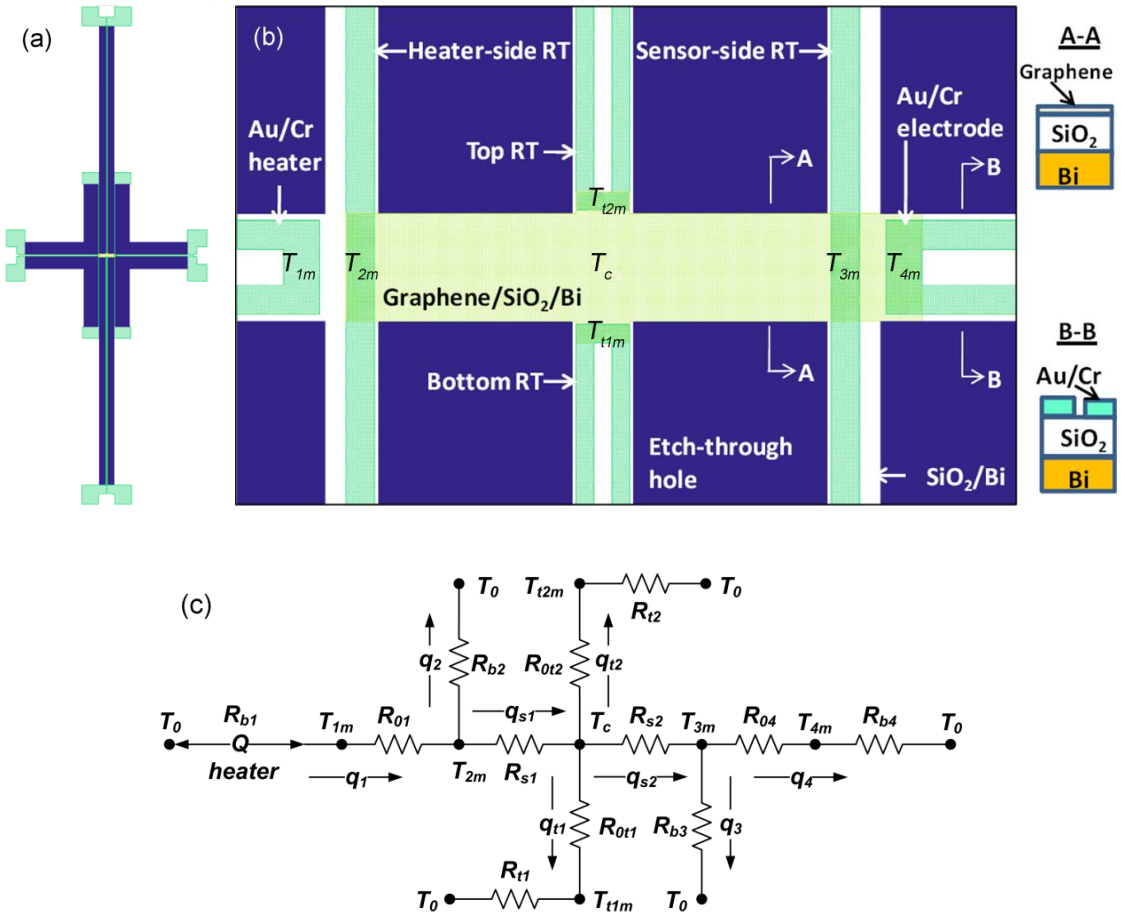

Figure 3.2: Schematic of a suspended device for thermal Hall measurement of a trimmed graphene flake (a) Full view. (b) Central graphene region. (c) The corresponding thermal resistance circuit. Thermal resistances, heat flows, and temperatures of the resistance thermometers (RTs) are represented by R, q, and T, respectively, according to (b). T_0 and Q are the ambient temperature and rate of heat generation in the heater (RT_1), respectively. Subscripts m and t denote midpoint of metal lines and transverse metal lines, respectively.

Compared to the resistance thermometer device shown in Figure 2.1 and Figure 2.2, a back-gate needs to be added. In addition, two additional resistance thermometers are added to measure the transverse temperature gradient $\nabla_y T$ developed upon the application of a longitudinal temperature gradient $\nabla_x T$ and a magnetic field B_z. Since transverse edges should be adiabatic for measurement of κ_{xy}, thermal conductance of these transverse resistance thermometers should be minimized. By increasing the length and decreasing the width of the transvers RTs, the thermal conductance can be reduced significantly compared to the longitudinal and transverse thermal conductance of the bridge, which includes graphene, 300 nm of SiO_2, and the back-gate metal. This approach ensures that there is negligible deviation from the adiabatic assumption.

With adiabatic boundaries at the transverse edges, the ratio of the transverse temperature gradient to the longitudinal temperature gradient can be obtained as

$$\frac{\nabla_y T}{\nabla_x T} = \frac{\kappa_{xy}\left(1 + \kappa_{xy,Bi} t_{Bi} / \left(\kappa_{xy} t\right)\right)}{\kappa_e\left(1 + \kappa_l/\kappa_e + \kappa_{SiO_2} t_{SiO_2}/(\kappa_e t) + \kappa_{Bi} t_{Bi}/(\kappa_e t)\right)} \tag{3-7}$$

where κ_{xy} is the transverse electronic thermal conductivity of graphene, κ_e and κ_l are the longitudinal electronic and lattice thermal conductivity of the graphene, respectively, $\kappa_{xy,Bi}$ is the transverse electronic thermal conductivity of the polycrystalline Bi film, κ_{Bi} (< 3 W m $^{-1}$ K $^{-1}$) and κ_{SiO_2} (~1 W m $^{-1}$ K $^{-1}$) are the longitudinal thermal conductivity of the Bi film and SiO_2 layer, respectively, and t = 0.334 nm, t_{SiO_2} = 300 nm, t_{Bi} = 40 nm are the thickness of the graphene, SiO_2, and Bi, respectively. In addition,

$$\frac{\kappa_{xy}}{\kappa_e} = \frac{L_{xy}}{L}\frac{\sigma_{xy}}{\sigma} = \frac{L_{xy}}{L}\sigma R_H B_z = \frac{L_{xy}}{L}\mu B_z \tag{3-8}$$

where $\sigma = \sigma_{xx} = \sigma_{yy} = ne\mu$ is the longitudinal electrical conductivity of graphene, $\sigma_{xy} = (\sigma_{xx})^2 R_H B_z$ is the transverse electronic thermal conductivity of graphene, μ is the carrier mobility, the Hall coefficient $R_H = 1/ne$, and n is the carrier concentration. Hence,

$$\frac{\nabla_y T}{\nabla_x T} = \frac{1 + \kappa_{xy,Bi} t_{Bi}/(\kappa_{xy} t)}{1 + \kappa_l/\kappa_e + \kappa_{SiO_2} t_{SiO_2}/(\kappa_e t) + \kappa_{Bi} t_{Bi}/(\kappa_e t)} \frac{L_{xy}}{L}\mu B_z \tag{3-9}$$

Assuming that κ_l of graphene is close to the in-plane thermal conductivity of supported graphene (~600 W m $^{-1}$ K $^{-1}$), κ_e is about 200 W m $^{-1}$ K $^{-1}$ based on the above estimation for the case that E_F is tuned away from the charge neutral Dirac point, L_{xy}/L is on the order of unity, B_z in the range of 1-9 Tesla (1 T = 1 V s m $^{-2}$), the large mobility of 20,000 (or 200,000) cm ^{2} V $^{-1}$ s $^{-1}$ found in supported (or clean suspended) graphene can result in a $\nabla_y T/\nabla_x T$ ratio larger than unity. For a longitudinal temperature difference in the range of 1 to 10 K along the graphene ribbon, the transverse temperature difference between the top and bottom edges of the graphene ribbon will be two orders of magnitude higher than the ~10 mK sensitivity of the two transverse RT lines.

According to equation (3-7), the transverse electronic thermal conductivity of the graphene can be obtained from the thermal Hall measurement as

$$\kappa_{xy} = \frac{l}{R_s t w}\frac{\nabla_y T}{\nabla_x T} - \kappa_{xy,Bi}\frac{t_{Bi}}{t} \tag{3-10}$$

where $2l$ and w are the length and width of the graphene sample, respectively, and the longitudinal thermal resistance $R_s \equiv l/(\kappa t + \kappa_{Bi} t_{Bi} + \kappa_{SiO_2} t_{SiO_2})w$ can be measured. After removing the graphene with a short oxygen plasma etch, the transverse electronic thermal conductivity of the Bi film can be obtained as $\kappa_{xy,Bi} = (l/R_{Bi+SiO_2} t_{Bi} w)\nabla_y T/\nabla_x T$, where $R_{Bi+SiO_2} \equiv l/(\kappa_{Bi} t_{Bi} + \kappa_{SiO_2} t_{SiO_2})w$ will be measured, and the $\nabla_y T/\nabla_x T$ ratio measured after etching the graphene becomes

$$\frac{\nabla_y T}{\nabla_x T} = \frac{1}{1 + \kappa_{l,Bi}/\kappa_{e,Bi} + \kappa_{SiO_2} t_{SiO_2}/(\kappa_{e,Bi} t_{Bi})} \frac{L_{xy,Bi}}{L_{Bi}} \mu_{Bi} B_z \qquad (3\text{-}11)$$

For Bi, the lattice thermal conductivity $\kappa_{l,Bi}$ is comparable to the electronic thermal conductivity $\kappa_{e,Bi}$,[101] the ratio between the Hall Lorenz number and Lorenz number $L_{xy,Bi}/L_{Bi}$ is assumed to be on the order of unity, and the mobility μ_{Bi} is reported to be ~200 cm ^{2} V $^{-1}$ s $^{-1}$ in ~40 nm thick thermally evaporated polycrystalline Bi films.[102] The low μ_{Bi} leads to a low $\nabla_y T/\nabla_x T$ ratio on the order of 0.1-0.01 after the graphene is etched away. Hence, the $\kappa_{xy,Bi} t_{Bi}/(\kappa_{xy} t)$ term in equation (3-10) is expected to be below 10% of κ_{xy} of the graphene. As discussed in section 3.2.5, the longitudinal thermal resistances R_s and R_{Bi+SiO_2} can be measured before and after etching the graphene based on heat conduction analysis using the thermal resistance circuit shown in Figure 3.2(c).

With the application of a gate voltage to the Bi film, the longitudinal four-probe electrical conductivity σ and electronic thermal conductivity κ_e of the graphene can be tuned and measured. The Hall coefficient R_H and the transverse electrical conductivity σ_{xy} can be obtained by using the two transverse RT lines as the probes of the transverse open-loop Hall voltage when a longitudinal current is passed through the graphene in the

presence of a magnetic field B_z. These measurements can allow for the determination of both L and L_{xy}. In addition, the thermogalvanomagnetic coefficients can be measured by measuring the temperature difference or voltage difference that develops in a direction perpendicular to the directions of current or heat flow because of an external magnetic field, as depicted in Figure 3.1.

3.2.3 Micro-Fabricated Heater-Thermometer Devices for Magneto-Thermal Measurements

In this work, measurements are conducted using suspended micro-heater thermometer devices, each of which consists of six metal resistance-thermometers (RTs) on suspended beams of SiO_2 with 300 nm thickness. The fabrication process for these devices is similar to that described in section 2.2.4. Two fine metal lines are added to measure the transverse temperature gradient and graphene sample is transferred atop the device as explained in section 3.2.4. Figure 3.3 shows a device that is used to conduct magneto-thermal measurements on a bilayer graphene sample.

Another fabrication process is developed in this work in order to deposit a metal layer on the backside of the suspended beams that can be used to tune the carrier concentration of graphene using the electric field effect. In brief, the fabrication process starts with a double-side polished Si wafer with low-stress SiN_x (SiO_2) on both sides. Alignment markers are fabricated using two aligned photolithography steps on the front side and backside of the wafer, followed by e-beam evaporation of Cr/Pt and a lift-off process in acetone. A window is opened in the backside SiN_x using electron beam

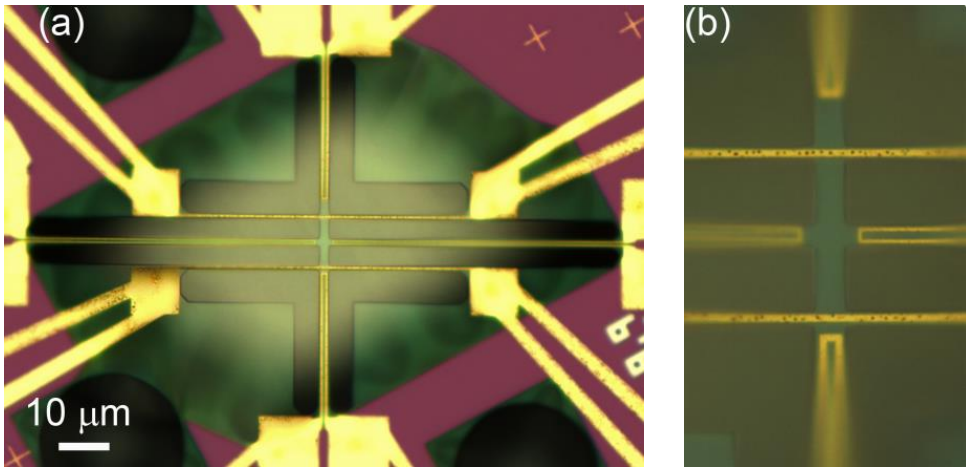

Figure 3.3: Optical micrograph of a micro-fabricated device with SiO_2 beams for magneto-thermal measurements. Full view (a) and the central region (b) of the device are shown.

lithography (EBL) followed by a reactive-ion etching (RIE) process with CF_4 gas. The sides of the window are adjusted along (111) planes in order to obtain smooth side walls after wet-etching of Si. A through-substrate hole is etched in Si using 4% (vol/vol) tetramethylammonium hydroxide (TMAH) in water at a temperature of about 85 °C, which produces a suspended membrane as shown in Figure 3.4(a). Metal lines and contact pads are fabricated using an EBL process followed by e-beam evaporation of Cr/Au and a lift-off process in acetone. The result is shown in Figure 3.4(b). The heater-thermometer metal lines are isolated from the membrane using another set of EBL and RIE processes. The gate metal is formed on the backside of the device by evaporating a metal on the backside of the suspended beams through the through-hole. With the smooth side walls of the through-hole, deposition of a thin layer of metal is sufficient to make an

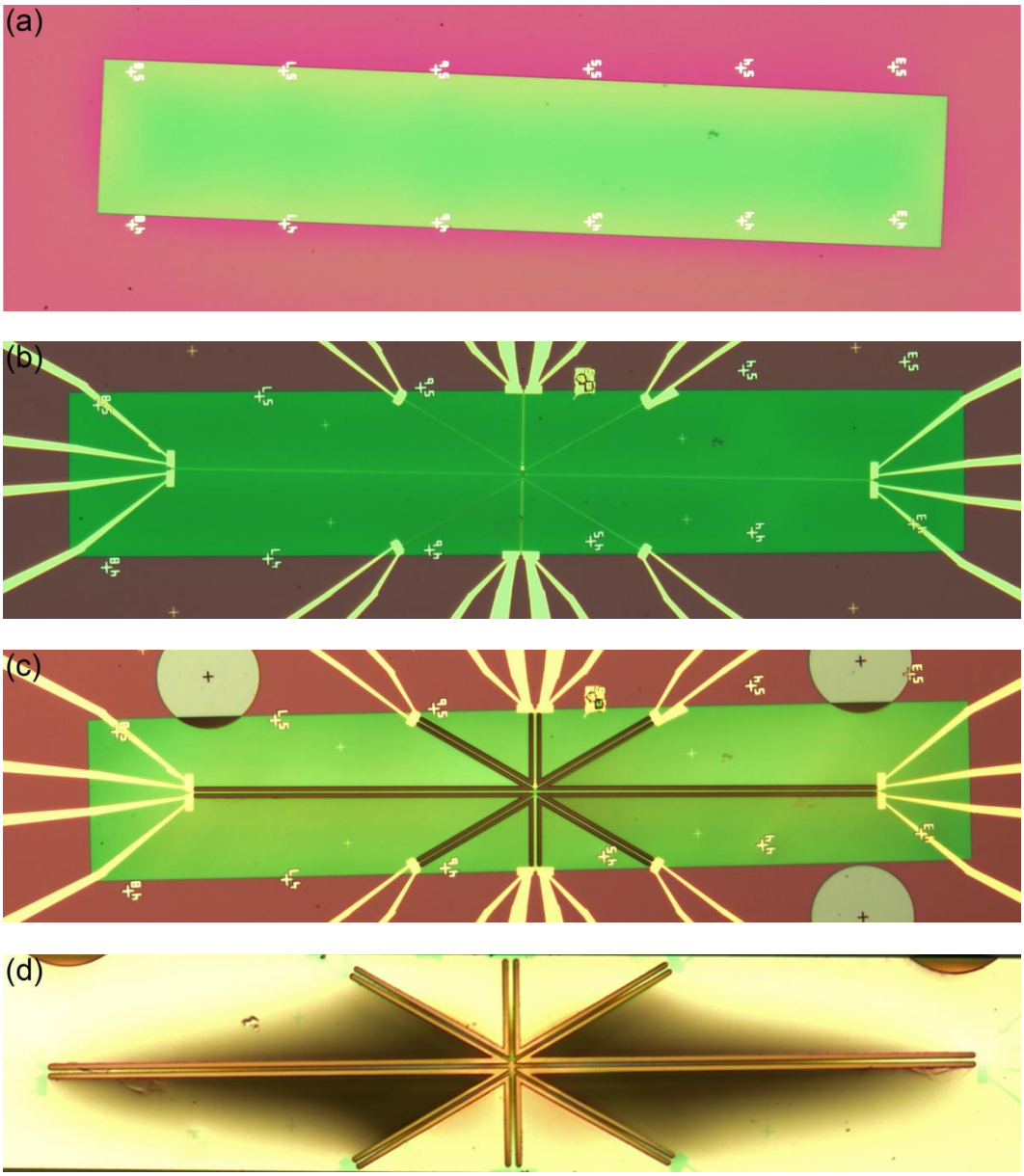

Figure 3.4

Figure 3.4: Fabrication steps for micro-heater thermometer devices with a back-gate. (a) and (b) show optical micrographs of a suspended SiN_x membrane over a substrate-through hole in the Si substrate and the patterned metal lines on the suspended membrane, respectively. (c) Etching windows around the metal lines makes suspended beams that are isolated from the membrane. (e) Optical micrograph of the backside of the measurement device showing the 30-40 nm Ti layer deposited at the backside of the suspended bridge to be used as a gate to tune the charge carrier concentration in graphene.

electrical connection to the metal deposited on the backside of the suspended beams. Figure 3.5 shows scanning electron micrographs (SEM) of two fabricated devices with back-gate. In the device shown in Figure 3.4(c) and Figure 3.5 (b), the bases of the heater-thermometer metal lines are designed to reach to the edges of the suspended membrane so that the base temperature can be assumed to be similar to that of the ambient, thus reducing systematic error in the measurement. Compared to the device shown in Figure 3.3, the relatively high mechanical strength of low-stress SiN_x enables the fabrication of much longer transverse resistance-thermometers to further minimize the heat conduction through them.

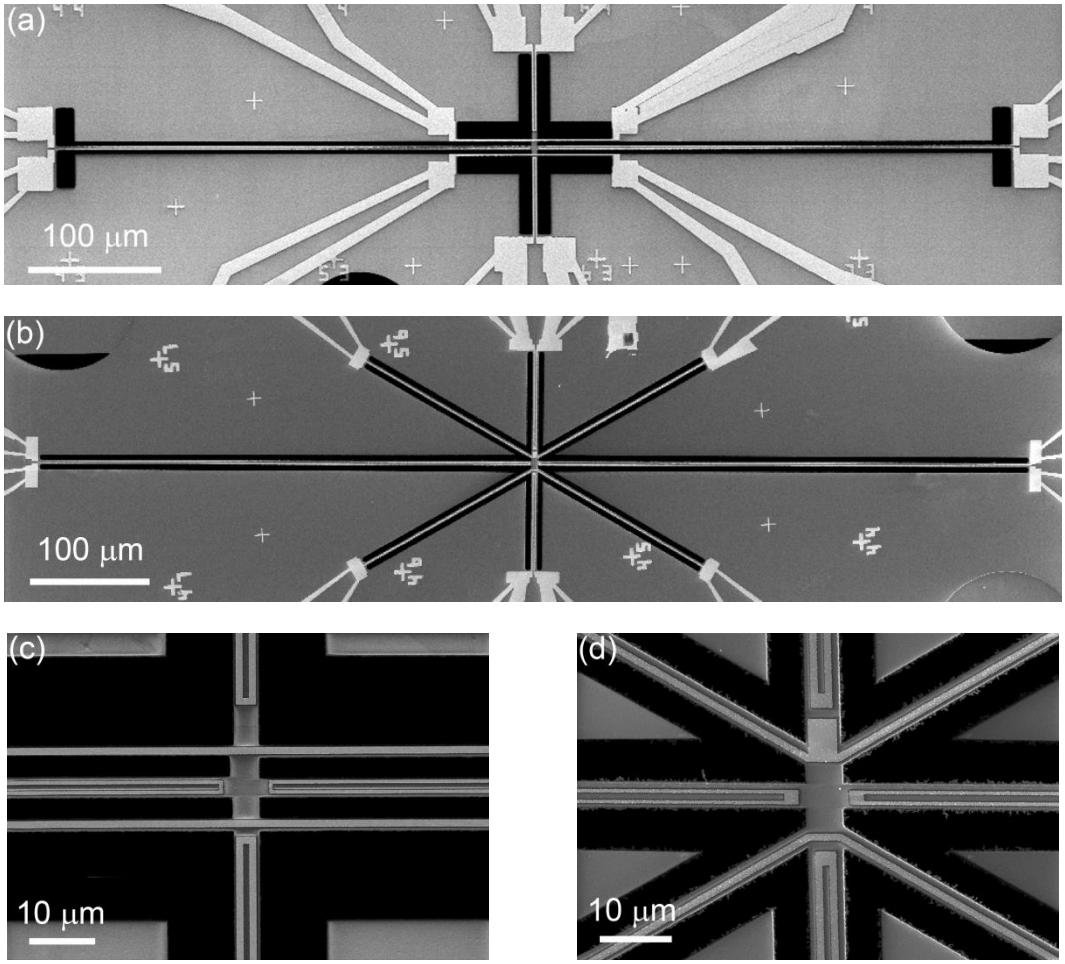

Figure 3.5: (a,b) SEM images of graphene magneto-thermal measurement devices on low-stress SiN_x membranes with a thin film Ti back-gate. In the device shown in panel (b), the base of all the resistance thermometers except for the transverse ones is located on SiN_x/Si. (c) and (d) show SEM images of the central bridge of (a) and (b), respectively.

3.2.4 Graphene Exfoliation and Assembly

Graphene samples are obtained by exfoliation[8] of natural graphite flakes (NGS Naturgraphit GmbH) onto a Si substrate covered by ~290 nm of thermally-grown SiO_2. Graphene samples are located using optical microscopy and their thickness is determined using the features of single-layer and bilayer graphene in their Raman spectra.[48] An EBL process followed by low-power oxygen plasma is used to pattern the graphene flakes to the desired shape. Graphene samples are transferred to micro-fabricated heater-thermometer devices using an aligned transfer technique.[55] Alignment marks are deposited using an EBL process, e-beam evaporation of Au, and a lift-off process in acetone. A thick layer of PMMA (~1.5 μm) is then spin-coated on the substrate. The substrate is placed in a 1% hydrofluoric acid solution, which etches the SiO_2 at the interface and detaches the PMMA layer with the graphene sample and Au alignment marks from the substrate. The PMMA stack is rinsed in deionized water and transferred atop a micro-fabricated device before drying out. While keeping the PMMA layer wet by adding deionized water sparingly, the graphene is aligned to the micro-fabricated device under an optical microscope by aligning the metal alignment marks attached to the PMMA layer to the metal alignment marks of the micro-fabricated device. This step can be done by manipulating the PMMA layer manually or using a micromanipulator. After evaporation of deionized water, the adhesion between the graphene sample and the micro-fabricated device is enhanced by annealing the device in vacuum at 150 ºC. The PMMA layer is dissolved in acetone to leave the graphene sample and metal alignment marks atop the device. Figure 3.6(d) shows a SEM of a graphene sample transferred to the central bridge of a suspended micro-fabricated device.

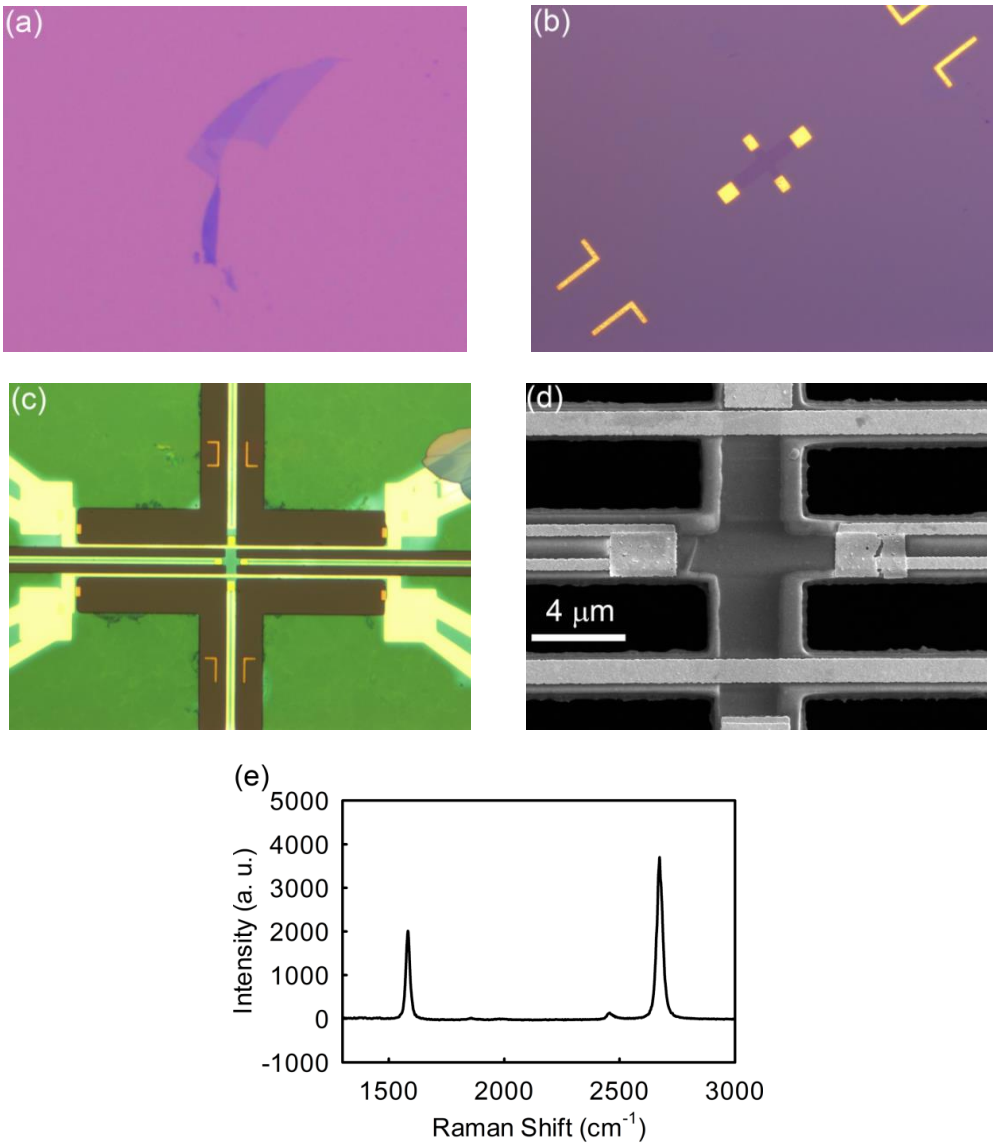

Figure 3.6: Aligned transfer of graphene to the device shown in Figure 3.5(c). (a) The exfoliated graphene sample. (b) Trimmed graphene with metal alignment marks. (c) Graphene and metal marks while supported by a PMMA layer are transferred and aligned to the device. (d) SEM image of the central bridge of the device after transferring graphene and removing PMMA. (e) Raman spectrum on the bridge that shows features of single-layer graphene.

3.2.5 Thermal Conductance Measurement

During the measurement, RT_1 (see Figure 3.2) is electrically heated with a power of Q, and the electrical resistances of all the RTs are measured and used to obtain average temperature rises in the metal lines ($\overline{\Delta T_i}$). When there is no heat generation in a metal line, $\Delta T_{im} = 2\,\overline{\Delta T_i}$ where ΔT_{im} is the corresponding temperature rise at the midpoint of the metal line. Since the device design is symmetric we assume that R_{b1}, R_{b2}, R_{b3}, and R_{b4} are similar and equal to R_b. Similarly, we can have $R_{s1} = R_{s2} = R_s$. Also, the transverse resistance thermometers are symmetric with resistance of R_t with $R_t = rR_b$. The proportionality factor r can be measured using the measurement method described in section 2.2.2. Based on the thermal circuit model and heat conduction analysis of the heater line, thermal resistances of the resistance thermometers and the center bridge can be determined from the measured data as

$$\begin{aligned} R_b &= 2\left(\Delta T_{1m} + \Delta T_{2m} + \Delta T_{3m} + \Delta T_{4m} + \frac{\Delta T_{t1m} + \Delta T_{t2m}}{r}\right) Q^{-1} \\ &\equiv Q^{-1} \sum \Delta T \end{aligned} \tag{3-12}$$

$$R_s = R_b \frac{\Delta T_c - \Delta T_{3m}}{\Delta T_{3m} + \Delta T_{4m}} \tag{3-13}$$

where

$$\begin{aligned} \Delta T_{1m} = 3\overline{\Delta T_1}/2 - (\Delta T_{2m} + \Delta T_{3m} + \Delta T_{4m})/4 \\ - (\Delta T_{t1m} + \Delta T_{t2m})/4r \end{aligned} \tag{3-14}$$

$$\Delta T_c = \frac{Q\,\Delta T_{3m}/2 + (\Delta T_{2m}\,\Delta T_{4m} - \Delta T_{1m}\,\Delta T_{3m})/R_b}{Q/2 + (\Delta T_{3m} + \Delta T_{4m} - \Delta T_{1m} - \Delta T_{2m})/R_b} \tag{3-15}$$

3.3 RESULTS AND DISCUSSION

In this work, we explore magneto-thermal measurements of electronic thermal transport in a bilayer graphene sample (20 μm x 6 μm) using the device shown in Figure 3.3. The magneto-thermal device is fabricated on a Si substrate covered with 300 nm thermally grown SiO_2, and a patterned bilayer graphene sample is transferred atop the device with the aligned transfer technique.

Figure 3.7(a) shows the correlation between the measured temperature rises of the RTs and the heat generation in RT_1. The slope of a linear fit to the data is used to obtain R_b according to equation (3-12). Similarly, the slope of a linear fit to the data shown in Figure 3.7(b) is used to obtain R_s/R_b. The correlation between the transverse temperature rise and the longitudinal temperature rise is shown in Figure 3.7(c). Also, the Seebeck coefficient was obtained based on the slope of a linear fit to data shown in Figure 3.7(d).

The results of magneto-thermal measurements for the bilayer graphene sample are summarized in Figure 3.8. The measured temperature-dependent thermal conductance of the bilayer graphene consistently reproduces the reported measurements for bilayer graphene in Chapter 2. As shown in Figure 3.8(a), the longitudinal thermal conductance does not show clear dependence on the perpendicular magnetic field for the bilayer graphene sample when no gate electric field is applied. The effect of magnetic field on electronic thermal transport has been masked by the large lattice contribution to thermal conductance of the graphene/SiO_2 bridge. Similarly, we do not observe the transverse temperature gradient that can be used to obtain k_{xy} and L_{xy} based on equation (3-10). As shown in Figure 3.8(b), the correlation between $\nabla_y T/\nabla_x T$ and B_z does not exhibit the linear trend suggested by equation (3-9). In comparison, the longitudinal Seebeck

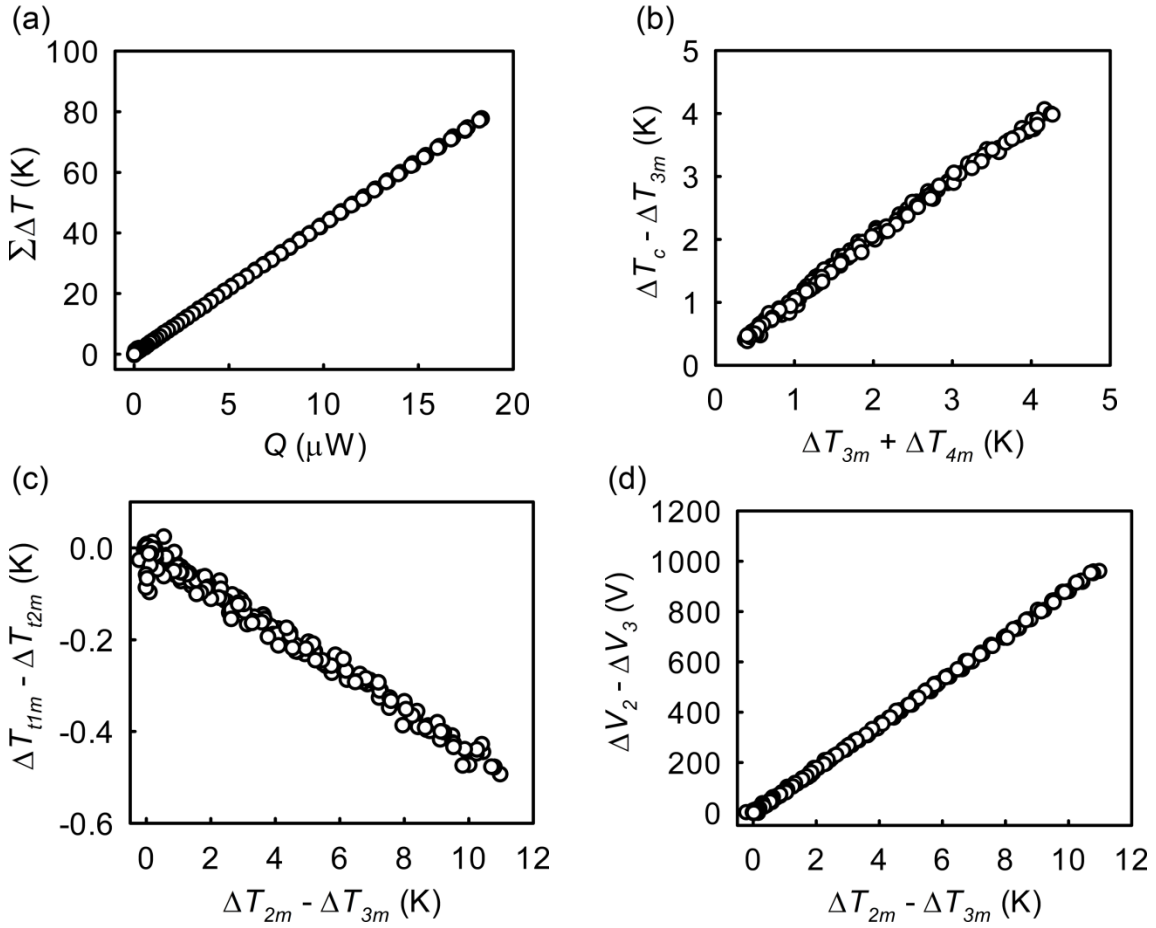

Figure 3.7: Analysis of the magneto-thermal measurement results at 150 K for a bilayer graphene sample. (a) The correlation between a combination of measured temperature responses of the RTs with heat generation in RT_1 to obtain R_b based on equation (3-12). (b) Correlation between the measured temperature responses of the RTs. The slope of a linear fit to the shown data obtains R_s/R_b based on equation (3-13). (c) The measured correlation between the transverse temperature rise versus longitudinal temperature rise. (d) The measured thermovoltage as a function of the measured longitudinal temperature rise along the graphene.

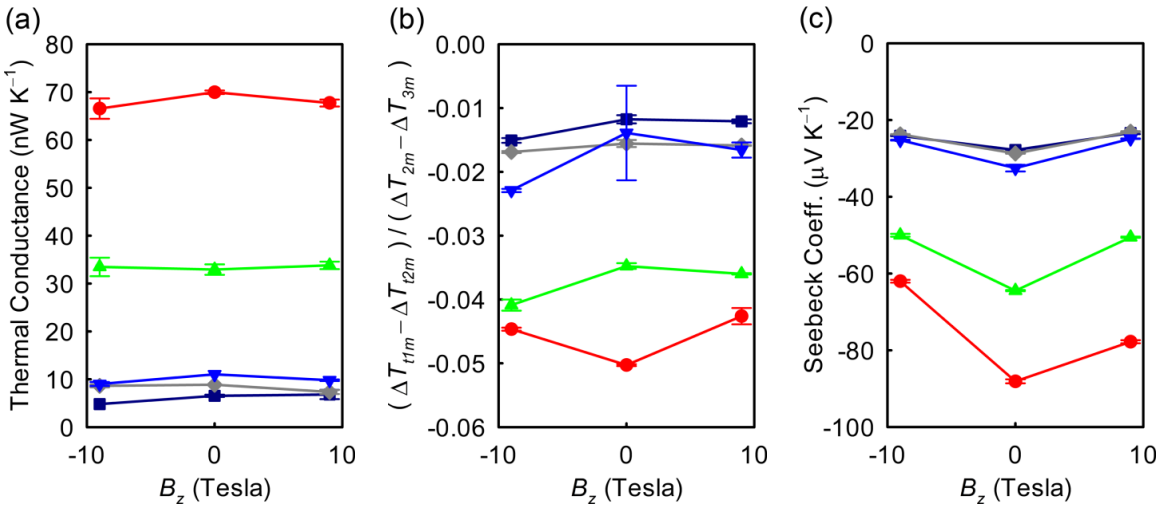

Figure 3.8: Measurement results for a bilayer graphene sample with intrinsic carrier concentration without an applied gate voltage. Measured thermal conductance of the central SiO_2 bridge covered with the graphene sample ($1/2R_s$) (a), the ratio of transverse temperature difference to longitudinal temperature difference (b), and Seebeck coefficient (c) are shown as a function of magnetic field at 32 K (dark blue squares), 43K (dark gray diamonds), 52 K (blue inverted triangles), 108 K (green triangles), and 157 K (red circles).

coefficient shows pronounced dependence on the magnetic field, shown in Figure 3.8(c), which indicates that electronic transport has been affected by the applied magnetic field.

These results suggests that the electronic thermal conductivity is negligible compared to the lattice contribution from the graphene and the SiO_2 support when no gate field is applied. Although k_{xy} and L_{xy} cannot be obtained based on the current results, a higher limit for κ_{xy} can be deduced. For example, based on Figure 3.8(b), for the measurements at 157 K the uncertainty in the measurement of

$(\Delta T_{t1m} - \Delta T_{t2m})/(\Delta T_{2m} - \Delta T_{3m})$ is ~0.01 or smaller, which is equivalent to $\nabla_y T/\nabla_x T$ of 0.03 or smaller based on the graphene dimensions. Since the $\nabla_y T/\nabla_x T$ signal from κ_{xy} is masked by the uncertainty in these measurements, we can assume that $\nabla_y T/\nabla_x T < 0.03$. Employing this inequality in equation (3-10) obtains the higher limit for κ_{xy} to be 15 W m $^{-1}$ K $^{-1}$ at 157 K by a magnetic field of 9 Tesla.

The transverse temperature gradient can be detected if $\nabla_y T/\nabla_x T > 0.1$. Figure 3.9 shows the results for calculation of $\nabla_y T/\nabla_x T$ based on equation (3-9) for a bilayer graphene sample supported by a SiO_2 membrane with the thickness of 300 nm with B_z of 9 Tesla at 157 K. Based on these results, in order to have $\nabla_y T/\nabla_x T = 0.1$, carrier concentration needs to be as large as 39.4 x 10^{11} and 9.8 x 10^{11} cm $^{-2}$ for mobility values of 5000 and 10000 cm ^{2} V $^{-1}$ s $^{-1}$, respectively. Given the capacitance of 11.5 nF cm $^{-2}$ for 300 nm SiO_2, this range of carrier concentration can be obtained by applying 55 and 14 V to the back-gate, respectively.

As explained in section 3.2.3, we developed a fabrication process that allows us to apply a back-gate to the suspended micro-heater thermometer devices. Figure 3.5 shows two fabricated devices with 30-40 nm Ti layer deposited at the backside to regulate carrier concentration. Figure 3.6 shows the device after a graphene sample is transferred atop the central bridge of one of the back-gated devices. Figure 3.10 shows modulation of electrical resistance using the back-gate voltage. Mobility (μ) can be obtained from the slope of conductance versus back-gate voltage (V_{gate}) using

$$\mu = \frac{1}{C_{mem}} \frac{d\sigma}{dV_{gate}} \tag{3-16}$$

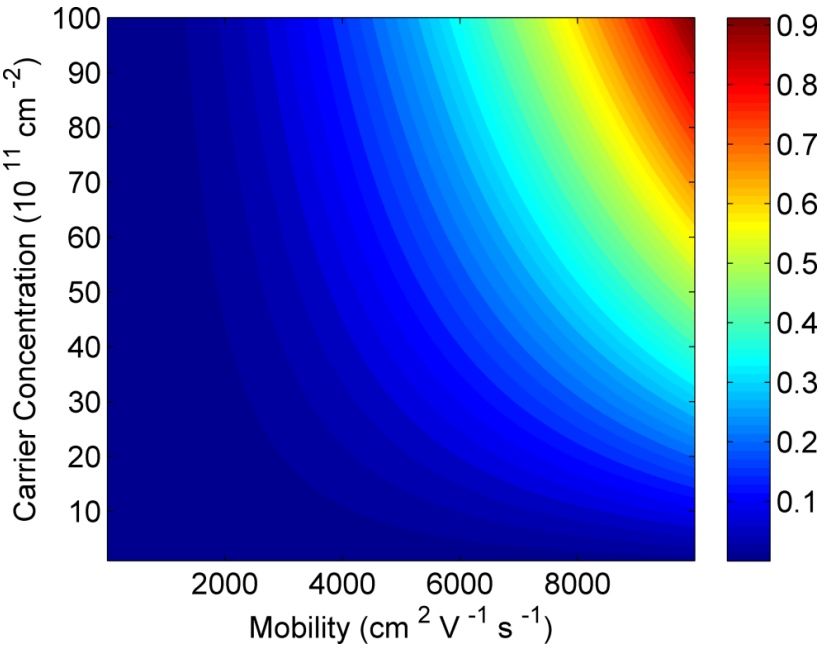

Figure 3.9: Calculated $\nabla_y T / \nabla_x T$ for a bilayer graphene sample at 157 K supported on 300 nm SiO_2 with applied magnetic field of 9 Tesla.

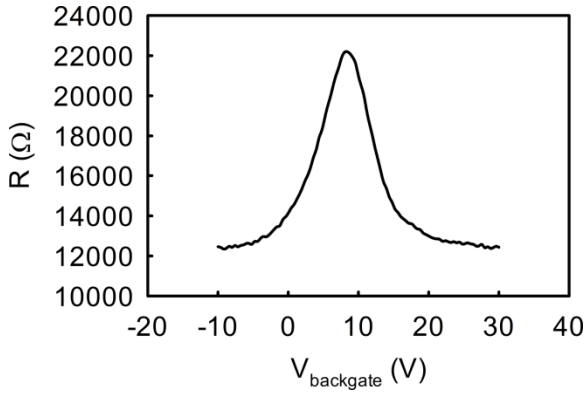

Figure 3.10: Electrical resistance of the transferred graphene measured as a function of back-gate voltage.

where C_{mem} is the capacitance of the supporting membrane. With a dielectric constant of 7.5 for Si_3N_4 and a thickness of 500 nm, C_{mem} is obtained to be 13 nF cm^{-2}. Electron and hole mobility is found to be 1100 and 900 $cm^2 V^{-1} s^{-1}$, respectively. The low values for mobility can be attributed to wrinkles and polymer residue on the graphene from the transfer process. To perform a quantitative investigation on electronic thermal transport in graphene, charge carrier mobility should be enhanced by employing cleaning and annealing processes.[103] For exfoliated graphene on SiO_2, the charge carrier mobility can be increased by an order of magnitude compared to the measured values.[104]

In addition to electronic thermal transport, these devices can be used to investigate thermogalvanomagnetic effects (section 3.2.2) in graphene and other layered materials. The resistance-thermometers at both ends of the central bridge of the device can be used to generate a longitudinal current flow or temperature gradient while the transverse resistance thermometers can measure the transverse electrostatic potential or temperature gradient that is caused by the applied magnetic field. Such measurements can be conducted on a single sample through a single measurement, which provides critical experimental data to investigate transport of electrons and phonons.

3.4 SUMMARY

We developed and implemented an experimental method to investigate electronic thermal transport in layered materials such as graphene under a temperature gradient in presence of electric and magnetic fields by measuring longitudinal and transverse thermal conductivity, longitudinal and transverse electrical conductivity, and thermogalvanomagnetic effects. Investigation of all these properties in a single sample

through a single measurement would obtain useful information to perform rigorous investigations on the transport of electrons and phonons without the effects of sample-to-sample and measurement-to-measurement variations. We employed this measurement technique for a bilayer graphene sample to study electronic thermal transport. The electronic contribution to thermal conductivity of graphene was found to be negligible compared to the contribution of phonons, and a higher limit for the transverse electronic thermal conductivity was obtained. The Seebeck coefficient of the bilayer graphene sample as a function of transverse magnetic field was also measured.

To perform quantitative measurements on electronic thermal transport in graphene using the approach presented here, contribution of electrons to thermal transport should be increased by increasing charge carrier concentration and mobility. In this work, design and fabrication of suspended micro-thermometer devices with back-gate was demonstrated. Enhancing charge carrier mobility is achievable by performing further annealing and cleaning processes on the graphene. In addition, the sensitivity of the micro-thermometer devices can be improved by reducing thermal conductance of the suspended beams using a metal with low thermal conductivity for resistance-thermometers such as Pd instead of Au as well as reducing the thickness and thermal conductivity of the suspended beam below the graphene sample.

Chapter 4: Quantitative Scanning Thermal Microscopy of Flexible Graphene Devices

4.1 INTRODUCTION

Understanding the physics of thermal transport at the nanoscale has become important for the design and optimization of many advanced technologies that are being actively explored, such as thermal barriers, heat-assisted magnetic recording, high efficiency thermoelectrics, phase-change memory, and renewable energies.[1-4] Thermal management of nanoelectronics is an obvious example where miniaturization of electronics aiming for higher performance and lower cost has led to an unprecedentedly high power density, which restricts performance and reliability.[6,7] Probing the temperature distribution in nanostructured devices provides useful insights into nanoscale energy transport and conversion. Furthermore, obtaining the temperature distribution with high resolution can help to reveal failure mechanisms, predict device reliability, and optimize device performance. For example, the temperature distribution in nanoelectronic devices is valuable for discovering the mechanisms behind hot spot formation and for illustrating the heat dissipation pathways, which is vital information needed for minimizing the intensity of hot spots and optimizing device performance and reliability.

Several optical thermometry techniques such as micro-Raman thermometry, optical emission thermometry and infrared thermal microscopy have been used to measure the temperature distribution of electrically biased graphene devices. The Stokes to anti-Stokes intensity ratio of the G peak of the Raman spectrum of graphene was used to measure the temperature of high-energy zone center optical phonons (G mode) with

resolution of ~100 K.[27,29,105,106] Other reports used the temperature dependent frequency of the G peak and 2D peak of the Raman spectrum of graphene[107] to measure the temperature of intermediate frequency phonons to which G phonons and 2D phonons anharmonically couple, respectively.[27,29,108] The electronic temperature of graphene was also probed via optical emission thermometry with ~100 K resolution by fitting the measured optical emission with Planck's law.[29] Improved temperature resolution was achieved by measuring infrared (IR) emission and IR thermal images were obtained with a spatial resolution of a few micrometers.[27,28] Berciaud et al. obtained the temperature distribution of electrically biased graphene using optical emission thermometry, Stokes to anti-Stokes intensity ratio and G peak shift in Raman spectrum of graphene. They found that the high-energy G mode phonons are in thermal equilibrium with electrons, but not with lower-energy phonons.[29] Infrared thermometry has been used to show that the hot spot location along a graphene channel depends on the gate and source biases, which influence the carrier concentration distribution along the channel.[27,28] These measurements have provided significant insights into the underlying physics of thermal transport in graphene. However, the spatial resolution of these far-field optical techniques is limited by the diffraction limit and comparable to the optical wavelength. This limitation results in a spatial resolution of ~1 μm and restricts our understanding of thermal phenomena occurring at smaller length scales. With nanoscale feature sizes of current-generation electronic devices,[5] probing the temperature distribution of such devices requires other thermometry techniques with superior spatial resolution.

Scanning probe microscopy (SPM) techniques[109] such as scanning thermal microscopy (SThM) and scanning Joule expansion microscopy (SJEM) have been

employed successfully to investigate thermal behavior of devices with higher lateral spatial resolution compared to optical thermometry methods. Scanning probe microscopy is a measurement method based on scanning tunneling microscopy (STM) and atomic force microscopy (AFM). These methods work by probing the surface of a device using a very sharp tip. In one of the SThM methods, a miniature thermocouple located at the apex of an AFM tip is scanned over the surface of the device. Local heat transfer between the tip and the surface of the device changes the temperature of the thermocouple. The measured thermovoltage map can be calibrated to produce a temperature map. However, since the thermovoltage map depends on the heat transfer between the tip and the sample, it can be distorted by a number of parameters that affect tip-sample thermal resistance, including the topography and surface chemistry. Moreover, parasitic heat transfer through the air gap between the probe and the device may considerably distort the measured thermovoltage and makes it challenging to obtain accurate quantitative results.[110] Meanwhile, the phonon transmission coefficient across a weakly bonded interface is inversely proportional to the square of the phonon frequency,[17,66] and the local temperature measured by the thermocouple tip at low contact force to the sample is dominated by contributions from low-frequency phonons, provided parasitic heat transfer through the air gap can be eliminated. In previous works, SThM measurements were used to obtain the temperature distribution in graphene channels with spatial resolution of ~100 nm.[30,111] By comparing thermal maps of graphene channels obtained from SThM and micro-Raman thermometry, Jo et al. found that low-frequency phonons are in thermal equilibrium with higher frequency phonons that are anharmonically coupled to 2D phonons.[30]

Alternatively, there can be a miniature heater-temperature sensor at the apex of a SThM tip. Heating the heater at constant power and monitoring the temperature while the tip is scanned over a surface in contact mode would allow analysis of thermal properties of the surface. Pumarol et al. reported the measurement of thermal conductance in suspended and supported graphene samples using this method.[112] Menges et al. reported on increased thermal conductance of supported graphene using vacuum-operated SThM measurements.[113] In comparison to SThM, SJEM operates by scanning an AFM tip in contact with the surface of a device under periodic heating to obtain the temperature distribution from the measured thermomechanical expansion distribution of a polymer layer coated on the device.[109] SJEM measurements were used to study Joule heating and thermoelectric phenomena at graphene-metal contacts and resistive heating at graphene wrinkles and grain boundaries.[114,115]

These prior reported efforts on obtaining temperature distributions of graphene devices supported on a substrate have been limited to the case where graphene is supported on ~90 nm or ~300 nm SiO_2, which makes graphene visible and also allows for tuning of the charge carrier concentration in graphene using a back-gate voltage. Recently, transparency, stretchability, and elasticity of graphene have attracted many researchers to employ graphene for flexible electronics,[16,22-24] a very active area for future electronics. Flexible electronic devices are mainly fabricated on polymer substrates with thermal conductivity values smaller than that of silicon by three orders of magnitude. In addition, the glass transition temperature for polymer substrates can limit the safe operating temperature of the device. While thermal management is already a major roadblock for further improvement of performance and reliability of Si-based electronic

devices,[7] the low thermal conductivity and limited allowable temperature rise of polymer substrates give rise to significant thermal management issues in flexible electronic devices. As one of the first steps of addressing such issues, it is necessary to obtain the temperature distribution on flexible electronic devices, which remains elusive.

4.1.1 Present Work

In this chapter, we present quantitative SThM measurements to obtain high-resolution temperature distribution in electrically biased graphene devices supported on flexible polyimide substrates. It is found that the large heated area in flexible electronic devices causes considerable challenges in high-resolution quantitative thermal imaging with SThM, including large parasitic heat transfer and high temperature rise. These challenges are addressed in this work by a triple scan technique to carefully eliminate the parasitic heat loss, and by a detailed study of the tip-sample thermal conductance as a function of sample temperature. The applicability and limitation of a calibration method based on a heater-thermometer metal line is evaluated. Furthermore, a null method SThM technique based on heating of the tip with a laser is developed to measure the local temperature of devices without the need for a separate calibration. This laser-heated SThM approach was implemented to study the temperature distribution on flexible graphene devices and to verify the calibrated triple scan SThM measurement results. The obtained measurement results reveal that the temperature rise in the flexible graphene devices is more than one order of magnitude higher than that reported for graphene devices fabricated on a silicon substrate, and that lateral heat spreading is a more

important heat dissipation pathway for devices on the flexible substrate than on the silicon substrate.

4.2 SCANNING THERMAL MICROSCOPY

In SThM, a miniature thermocouple located at the apex of an AFM tip is scanned over the surface of a device. Heat transfer between the tip and the device changes the temperature of the thermocouple, and a thermovoltage map with very high lateral resolution is generated. The thermovoltage map and its lateral resolution depend on the relative contribution and length scale of heat transfer mechanisms between the tip and the device surface, which are shown in Figure 4.1.[109,110] Solid-solid conduction is the heat conduction through the tip-sample contact area. It is a highly localized heat transfer mechanism with length scale on the order of the tip-sample contact area. Under ultrahigh vacuum conditions where solid-solid conduction is the dominant heat transfer mechanism, SThM can obtain ~10 nm spatial resolution.[116] Although this length scale is highly desirable, solid-solid conduction is not the dominant heat transfer mechanism in ambient conditions. Because of condensation of water molecules and other adsorbates on the surface of the tip and device, a liquid bridge surrounds the tip-sample contact area. The heat conduction through this liquid film was found to be important for ambient SThM measurements and sub-100 nm spatial resolution has been reported.[110,117] Far-field and near-field radiative heat transfer mechanisms have been estimated to be negligible compared to other heat transfer mechanisms when the tip and sample are close to room temperature.[109] Heat conduction through the air gap between the tip and sample often provides a major contribution to ambient SThM measurements. Since it is a non-local

signal from the whole heated area on the surface, the ambient SThM signal depends on the size of the heated area on the sample.[110]

For SThM measurements in ambient conditions, the thermovoltage signal is dominated by the heat transfer contributions through the liquid film and air. The presence of a non-local signal via air conduction distorts the high-resolution thermovoltage signal via liquid film conduction. This non-local parasitic signal should be eliminated to obtain a local thermovoltage signal that can be employed for quantitative SThM measurements of the local temperature of the sample.

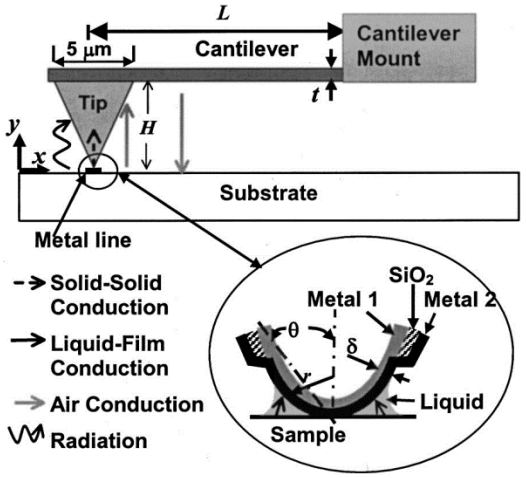

Figure 4.1: Mechanisms of heat transfer between the SThM tip and the device surface. Adopted from Shi et al.[110]

4.2.1 Quantitative Scanning Thermal Microscopy

For quantitative SThM measurements, it is necessary to eliminate the non-local signal via air conduction from the thermovoltage signal. This allows one to obtain high

resolution quantitative thermal maps that cannot be obtained with other thermometry techniques. This key step can be taken by conducting SThM measurements under vacuum conditions.[116,118] For ambient SThM, the thermovoltage can be interpreted by performing calibration measurements with other low-resolution thermometry techniques such as micro-Raman thermometry.[111] In comparison, Kim et al. proposed a SThM technique to eliminate the parasitic air conduction signal by scanning the tip in contact and at a fixed height above the sample.[119,120] They showed that the local temperature rise (ΔT_s) can be obtained by measuring the temperature rise of the thermocouple in contact mode ($\Delta T_{t,c}$) and non-thermal contact mode ($\Delta T_{t,nc}$). In the contact mode where the tip is in contact with the surface of the device, there is heat transfer at the tip-surface contact ($Q_{ts} \neq 0$). In comparison, the non-thermal contact mode represents a thought experiment where the local heat transfer through solid-solid and liquid film conduction is absent, namely $Q_{ts} = 0$, even though the cantilever-sample spacing remains the same as that in the contact mode. Therefore, the heat transfer through the air is the same for the two cases. It can be derived that the local surface temperature rise of the device is given by the following relationship[120]

$$\Delta T_s = \Delta T_{t,c} + \varphi\left(\Delta T_{t,c} - \Delta T_{t,nc}\right) \quad , \quad \varphi \equiv R_{ts}/C \tag{4-1}$$

where R_{ts} is the thermal resistance at the contact of the tip and the surface, and C is a constant with units of K W $^{-1}$. It can be shown that C depends on the probe's dimensions and material properties, and effective local heat transfer coefficient between the probe and its surroundings including the sample, but not the temperature distribution of the sample. If φ can be determined from a calibration, ΔT_s can be obtained by measuring $\Delta T_{t,c}$ and $\Delta T_{t,nc}$.

4.3 SCANNING THERMAL MICROSCOPY OF FLEXIBLE GRAPHENE DEVICES

A quantitative SThM technique is established in this work to measure the temperature distribution on flexible graphene devices fabricated on polyimide substrates under operating conditions, as discussed below.

4.3.1 Measurement Setup

The measurement setup consists of a MultiMode AFM with the Nanoscope IIIa controller (Digital Instruments) equipped with a Signal Access Module. The SThM probe is a custom-made AFM probe with SiN_x V-shape cantilever and a SiO_2 tip, as shown in Figure 4.2.[121,122] A sub-micron Pt-Cr thermocouple is fabricated at the apex of the SiO_2 tip. At the apex of the tip, the tip radius is 20 nm and can map a thermovoltage signal with a spatial resolution of 50 nm. The thermopower of the Pt-Cr junction was measured to be 13.4 μV/K.[110] Making contact with the surface of the device does not modify the thermopower value since the thin native oxide layer of Cr electrically insulates the junction from the surface of the device. In these experiments, the electrical insulation is further enhanced by atomic layer deposition (ALD) of 20 nm Al_2O_3 on the probe at 250 °C using trimethylaluminum (TMA) and water as the precursors. Before SThM measurements, the effectiveness of the insulating layer is verified by measuring the electrical resistance between the tip and a conducting sample. Furthermore, raising the electrostatic potential of the sample without flowing any electrical current through the sample does not change the measured thermovoltage of the thermocouple.[121] The SThM probe is mounted on a custom-made AFM tip holder, which provides electrical connections to the SThM probe, as shown in Figure 4.3(a). The two terminals of the

thermocouple are wire-bonded to two metal plates on the tip holder. The thermovoltage signal is amplified using a SR 560 voltage preamplifier and connected to the Signal Access Module of the AFM. The angle between the probe and the surface of the sample is adjusted by an Al wedge on the tip holder, as shown in Figure 4.3(b). The angle is adjusted to be 11 degrees to reflect the laser to photodetector of the AFM.

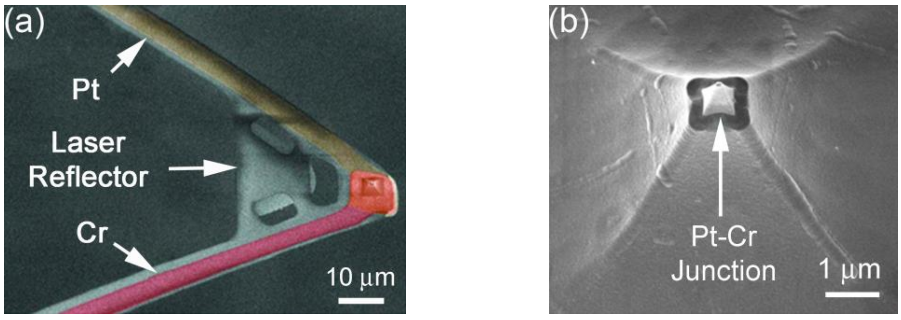

Figure 4.2: Scanning electron micrograph (SEM) of the SThM probe (a) and its SiO_2 tip with a Pt-Cr thermocouple (b).

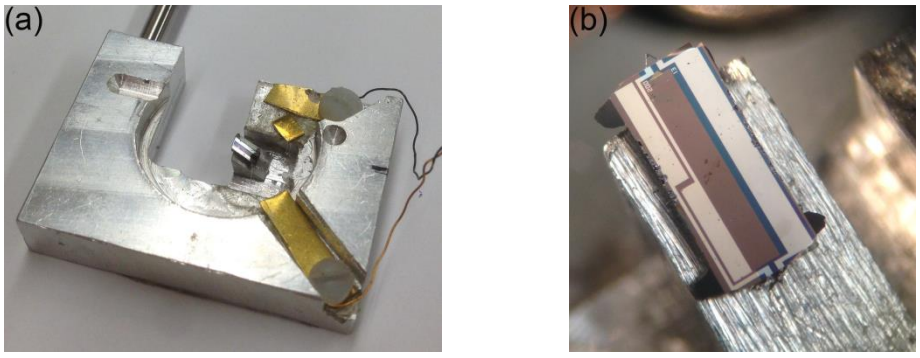

Figure 4.3: (a) Optical image of the SThM probe holder with metal plates connected to terminals of the thermocouple. (b) Optical micrograph of SThM probe aligned using an Al wedge on the tip holder.

4.3.2 Flexible Graphene Devices

The flexible graphene devices measured in this work have been fabricated by Saungeun Park in Prof. Deji Akinwande's group. The flexible graphene devices consist of graphene channels contacted by metal electrodes on a flexible polyimide substrate. A fabricated device is shown in Figure 4.4(a). During the fabrication process, liquid polyimide is spun over a polyimide sheet with 125 μm thickness and cured at 300 °C to achieve a RMS roughness better than 1 nm.[123] The process is repeated for the other side of the polyimide sheet to prevent bending of the substrate because of thermal stress of the curing process. Atomic layer deposition (ALD) is employed to deposit 20 nm of Al_2O_3 on the substrate. Single layer graphene, grown on copper foil by chemical vapor deposition, is transferred on the Al_2O_3/Polyimide substrate via poly(methyl methacrylate) (PMMA) assisted wet transfer process.[124] Electron-beam lithography (EBL) followed by oxygen plasma is employed to define active graphene channels. Another EBL step followed by e-beam evaporated metal deposition (2 nm Ti, 40 nm Au) is used to define source and drain metal fingers and metal contacts.

We cut the devices and load them into a device stage with electrical connections as shown in Figure 4.4(b). A wire-bonder machine is used to connect the contact pads on the graphene device to the bonding pads of a chip carrier. Because the flexible graphene device is too soft for wire bonding, 25 μm thick bonding wires are attached to the bonding pads of the chip carrier with the use of the wire bonder. Manual micro-soldering is used to attach the other end of each bonding wire to a contact pad on the device. Conductive paint is used to attach a thin film of solder, with a size comparable to the size of the contact pads, to the contact pads. A micro-soldering iron is built by mounting a 160

μm thick wire to the tip of a fine soldering iron, and is used to solder the bonding wires to the solder films attached to the contact pads. Prior to wire bonding the device to the chip carrier, manual soldering is used to connect 160 μm thick wires to the side contact pads of the chip carrier. The electrical wires are connected to external electronics through a BNC box to apply and measure voltage biases and electrical currents.

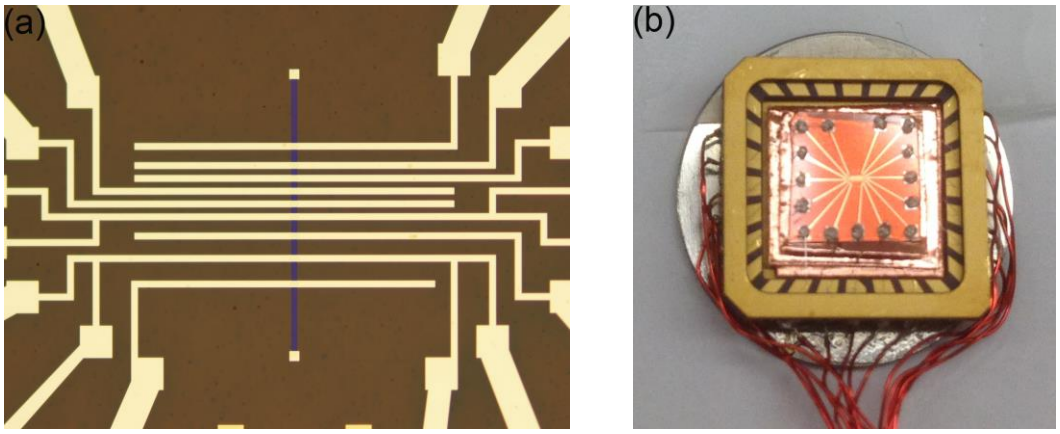

Figure 4.4: (a) Optical micrograph of a flexible graphene device on polyimide substrate. The graphene channels are shown by false blue color. The channel width for the graphene channels and metal fingers is 10 μm. (b) A flexible graphene device mounted on a device stage.

4.3.3 Calibration Using a Resistance-Thermometer Metal line

As equation (4-1) indicates, measuring the local temperature rise ΔT_s using SThM requires knowledge of $\Delta T_{t,c}$, $\Delta T_{t,nc}$ and the calibration parameter φ. Figure 4.5 shows the deflection and thermovoltage of the SThM probe when a Joule-heated graphene or Au sample approaches or retracts from the probe. The thermovoltage signal can be converted

to the thermocouple temperature rise using the thermopower of the Pt-Cr junction. As the graphene sample approaches the tip, the thermocouple temperature increases because of the parasitic heat transfer through the air. Once the sample is very close to the tip, the tip jumps into contact with the surface because of capillary forces. This phenomenon causes a jump in the thermocouple temperature from point C to point D. The thermovoltage does not change appreciably by increasing the tip-sample contact force, as indicated by the measured thermovoltage when the scanner is moved beyond the jump-to-contact point. It should also be noted that the tip-sample contact force is minimized during measurements to avoid any damage to the sample and the tip. Hence, during the scanning $\Delta T_{t,c}$ is measured at a point (D') near point D with the tip in contact with the sample.

Measurement of $\Delta T_{t,nc}$ requires additional efforts since the cantilever-sample distance should remain the same as that for point D' yet the local tip-sample heat transfer must be absent. Although this condition is nearly met at point C, the tip cannot be held in this state while scanning over the sample. Some prior studies have used the tip temperature when the probe is lifted at a fixed height above the sample to obtain $\Delta T_{t,nc}$.[30,119] However, Figure 4.5(a) shows that this assumption can lead to a considerable error when the parasitic heat transfer increases rather rapidly with decreasing tip-sample distance, which can occur when the heated area on the sample is large. Here, the thermovoltage difference between point D and point B at 100 nm lift height or point A at 400 nm lift height is 12.4 μV or 28.5 μV, respectively, and is considerably larger than the thermovoltage jump of about 8 μV between point D and point C, because of the presence of a large contribution from the parasitic air gap heat transfer in the two larger thermovoltage difference signals. The presence of residual parasitic air conduction in the

measured $\left(\Delta T_{t,c} - \Delta T_{t,nc}\right)$ value can lead to underestimation or overestimation of the sample temperature depending on the calibration method.

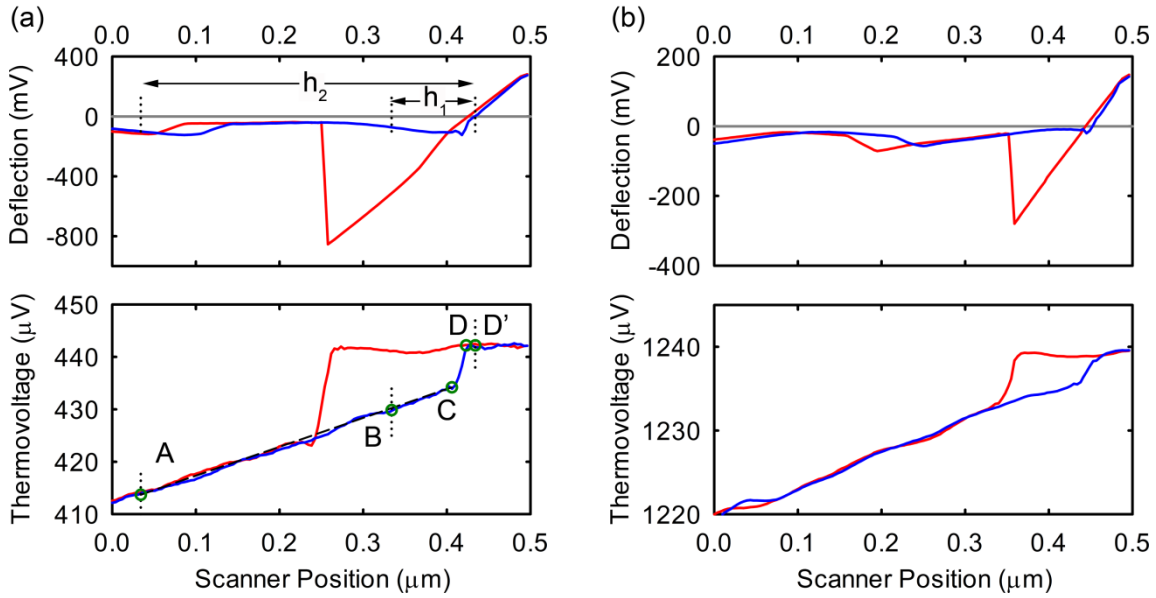

Figure 4.5: Cantilever deflection and thermovoltage signal of the SThM probe as a function of the sample position when the sample approaches (blue curve) or retracts (red curve) from the probe. The samples are a graphene channel (a) and an Au line (b). Points A and B denote the measured thermovoltage signal if the tip is lifted by 400 nm (h_2) and 100 nm (h_1) from point D', respectively. Points C and D denote the measured thermovoltage signals before and after the jump-to-contact phenomenon.

In this study, we use a triple scan technique[120] to obtain the thermovoltage jump. In this method, we measure the thermovoltage signal at two different lift heights, A and B, in addition to the thermovoltage signal measured in the contact mode. Linear extrapolation through these lift mode thermovoltage signals would obtain the

thermovoltage signal at point C, which only accounts for the thermovoltage signal caused by the parasitic heat transfer. This triple scan approach is necessary to eliminate the parasitic air conduction signal from the measured thermovoltage and to obtain a calibration parameter that does not depend on the temperature distribution and size of the heated area of the device.

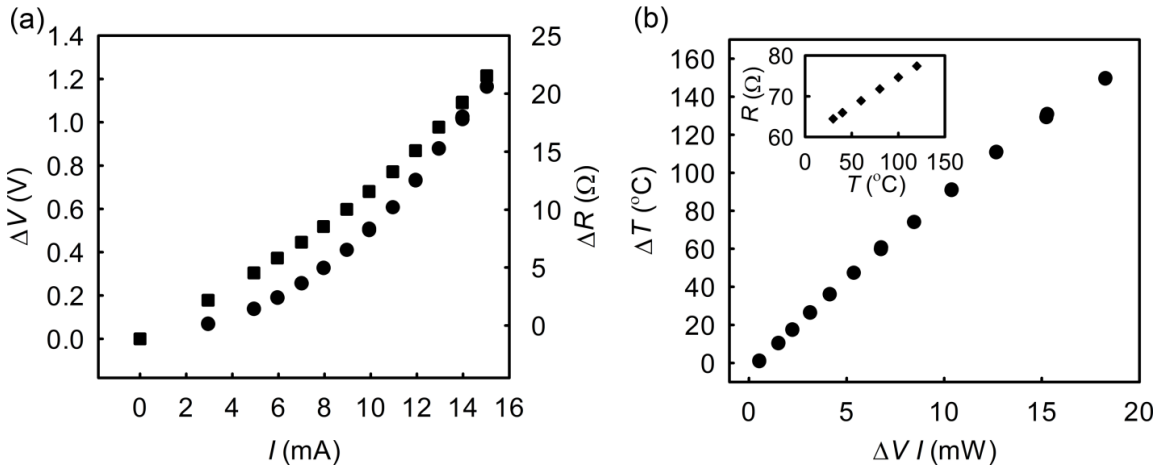

Figure 4.6: Temperature measurements using the metal line heater and resistance thermometer. (a) IV curve (squares) and resistance change (circles) as a function of the electrical current. (b) The metal line temperature rise as a function of power. The temperature rise is obtained from the change in resistance in (a) and the temperature coefficient of resistance (TCR) of the metal line. The inset shows the TCR measurement results.

To convert the measured thermovoltage jump to temperature, the calibration factor for the Au surface (φ_{Au}), is determined by performing SThM measurements on a 550 μm long, 10 μm wide metal line heater and resistance thermometer. As shown in Figure 4.6, the change in the electrical resistance of the Au line is measured as a function of the electrical current. In addition, the temperature coefficient of resistance (TCR) of the metal line is measured in a furnace and used to correlate the average temperature rise in the metal line from the measured resistance. With known ΔT_s and obtaining $\Delta T_{t,c}$ and $\Delta T_{t,nc}$ from SThM measurements, the calibration factor φ_{Au} is determined using equation (4-1).

Figure 4.7(a) shows the analysis of the results of $\left(\Delta T_{t,c} - \Delta T_{t,nc}\right)$ determined from double scan, triple scan, and quadruple scan measurements. For quadruple scan measurements, the measured thermovoltage at three lift heights are used for a linear extrapolation to point C, whereas the thermovoltage of point C is assumed to be the same as that measured directly at a single point at a specified lift height for the double scan measurement. Based on equation (4-1), φ_{Au} can be determined from the slope of a plot of $\left(\Delta T_s - \Delta T_{t,c}\right)$ versus $\left(\Delta T_{t,c} - \Delta T_{t,nc}\right)$. For double scan measurements, the obtained value for φ_{Au} depends on the lift height, which indicates the contribution of residual parasitic heat transfer through the air. In comparison, triple scan and quadruple scan measurements find similar values for φ_{Au} (110 ± 5) within the uncertainty range of the measurements. This result verifies the linearity assumption of the triple-scan measurement method and the effectiveness of the triple-scan method to obtain the thermovoltage jump.

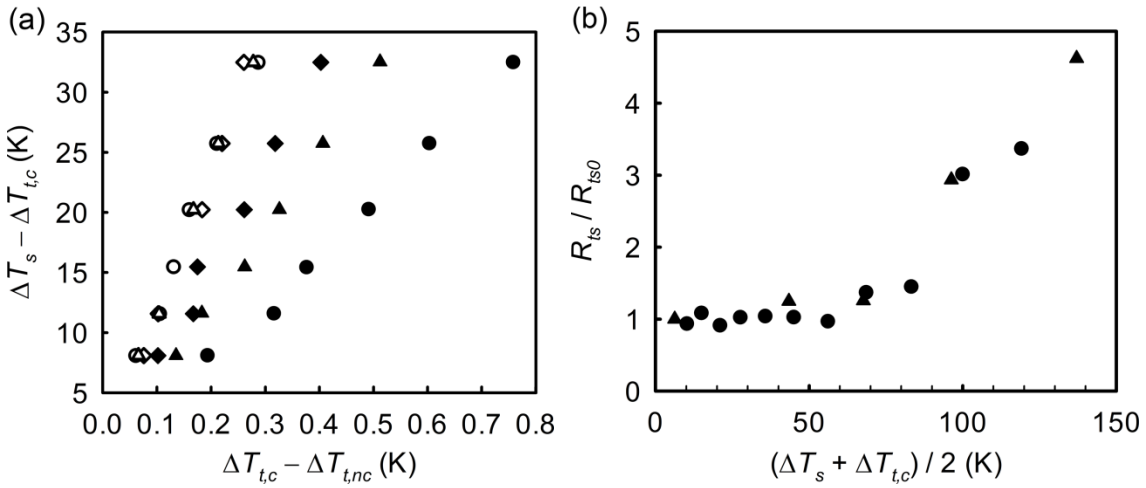

Figure 4.7: Analysis of SThM measurements on a long metal line to obtain the calibration parameter φ based on equation (4-1). Panel (a) shows the results for double scan measurements with lift heights of 400 nm (filled circles), 200 nm (filled triangles), and 100 nm (filled diamonds), and triple scan measurements with lift heights of 100 nm and 200 nm (unfilled diamonds), and 100 nm and 400 nm (unfilled triangles), and quadruple scan measurements with lift heights 100 nm, 200 nm and 400 nm (unfilled circles). Panel (b) shows the tip-sample thermal resistance normalized by its value at room temperature as a function of the average temperature rise in the thermocouple and the metal line for two Au lines.

It is important to investigate the variability of φ under different measurement conditions. Parameter φ is defined as R_{ts}/C where C can be assumed constant for a specific probe. However, R_{ts} can be influenced by measurement parameters. Solid-solid conduction depends on structural and thermal properties of the surfaces, contact force, and temperature. First, the contact area of a sphere and a plane under a normal force F is expected to increase by $F^{2/3}$.[125] However, Figure 4.5 shows that increasing the tip-

sample contact force does not appreciably change the temperature of the thermocouple within the range of the contact force tested. The temperature of the thermocouple remains constant over a large variation of the tip-device contact force, from the point where the tip jumps to contact on the approach curve until it snaps out of contact on the retract curve. Similar measurements at higher temperatures show similar insensitivity of the measured temperature to the contact force. Moreover, in all SThM measurements for calibration and thermal mapping purposes, the contact force has been adjusted to obtain a minimal and consistent contact force for all the measurements.

The observed insensitivity on the contact force can be caused by the dominant heat transfer pathway through the liquid meniscus around the tip compared to the solid-solid conduction. Thermal conduction through the liquid film depends on several parameters. When the tip is in contact with the sample, the lateral size of the liquid film and the capillary force are functions of the tip radius, contact angles of the liquid meniscus with the tip and the sample, temperature, and relative humidity.[126] The liquid film conduction can be determined from the meniscus dimensions, thermal conductivity of the liquid, and the thermal interface resistance at the liquid-solid interfaces. For example, the temperature at the tip-sample junction affects the size of the liquid film,[127] which alters the thermal resistance of the film. Surface temperature rises can change the liquid film conduction by changing the contact angels[128] and the local relative humidity. We investigated the effect of temperature through calibration measurements at different surface temperatures over two heater-thermometer metal lines. Figure 4.7(b) shows that for Au lines, the measured thermal resistance between the SThM tip and the Au ($R_{ts,Au}$) and the calibration factor φ_{Au} does not change noticeably until $\left(\Delta T_s + \Delta T_{t,c}\right)/2$ reaches

~60 K, upon which there appears to be a small increase of $R_{ts,Au}$ with increasing average temperature rise up to ~85 K. An apparent jump in $R_{ts,Au}$ occurs in the interval of 85−95 K, beyond which $R_{ts,Au}$ increases appreciably with increasing temperature. Based on this result, φ_{Au} obtained through Figure 4.7(a) remains nearly constant when the temperature rise of the meniscus is less than 60 K above ambient, or less than a temperature of 80 °C despite the effects of temperature on the size of the liquid meniscus which renders itself in temperature-dependent capillary force.

Furthermore, we have investigated whether the calibration factor can change as the tip moves from the Au surface to an adjacent graphene surface. We have performed calibration measurements at the edge of the heater-thermometer Au line where the line crosses over a graphene sample. The temperature of the graphene at a location several hundreds of nanometers away from the edge of the metal line is expected to be close to the temperature of the metal line on account of the cylindrical heat dissipation pathway through the relatively thick polyimide substrate with low thermal conductivity. If the graphene temperature is assumed to be the same as the metal line temperature, the obtained calibration factor for graphene (φ_{gr}) is found to be similar to φ_{Au} despite their different surface properties. It is worth noting that graphene is supported on a layer of ALD-deposited Al_2O_3 with a thickness of 20 nm, which can affect the contact angle of the liquid meniscus with graphene.[129,130] In addition, it is expected that PMMA residue can be present on the graphene surface and the thickness of the PMMA residue layer can be about 1-2 nm.[131,132] PMMA residue is also likely present on the Au surface. Moreover, the capillary force values between the SThM probe and graphene and the Au calibration line has been measured in this work. As the sample is moving away from the cantilever,

the cantilever deflects by the capillary force until a point where the cantilever snaps out of the contact. The maximum deflection signal of the cantilever by the capillary force is 633 mV and 607 mV for Au and graphene at room temperature, respectively. Therefore, the contact angle on graphene/ALD Al_2O_3 and Au can be similar. These factors can explain the similar calibration factors found on the Au and graphene sample.

In this work, the contact force of the probe is consistently controlled to a minimum value just enough to make contact with the sample to prevent tip wear. In addition, the obtained calibration parameters are compared before and after the thermal mapping to ensure that the parameter has not changed because of tip wear.

4.3.4 Laser-Heated Scanning Thermal Microscopy

In order to further validate the triple scan calibration and measurement method, a different measurement technique has been developed. In this technique, the tip is brought into contact with the surface of the operating electronic device to obtain the thermovoltage jump from the measured approach curve as shown in Figure 4.5(a). After the temperature of the tip is changed by changing the AFM laser power incident on the AFM cantilever, the thermovoltage jump is measured again, and the process is repeated for several temperatures of the tip under different laser heating powers. The incident laser power can be adjusted by either tuning the laser output power, or by placing glass slides with different metal coating thicknesses between the laser and the AFM cantilever. The change in the laser power alters the tip temperature with negligible effect on the temperature distribution of the sample. Increasing the temperature of the tip decreases the temperature jump, and at a certain laser power no temperature jump occurs. This is the

point where the temperature of the tip is equal to the local temperature of the sample. This conclusion is supported by equation (4-1), where the same values for $\Delta T_{t,c}$ and $\Delta T_{t,nc}$ results in the same values for ΔT_s and $\Delta T_{t,c}$ regardless of the value for φ. This measurement technique is essentially a null point method,[133,134] which means that the temperature of the tip is measured when the tip-sample heat transfer is zero. As such, the measured temperature is not affected by variations in R_{ts} and heat spreading of the sample. This provides a facile, useful means for interpretation and calibration of SThM measurements.

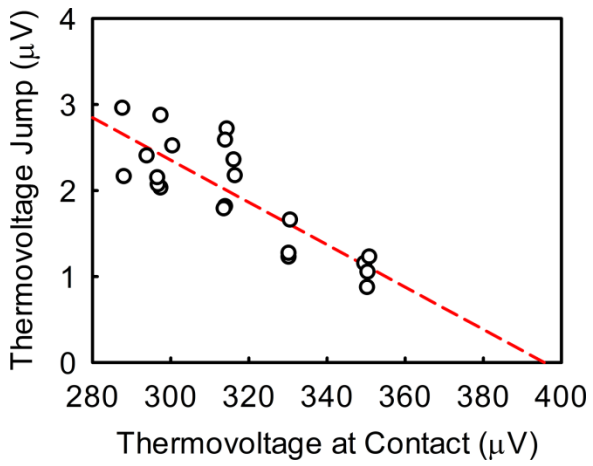

Figure 4.8: Laser-heated SThM to obtain the temperature rise at the center of a 10 x 10 μm ^{2} graphene channel with a power dissipation density of 895 W cm $^{-2}$. The measured variations of the thermocouple thermovoltage in the contact mode and the thermovoltage jump at different incident laser powers are shown. The red dashed line shows the extrapolation line to find the thermovoltage of the thermocouple that corresponds to zero thermovoltage jump. At this point, the local temperature of the sample is equal to temperature of the thermocouple.

We employed the laser-heated SThM technique to measure the temperature at the center of the 10 x 10 μm^2 graphene channel on polyimide shown in Figure 4.10(a). The measurement results are shown in Figure 4.8. Increasing incident laser power decreases the thermovoltage jump. Using the extrapolation line shown, we find that the thermovoltage jump is zero when the thermovoltage in contact mode is 396 μV, which gives ΔT_s to be 29.6 ± 3.6 K. Interpreting SThM measurements by employing equation (4-1) with the calibration factor for the metal line φ_{Au} obtains ΔT_s to be 29 ± 1 K. This result verifies that the Au line calibration properly works for the graphene sample.

4.3.5 Thermovoltage Maps and Thermal Maps

The SThM results for four flexible graphene devices are discussed in this section. The channel width for all of the devices is 10 μm, and the channel lengths are 10 μm, 10 μm, 25 μm, and 30 μm. Before SThM measurements, the graphene channels and metal lines are annealed by passing a DC current. The applied electrical bias is increased and decreased repeatedly until there is no change in the obtained IV curves.

Figure 4.9 shows the SThM measurements results for a 25 x 10 μm^2 graphene channel with a power dissipation density of 1276 W cm^{-2}. The thermovoltage maps in the contact and lift modes and their difference are shown. The heated area in the flexible device extends laterally more than SiO_2/Si devices.[27,28,30] In particular, large temperature rises occur on the exposed polyimide surface surrounding the graphene channel. A smaller heated area was found previously in a graphene device made on a SiO_2/Si substrate because the large thermal conductivity of the Si substrate below the 300 nm top SiO_2 layer effectively set the SiO_2/Si interface temperature to be close to the ambient

temperature. Figure 4.10 shows the temperature profile along the centerline of two graphene channels for a range of power dissipation densities. The temperature rise for these flexible devices is much higher than temperature rise in the graphene devices on SiO_2/Si substrates with a similar lateral dimension and under a similar power density.[27-30,105]

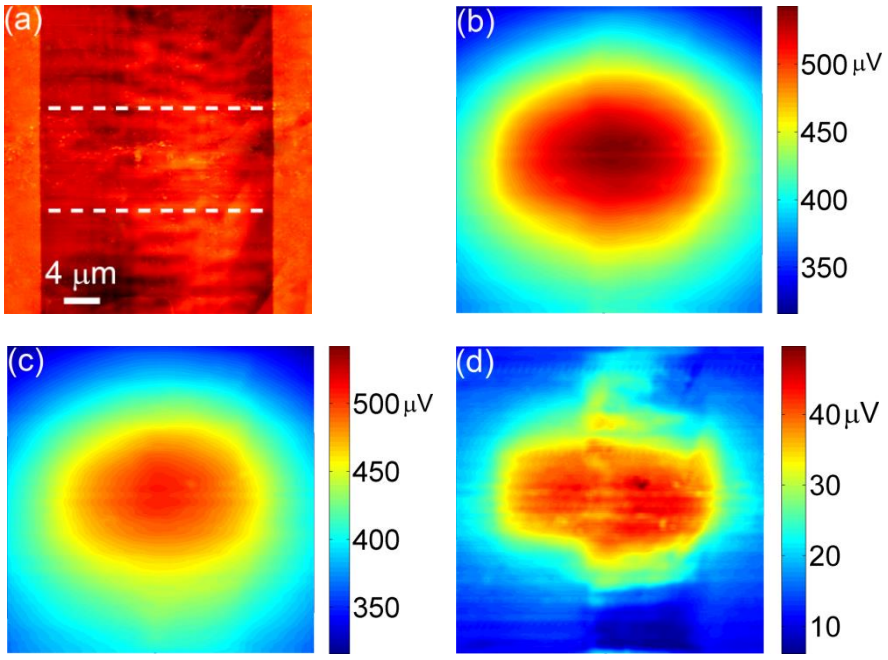

Figure 4.9: SThM measurement results for a 25 x 10 μm^2 graphene channel with a power dissipation density of 1276 W cm^{-2}. Topography (a), thermovoltage map in contact mode (b), and thermovoltage map when the tip is lifted 1 μm above the device surface (c) are shown. Panel (d) shows the difference between (b) and (c). In (a), graphene is located between the dashed lines. The electrical bias is applied to the left metal line, and the right metal line is grounded.

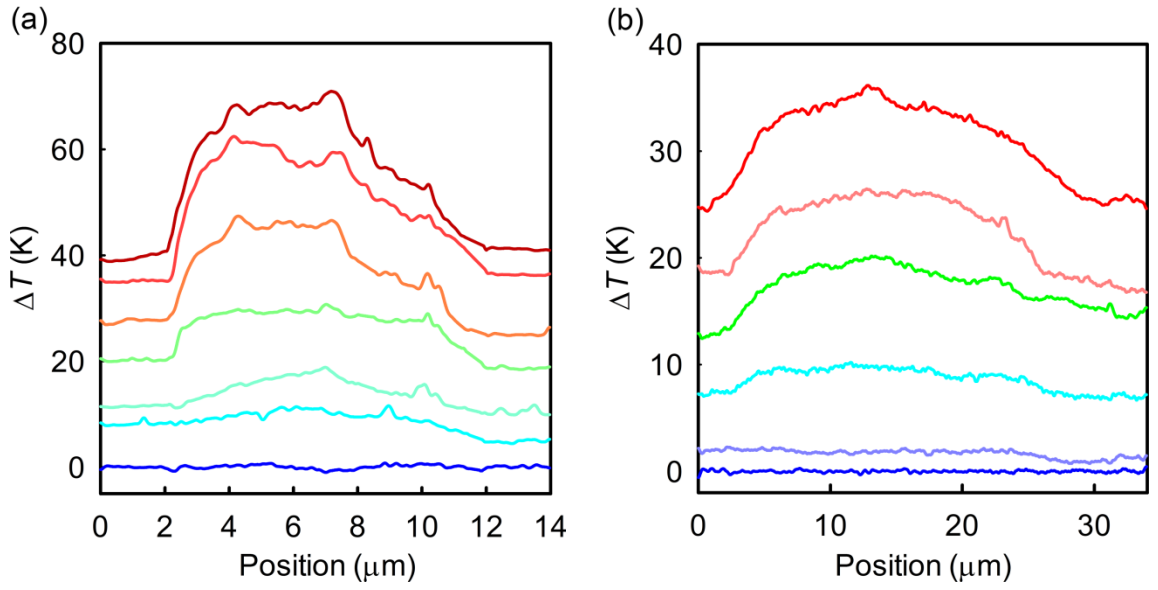

Figure 4.10: Measured temperature profile along the centerline of the 10 x 10 μm^2 (a) and 30 x 10 μm^2 (b) graphene channels. The biased and grounded electrodes are located on the left and right ends, respectively, with a width of 2 μm (a) and 2.7 μm (b). The measured temperature rise increases with increasing power dissipation density of 0, 305, 497, 760, 1425, 1787, and 2044 W cm^{-2} for (a) and 0, 23, 141, 311, 398, and 650 W cm^{-2} for (b).

The higher temperature in the flexible device is caused by the lower thermal conductivity of polyimide compared to SiO_2 and Si. Because of the high thermal conductance of the metal electrodes, the temperature rise measured on top of the metal contacts is lower than that measured on the graphene channel. As the power density increases, the peak temperature moves from the middle of the channel toward the positively biased source contact. This observation reveals that the local carrier density and conductivity near the grounded drain electrode become higher than those near the

source electrode when the positive bias applied to the source electrode is increased. This phenomenon can occur when the Fermi level is above the Dirac point so that the graphene channel is n-type.

4.3.6 Substrate and Channel Size Effects

The low thermal conductivity of the flexible devices increases the hot spot intensity compared to the SiO_2/Si devices and modifies the heat dissipation pathway. Figure 4.11 shows the average resistance ($\overline{R}$) for heat dissipation, defined as the ratio of average temperature rise to power dissipation density, in the flexible devices and other reports for graphene on Si substrates with 300 nm thick SiO_2.

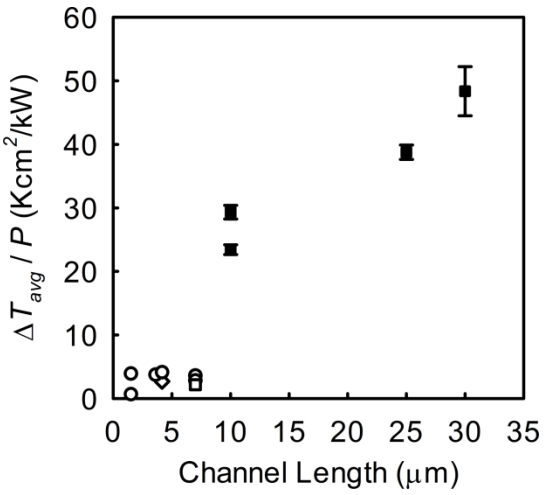

Figure 4.11: The ratio of average temperature rise to power dissipation density as a function of channel length for flexible graphene samples (filled squares). Also shown for comparison are the results for graphene samples on the Si substrate covered with 300 nm SiO_2 measured by SThM (unfilled square),[30] infrared emission thermometry (unfilled diamond),[27] and Raman thermometry (unfilled circles)[27,29,30,105].

In graphene/SiO_2/Si devices, $\overline{R}$ is measured with different thermometry methods to be ~3 K cm ^{2} kW $^{-1}$ irrespective of the channel length in the range of 1.5 and 7 μm,[27,29,30,105] because the main pathway for heat dissipation is across the SiO_2 layer toward the high thermal conductivity Si substrate. In comparison, in the current flexible devices, $\overline{R}$ is found to be larger by more than one order of magnitude and depends on the channel length.

4.4 SUMMARY

This chapter has reported an investigation of a SThM measurement technique for quantitative thermal imaging with a sub-100 nm spatial resolution. It was shown that the temperature jump in the thermocouple by the heat conduction via the liquid meniscus at the tip-device interface can be measured via multiple SThM scans at different tip-sample distances and calibrated to obtain quantitative temperature distribution of the device. The spatial resolution of the thermal imaging technique is expected to be comparable to the size of the liquid meniscus at the tip-sample contact. The effect of sample temperature variation on interpreting SThM measurements and tip-sample heat transfer was investigated. Variations of the heat transfer through the liquid meniscus with temperature can significantly distort the measurement results when the average temperature of the meniscus is higher than 80 ^{o}C. Below this temperature, the calibration factor was measured to be nearly constant regardless of the changes in the capillary force.

We also developed laser-heated SThM, an active SThM technique that enables direct measurement of the temperature at a single point on a device. The method does not rely on the heat transfer between the tip and the device and can measure local

temperature without any calibration, which provides a facile approach to interpret SThM measurements. Laser-heated SThM was employed to measure the temperature of a graphene device on a polyimide substrate and found consistent results with the calibrated SThM approach.

Through the use of calibrated SThM measurements, high-resolution temperature maps in graphene devices supported on flexible polyimide substrates were obtained. The peak temperature at low power dissipation rates was found to be at the center of the graphene channels, and moved toward the positively biased source contact by increasing the bias. Compared to Si devices with 300 nm SiO_2 where the temperature rise is found to be insensitive to the lateral sample size, the average temperature rise in flexible graphene devices was found to be higher by more than one order of magnitude and depends on the size of the graphene channel. These findings help to quantify the effects of the low thermal conductivity of the polyimide substrate.

Chapter 5: Conclusion

5.1 SUMMARY

This work aims to further the current understanding of nanoscale thermal transport in graphene which plays an important role in the design of future graphene-based devices. Thermal transport in graphene was investigated by conducting experimental and theoretical analyses of the thickness-dependent thermal conductivity in supported multi-layer graphene, developing an experimental approach to study electronic thermal transport in graphene, and performing quantitative scanning thermal microscopy measurements to obtain the temperature distributions in flexible graphene devices with a high spatial resolution.

The thermal conductivity of several multi-layer graphene samples supported on SiO_2 was measured using suspended micro-thermometer devices to investigate how the thermal conductivity evolves by increasing thickness from two-dimensional graphene to three-dimensional graphite. A steady state comparative method was employed to measure the thermal conductivity of the graphite source used for exfoliating the graphene samples. In addition, a measurement technique was introduced for the analysis of micro-thermometer devices with non-symmetric designs that were optimized to improve measurement accuracy. The measurement results show that the room-temperature thermal conductivity of multi-layer graphene increases gradually with increasing thickness and has not fully recovered to the graphite value even after the thickness increases to 34 layers. Based on detailed investigation of mechanisms for the suppression of the thermal conductivity in supported graphene, it was shown that the observed thermal conductivity

suppression even in relatively thick supported multi-layer graphene is caused by the long intrinsic mean free path of both in-plane and cross-plane phonons and partially diffuse scattering at the interface with the adjacent amorphous layer. This phenomenon was clarified by a theoretical model based on a solution of phonon Boltzmann transport equation in the boundary scattering regime. The numerical solution of the theoretical model agrees with the low-temperature measurement results of a 34-layer graphene sample when the top and bottom surfaces are partially diffuse with a specularity parameter of 0.36, or when one surface is diffuse and the other one is specular. It was also found that the peak thermal conductivity shifts to higher temperatures for decreased thickness of multi-layer graphene samples. This phenomenon was explained based on the decreased mean free path of phonons for thinner graphene samples because of partially-diffuse scattering of phonons at the interface.

An experimental method was explored to investigate electronic thermal transport in graphene and other layered materials under an applied longitudinal temperature gradient in the presence of applied electric and magnetic fields. Suspended micro-thermometer devices were fabricated to measure the longitudinal and transverse components of the thermal conductivity, electrical conductivity tensors, thermoelectric power tensors, and investigate thermogalvanomagnetic effects. The measurement method was tested for a bilayer graphene sample without the use of an applied gate field. The measurement results showed no clear dependence of longitudinal thermal conductivity and transverse thermal conductivity to the applied magnetic field. The result is indicative of negligible contribution of electrons to thermal conductivity of graphene when the charge carrier concentration is low without the application of a gate field. In comparison,

the Seebeck coefficient was found to be strongly suppressed by the applied magnetic field. Based on these results, suspended micro-thermometer devices were fabricated to incorporate a back-gate to tune the carrier concentration of graphene with the field effect.

Furthermore, a quantitative scanning thermal microscopy (SThM) technique was developed and employed to map the temperature distribution in flexible graphene devices with a sub-100 nm spatial resolution. The challenge of eliminating parasitic signal via the air conduction from the SThM measurement results was addressed by employing a triple scan technique to obtain the temperature jump in the thermocouple via the heat conduction through the liquid meniscus and solid-solid contact at the tip-sample junction. The thermovoltage jump was calibrated using calibration measurements on a resistance-thermometer metal line. The effectiveness of the calibration method was discussed and variability of the obtained calibration factor was investigated by measuring temperature-dependence of the thermal resistance of the liquid meniscus. It was found that, despite the expected changes in the shape of the liquid meniscus and measured variations in the capillary force, the thermal resistance of the liquid meniscus remains unchanged when the average temperature of meniscus is increased from room temperature up to 80 ºC. At this point, the thermal resistance starts to gradually increase with increasing temperature and after an abrupt jump at 110 ºC, increases appreciably with increasing temperature. Such analysis on thermal resistance of the liquid meniscus helps to better understand the applicability and accuracy of the SThM measurements that rely on the tip-sample heat transfer.

Laser-heated SThM was developed to enable direct measurement of the local temperature. The method is based on variable heating of the SThM probe by the incident

laser of the AFM. The local temperature is obtained from the measured tip temperature when the tip-sample heat transfer is zero. Such approach that does not rely on the tip-device heat transfer offers a robust method for calibration of SThM measurements especially where variations of surface chemistry and the effect of tip on local temperature is a concern.

Calibrated SThM measurements were employed to study temperature distribution in flexible graphene devices on polyimide substrates. It was found that the average temperature rise on the flexible graphene devices is more than one order of magnitude larger than graphene devices on silicon substrate with 300 nm SiO_2 and comparable power dissipation density. The peak temperature was found at the center of the graphene channels, and moved toward the biased source by increasing the positive voltage bias. The measurement results were verified by laser-heated SThM measurements at the center of a graphene channel.

5.2 FUTURE WORKS

Despite the wealth of progress in the field of nanoscale thermal transport over the past two decades including this contribution, there remains a number of outstanding questions. The experimental and theoretical approaches presented in this work can be used to advance current understanding. Further investigation is needed to study the size effects on thermal transport and thermoelectric properties of other layered materials that are being actively explored for future nanoelectronic devices and other applications. Similarly, the effect of material and surface properties of the substrate on thermal transport in supported layered materials remains to be studied. Moreover, further research

to perform magneto-thermal measurements on graphene and other layered materials in a case where electronic thermal transport can be modulated would enable direct measurement of electronic thermal conductivity. Furthermore, more research is needed to investigate thermal management in flexible devices with channel lengths comparable to the channel length in state-of-the-art transistors. Possible topics to study include effectiveness of underlying heat spreading layers, lateral thermal cross talk between adjacent transistors, and effects of ballistic transport of electrons and phonons.

Appendix A: Finite Element Analysis of Micro-Thermometer Devices

We used three-dimensional finite element models of the micro-thermometer devices to investigate the accuracy of the measurement method via systematic errors caused by neglecting thermal contact resistances and thermal resistance of the substrate, and the assumption of uniform temperature across the thickness of the supporting SiO_2 beam. Comsol Multiphysics software was used to perform the simulations. Figure A.1 shows the temperature distribution of the G34 device with uniform heat generation in one of the resistance-thermometers. Modeling the micro-thermometer devices with nanometer-thick graphene samples leads to simulations with extremely large number of nodes beyond the software capability. To avoid this issue in these simulations, the graphene samples were modeled as thin film solids with equivalent thermal conductance values. The thickness and thermal conductivity values were increased and decreased, respectively, by a scaling factor. We used the Wiedemann-Franz law[77] to determine the thermal conductivity of the thin film metals from the measured electrical resistance values of the metal lines in the actual devices. Temperature-dependent thermal conductivity of SiO_2 was taken from the literature,[135] which was consistent with the measured thermal conductivity of the SiO_2 bridge after removing graphene in current measurements. The thermal interface resistance for graphene/SiO_2,[44,72,73] Au/Cr/graphene,[44,136] Au/Cr/SiO_2,[136-138] and Si/SiO_2[137] interfaces were included in the simulation.

To evaluate the accuracy of the measurements, simulations were performed in the temperature range of 40-300 K with and without including the thermal resistances at the

interfaces. We followed the experimental approach to obtain the thermal conductance of the central bridge of the device based on the average temperature rise of the resistance-thermometers and heat generation of the heater(s). Uniform heat generation in a metal line established temperature gradients along the central bridge and the resistance-thermometers. The average temperature rises of the resistance-thermometers were obtained from the simulation results, and as described in sections 2.2.1 and 2.2.2, were used to obtain the temperature rise at the midpoint of the metal line for each resistance-thermometer, and subsequently the thermal conductance of the bridge. The obtained thermal conductance was compared to the thermal conductance of the bridge based on the dimensions and thermal conductivity of the materials. With the use of the largest thermal interface resistance value reported for different graphene samples, as well as the lowest reported cross-plane thermal conductivity and the highest reported in-plane thermal conductivity of graphite at different temperatures,[32] the largest relative uncertainty is found in sample G27 at 100 K, where the basal-plane thermal conductivity is underestimated by no more than 9%.

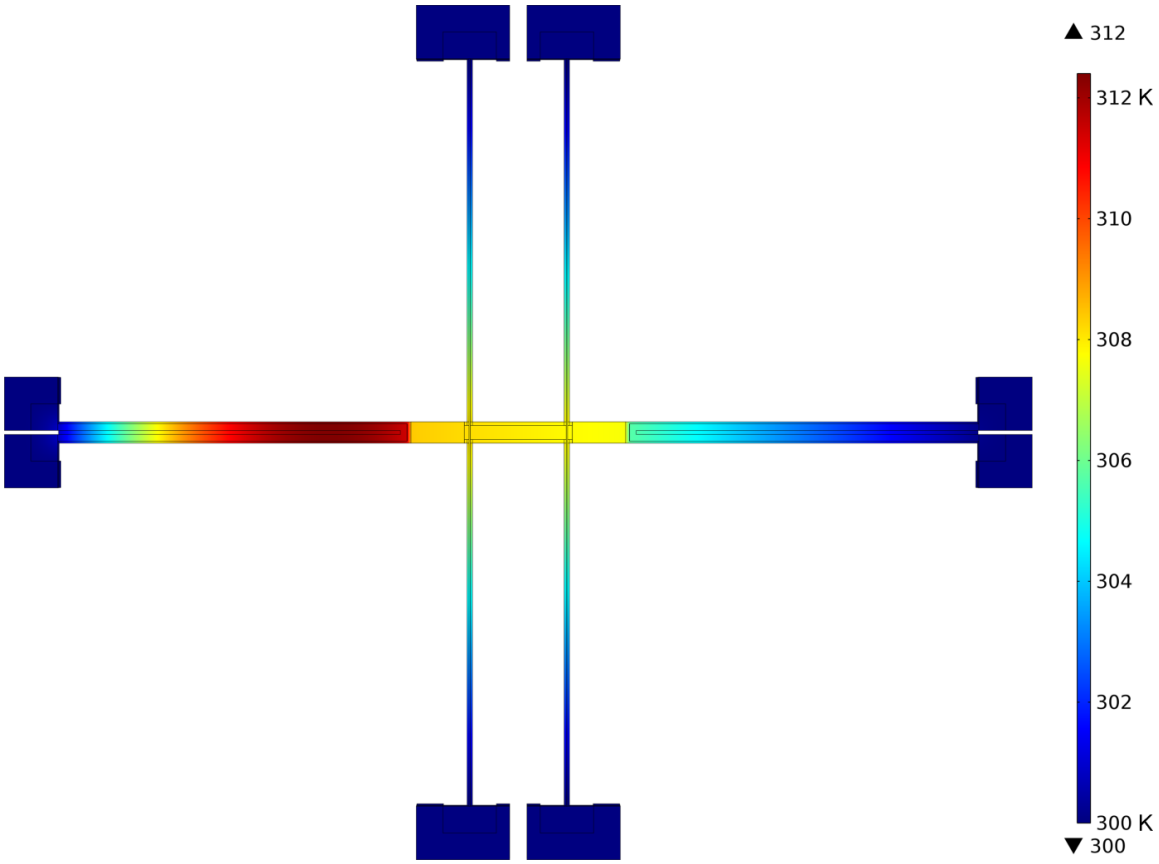

Figure A.1: Temperature distribution in G34 device at room temperature obtained by three-dimensional simulation of heat conduction in the device while there is a uniform heat generation in the left U-shape resistance-thermometer.

Appendix B: Phonon Dispersion of Graphite

The phonon dispersion of graphite was calculated with the use of *ab initio* calculation package QUANTUM ESPRESSO,[67] which performs calculations based on density functional perturbation theory. Generalized gradient approximation, ultrasoft pseudopotentials, and plane-wave basis set were used in the self-consistent calculations.[139] Lattice constants of $a = 2.458$ Å and $c = 6.701$ Å, and a wavefunction cut-off of 60 Ryd results in the convergence of energy calculated over a 8 x 8 x 4 Monkhorst-Pack grid in the Brillouin zone. Subsequently, the dynamical matrices on a 5 x 5 x 4 grid of phonon q-vectors were obtained, and the inter-atomic force constants in real space were calculated. The phonon frequencies for any arbitrary phonon vector were determined through Fourier interpolation.

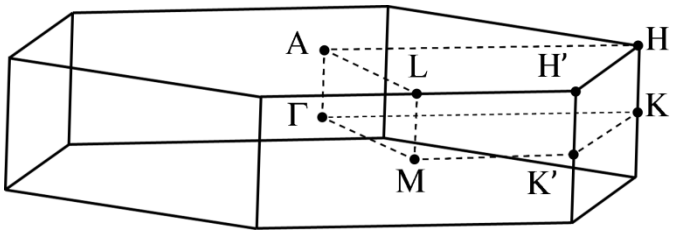

Figure B.1: Schematic illustrations of the Brillouin zone of graphite (solid line) and the prism ΓMK′KALH′H (dashed lines) over which phonon dispersion calculations are performed.

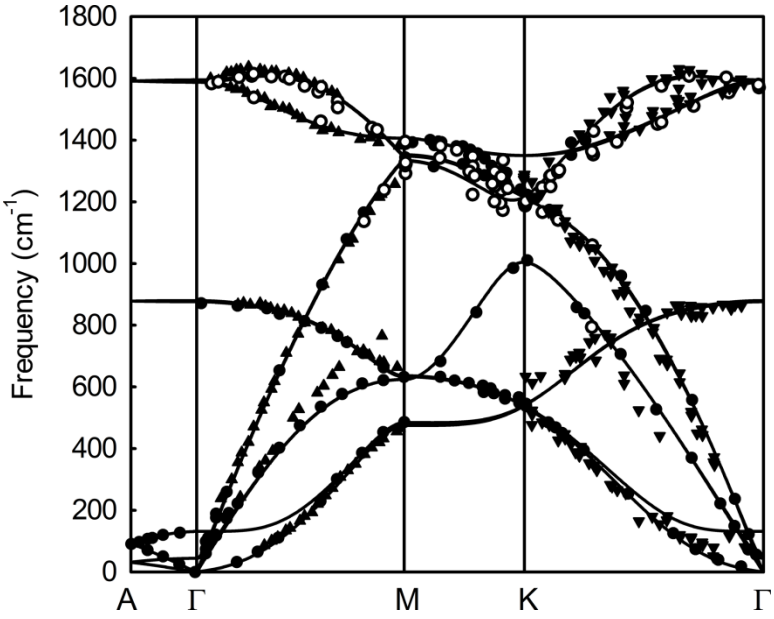

Figure B.2: The calculated phonon dispersion of graphite (solid line). Also shown for comparison are the experimental data based on inelastic x-ray scattering (filled circles[140] and unfilled circles[141]) and electron energy-loss spectroscopy (triangles[142] and inverted triangles[143]).

The phonon dispersion calculation was carried out over 1/8th of the Brillouin zone, which is the prism ΓMK′KALH′H shown in Figure B.1. The full phonon dispersion over the entire Brillouin zone was obtained based on symmetry. The calculation grid consists of 291984 grid points with 116, 101, and 33 grid points along ΓK, ΓM, and ΓA directions, respectively. At each grid point, 12 frequencies were obtained from the calculation with QUANTUM ESPRESSO. For each specific direction in the Brillouin zone parallel to ΓK, ΓM, and ΓA directions, these frequencies were assigned to different phonon branches by maximizing the smoothness of the phonon dispersion curves. For all phonon modes, components of group velocity parallel to ΓK, ΓM, and ΓA directions were

calculated numerically. The calculated phonon dispersion relations are in excellent agreement with reported calculations[139] and experimental results shown in Figure B.2.

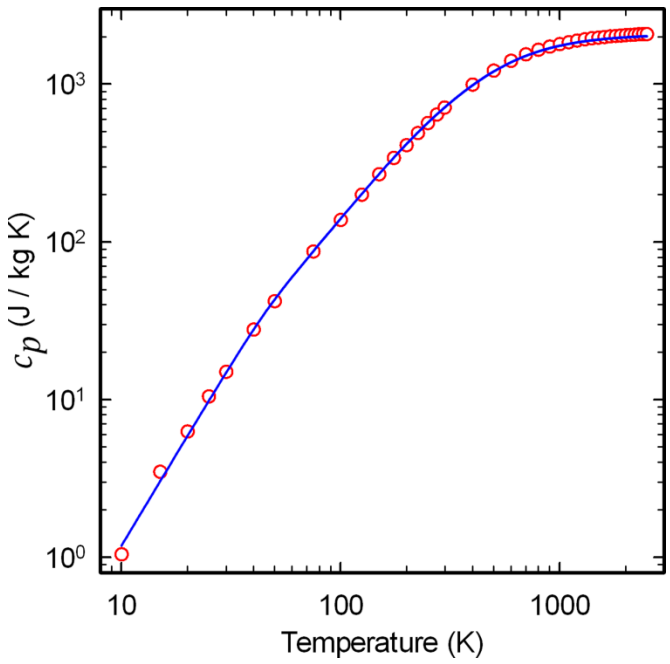

Figure B.3: The calculated specific heat of graphite (blue solid line) in comparison with the values recommended in ref. 144 (red unfilled circles).

Based on the calculated phonon dispersion over the entire Brillouin zone, the specific heat of graphite is calculated based on

$$c_p = \sum_p \sum_{\vec{k}} k_B \, x^2 \, \frac{e^x}{(e^x - 1)^2} \, \frac{\Delta k^3}{8\pi^3} \quad , \qquad x \equiv \hbar\omega / k_B T \tag{B-1}$$

where the summations are over all phonon polarizations (p) wave vector ($\vec{k}$) states in the discretized Brillouin zone, Δk^3 is the volume of the element associated with each grid point within the discretized Brillouin zone, $\hbar$ is the reduced Planck constant, ω is the angular frequency, k_B is the Boltzmann constant, and T is the temperature. As shown in Figure B.3, the calculated specific heat is in agreement with the reported specific heat of graphite over the entire temperature range.

References

1 Cahill, D. G., Ford, W. K., Goodson, K. E., Mahan, G. D., Majumdar, A., Maris, H. J., Merlin, R. & Sr, P. Nanoscale Thermal Transport. *J Appl Phys* **93**, 793-818 (2003).

2 Baxter, J. *et al.* Nanoscale Design to Enable the Revolution in Renewable Energy. *Energ Environ Sci* **2**, 559-588 (2009).

3 Cahill, D. G. *et al.* Nanoscale Thermal Transport. II. 2003-2012. *Appl Phys Rev* **1**, 011305 (2014).

4 Shi, L. *et al.* Evaluating Broader Impacts of Nanoscale Thermal Transport Research. *Nanosc Microsc Therm* **19**, 127-165 (2015).

5 Pop, E., Sinha, S. & Goodson, K. E. Heat Generation and Transport in Nanometer-Scale Transistors. *P IEEE* **94**, 1587-1601 (2006).

6 Shakouri, A. Nanoscale Thermal Transport and Microrefrigerators on a Chip. *P IEEE* **94**, 1613-1638 (2006).

7 Pop, E. Energy Dissipation and Transport in Nanoscale Devices. *Nano Res* **3**, 147-169 (2010).

8 Novoselov, K. S., Geim, A. K., Morozov, S. V., Jiang, D., Zhang, Y., Dubonos, S. V., Grigorieva, I. V. & Firsov, A. A. Electric Field Effect in Atomically Thin Carbon Films. *Science* **306**, 666-669 (2004).

9 Geim, A. K. Graphene: Status and Prospects. *Science* **324**, 1530-1534 (2009).

10 Geim, A. K. & Novoselov, K. S. The Rise of Graphene. *Nat Mater* **6**, 183-191 (2007).

11 Schwierz, F. Graphene Transistors. *Nat Nanotechnol* **5**, 487-496 (2010).

12 Lee, C., Wei, X. D., Kysar, J. W. & Hone, J. Measurement of the Elastic Properties and Intrinsic Strength of Monolayer Graphene. *Science* **321**, 385-388 (2008).

13 Liu, F., Ming, P. M. & Li, J. Ab Initio Calculation of Ideal Strength and Phonon Instability of Graphene under Tension. *Phys Rev B* **76**, 064120 (2007).

14 Balandin, A. A. Thermal Properties of Graphene and Nanostructured Carbon Materials. *Nat Mater* **10**, 569-581 (2011).

15 Lindsay, L., Broido, D. A. & Mingo, N. Flexural Phonons and Thermal Transport in Multilayer Graphene and Graphite. *Phys Rev B* **83**, 235428 (2011).

16 Novoselov, K. S., Fal'ko, V. I., Colombo, L., Gellert, P. R., Schwab, M. G. & Kim, K. A Roadmap for Graphene. *Nature* **490**, 192-200 (2012).

17 Seol, J. H. *et al.* Two-Dimensional Phonon Transport in Supported Graphene. *Science* **328**, 213-216 (2010).

18 Pettes, M. T., Jo, I. S., Yao, Z. & Shi, L. Influence of Polymeric Residue on the Thermal Conductivity of Suspended Bilayer Graphene. *Nano Lett* **11**, 1195-1200 (2011).

19 Jang, W. Y., Chen, Z., Bao, W. Z., Lau, C. N. & Dames, C. Thickness-Dependent Thermal Conductivity of Encased Graphene and Ultrathin Graphite. *Nano Lett* **10**, 3909-3913 (2010).

20 Gabor, N. M., Song, J. C. W., Ma, Q., Nair, N. L., Taychatanapat, T., Watanabe, K., Taniguchi, T., Levitov, L. S. & Jarillo-Herrero, P. Hot Carrier-Assisted Intrinsic Photoresponse in Graphene. *Science* **334**, 648-652 (2011).

21 Song, J. C. W., Rudner, M. S., Marcus, C. M. & Levitov, L. S. Hot Carrier Transport and Photocurrent Response in Graphene. *Nano Lett* **11**, 4688-4692 (2011).

22 Kim, K. S. *et al.* Large-Scale Pattern Growth of Graphene Films for Stretchable Transparent Electrodes. *Nature* **457**, 706-710 (2009).

23 Bae, S. *et al.* Roll-to-Roll Production of 30-Inch Graphene Films for Transparent Electrodes. *Nat Nanotechnol* **5**, 574-578 (2010).

24 Akinwande, D., Petrone, N. & Hone, J. Two-Dimensional Flexible Nanoelectronics. *Nat Commun* **5**, 5678 (2014).

25 Cahill, D. G., Goodson, K. E. & Majumdar, A. Thermometry and Thermal Transport in Micro/Nanoscale Solid-State Devices and Structures. *J Heat Trans-T ASME* **124**, 223-241 (2002).

26 Shi, L., Zhou, J. H., Kim, P., Bachtold, A., Majumdar, A. & McEuen, P. L. Thermal Probing of Energy Dissipation in Current-Carrying Carbon Nanotubes. *J Appl Phys* **105**, 104306 (2009).

27 Freitag, M., Chiu, H. Y., Steiner, M., Perebeinos, V. & Avouris, P. Thermal Infrared Emission from Biased Graphene. *Nat Nanotechnol* **5**, 497-501 (2010).

28 Bae, M. H., Ong, Z. Y., Estrada, D. & Pop, E. Imaging, Simulation, and Electrostatic Control of Power Dissipation in Graphene Devices. *Nano Lett* **10**, 4787-4793 (2010).

29 Berciaud, S., Han, M. Y., Mak, K. F., Brus, L. E., Kim, P. & Heinz, T. F. Electron and Optical Phonon Temperatures in Electrically Biased Graphene. *Phys Rev Lett* **104**, 227401 (2010).

30 Jo, I. *et al.* Low-Frequency Acoustic Phonon Temperature Distribution in Electrically Biased Graphene. *Nano Lett* **11**, 85-90 (2011).

31 Slack, G. A. Anisotropic Thermal Conductivity of Pyrolytic Graphite. *Phys Rev* **127**, 694-701 (1962).

32 Touloukian, Y. S., Powell, R. W., Ho, C. Y. & Klemens, P. G. *Thermophysical Properties of Matter*. Vol. 2 (IFI/Plenum, 1970).

33 Klemens, P. G. & Pedraza, D. F. Thermal-Conductivity of Graphite in the Basal-Plane. *Carbon* **32**, 735-741 (1994).

34 Baughman, R. H., Zakhidov, A. A. & de Heer, W. A. Carbon Nanotubes - The Route toward Applications. *Science* **297**, 787-792 (2002).

35 Tien, C. L., Majumdar, A. & Gerner, F. M. *Microscale Energy Transport*. (Taylor & Francis, 1997).

36 Kim, P., Shi, L., Majumdar, A. & McEuen, P. L. Thermal Transport Measurements of Individual Multiwalled Nanotubes. *Phys Rev Lett* **87**, 215502 (2001).

37 Ghosh, S., Bao, W. Z., Nika, D. L., Subrina, S., Pokatilov, E. P., Lau, C. N. & Balandin, A. A. Dimensional Crossover of Thermal Transport in Few-Layer Graphene. *Nat Mater* **9**, 555-558 (2010).

38 Marconnet, A. M., Panzer, M. A. & Goodson, K. E. Thermal Conduction Phenomena in Carbon Nanotubes and Related Nanostructured Materials. *Rev Mod Phys* **85**, 1295-1326 (2013).

39 Lindsay, L., Broido, D. A. & Mingo, N. Flexural Phonons and Thermal Transport in Graphene. *Phys Rev B* **82**, 115427 (2010).

40 Klemens, P. G. Theory of Thermal Conduction in Thin Ceramic Films. *Int J Thermophys* **22**, 265-275 (2001).

41 Ong, Z. Y. & Pop, E. Effect of Substrate Modes on Thermal Transport in Supported Graphene. *Phys Rev B* **84**, 075471 (2011).

42 Qiu, B. & Ruan, X. L. Reduction of Spectral Phonon Relaxation Times from Suspended to Supported Graphene. *Appl Phys Lett* **100**, 193101 (2012).

43 Chen, J., Zhang, G. & Li, B. W. Substrate Coupling Suppresses Size Dependence of Thermal Conductivity in Supported Graphene. *Nanoscale* **5**, 532-536 (2013).

44 Sadeghi, M. M., Pettes, M. T. & Shi, L. Thermal Transport in Graphene. *Solid State Communications* **152**, 1321-1330 (2012).

45 Ong, Z. Y., Pop, E. & Shiomi, J. Reduction of Phonon Lifetimes and Thermal Conductivity of a Carbon Nanotube on Amorphous Silica. *Phys Rev B* **84**, 165418 (2011).

46 Seol, J. H., Moore, A. L., Shi, L., Jo, I. & Yao, Z. Thermal Conductivity Measurement of Graphene Exfoliated on Silicon Dioxide. *J Heat Trans-T ASME* **133**, 022403 (2011).

47 Blake, P., Hill, E. W., Castro Neto, A. H., Novoselov, K. S., Jiang, D., Yang, R., Booth, T. J. & Geim, A. K. Making Graphene Visible. *Appl Phys Lett* **91**, 063124 (2007).

48 Ferrari, A. C. *et al.* Raman Spectrum of Graphene and Graphene Layers. *Phys Rev Lett* **97**, 187401 (2006).

49 Hao, Y. F., Wang, Y. Y., Wang, L., Ni, Z. H., Wang, Z. Q., Wang, R., Koo, C. K., Shen, Z. X. & Thong, J. T. L. Probing Layer Number and Stacking Order of Few-Layer Graphene by Raman Spectroscopy. *Small* **6**, 195-200 (2010).

50 Graf, D., Molitor, F., Ensslin, K., Stampfer, C., Jungen, A., Hierold, C. & Wirtz, L. Spatially Resolved Raman Spectroscopy of Single- and Few-Layer Graphene. *Nano Lett* **7**, 238-242 (2007).

51 Wang, Y. Y., Ni, Z. H., Shen, Z. X., Wang, H. M. & Wu, Y. H. Interference Enhancement of Raman Signal of Graphene. *Appl Phys Lett* **92**, 043121 (2008).

52 Meyer, J. C., Geim, A. K., Katsnelson, M. I., Novoselov, K. S., Booth, T. J. & Roth, S. The Structure of Suspended Graphene Sheets. *Nature* **446**, 60-63 (2007).

53 Incropera, F. P. & DeWitt, D. P. *Fundamentals of Heat and Mass Transfer*. 5th edn, (Wiley, 2002).

54 Ferrari, A. C. Raman Spectroscopy of Graphene and Graphite: Disorder, Electron-Phonon Coupling, Doping and Nonadiabatic Effects. *Solid State Communications* **143**, 47-57 (2007).

55 Jo, I., Pettes, M. T., Kim, J., Watanabe, K., Taniguchi, T., Yao, Z. & Shi, L. Thermal Conductivity and Phonon Transport in Suspended Few-Layer Hexagonal Boron Nitride. *Nano Lett* **13**, 550-554 (2013).

56 Koenig, S. P., Boddeti, N. G., Dunn, M. L. & Bunch, J. S. Ultrastrong Adhesion of Graphene Membranes. *Nat Nanotechnol* **6**, 543-546 (2011).

57 Aizawa, T., Souda, R., Ishizawa, Y., Hirano, H., Yamada, T., Tanaka, K. I. & Oshima, C. Phonon-Dispersion in Monolayer Graphite Formed on Ni(111) and Ni(001). *Surface Science* **237**, 194-202 (1990).

58 Shikin, A. M., Farias, D., Adamchuk, V. K. & Rieder, K. H. Surface Phonon Dispersion of a Graphite Monolayer Adsorbed on Ni(111) and Its Modification Caused by Intercalation of Yb, La and Cu Layers. *Surface Science* **424**, 155-167 (1999).

59 Wu, M. C., Xu, Q. & Goodman, D. W. Investigations of Graphitic Overlayers Formed from Methane Decomposition on Ru(0001) and Ru(1120) Catalysts with Scanning-Tunneling-Microscopy and High-Resolution Electron-Energy-Loss Spectroscopy. *Journal of Physical Chemistry* **98**, 5104-5110 (1994).

60 Farias, D., Rieder, K. H., Shikin, A. M., Adamchuk, V. K., Tanaka, T. & Oshima, C. Modification of the Surface Phonon Dispersion of a Graphite Monolayer Adsorbed on Ni(111) Caused by Intercalation of Yb, Cu and Ag. *Surface Science* **454**, 437-441 (2000).

61 Aizawa, T., Hwang, Y., Hayami, W., Souda, R., Otani, S. & Ishizawa, Y. Phonon-Dispersion of Monolayer Graphite on Pt(111) and Nbc Surfaces - Bond Softening and Interface Structures. *Surface Science* **260**, 311-318 (1992).

62 Yoon, T., Shin, W. C., Kim, T. Y., Mun, J. H., Kim, T. S. & Cho, B. J. Direct Measurement of Adhesion Energy of Monolayer Graphene as-Grown on Copper and Its Application to Renewable Transfer Process. *Nano Lett* **12**, 1448-1452 (2012).

63 Cullen, W. G., Yamamoto, M., Burson, K. M., Chen, J. H., Jang, C., Li, L., Fuhrer, M. S. & Williams, E. D. High-Fidelity Conformation of Graphene to SiO_2 Topographic Features. *Phys Rev Lett* **105**, 215504 (2010).

64 Lui, C. H., Liu, L., Mak, K. F., Flynn, G. W. & Heinz, T. F. Ultraflat Graphene. *Nature* **462**, 339-341 (2009).

65 Locatelli, A. *et al.* Corrugation in Exfoliated Graphene: An Electron Microscopy and Diffraction Study. *Acs Nano* **4**, 4879-4889 (2010).

66 Prasher, R. Acoustic Mismatch Model for Thermal Contact Resistance of Van Der Waals Contacts. *Appl Phys Lett* **94**, 041905 (2009).

67 Giannozzi, P. *et al.* Quantum Espresso: A Modular and Open-Source Software Project for Quantum Simulations of Materials. *J Phys-Condens Mat* **21**, 395502 (2009).

68 Shen, M., Schelling, P. K. & Keblinski, P. Heat Transfer Mechanism across Few-Layer Graphene by Molecular Dynamics. *Phys Rev B* **88**, 045444 (2013).

69 Klemens, P. G. Theory of the a-Plane Thermal Conductivity of Graphite. *Journal of Wide Bandgap Materials* **7**, 332-339 (2000).

70 Chen, G. *Nanoscale Energy Transport and Conversion : A Parallel Treatment of Electrons, Molecules, Phonons, and Photons*. (Oxford University Press, 2005).

71 Prasher, R. Thermal Boundary Resistance and Thermal Conductivity of Multiwalled Carbon Nanotubes. *Phys Rev B* **77**, 075424 (2008).

72 Mak, K. F., Lui, C. H. & Heinz, T. F. Measurement of the Thermal Conductance of the Graphene/SiO_2 Interface. *Appl Phys Lett* **97**, 221904 (2010).

73 Chen, Z., Jang, W., Bao, W., Lau, C. N. & Dames, C. Thermal Contact Resistance between Graphene and Silicon Dioxide. *Appl Phys Lett* **95**, 161910 (2009).

74 Ziman, J. M. *Electrons and Phonons : The Theory of Transport Phenomena in Solids*. (Clarendon Press, 1960).

75 McCurdy, A. K., Maris, H. J. & Elbaum, C. Anisotropic Heat Conduction in Cubic Crystals in the Boundary Scattering Regime. *Phys Rev B* **2**, 4077-4083 (1970).

76 Chen, G. Size and Interface Effects on Thermal Conductivity of Superlattices and Periodic Thin-Film Structures. *J Heat Trans-T ASME* **119**, 220-229 (1997).

77 Ashcroft, N. W. & Mermin, N. D. *Solid State Physics*. (Holt, 1976).

78 Chester, G. & Thellung, A. The Law of Wiedemann and Franz. *Proceedings of the Physical Society* **77**, 1005 (1961).

79 Pettes, M. T., Maassen, J., Jo, I., Lundstrom, M. S. & Shi, L. Effects of Surface Band Bending and Scattering on Thermoelectric Transport in Suspended Bismuth Telluride Nanoplates. *Nano Lett* **13**, 5316-5322 (2013).

80 Huang, B. L. & Kaviany, M. Ab Initio and Molecular Dynamics Predictions for Electron and Phonon Transport in Bismuth Telluride. *Phys Rev B* **77**, 125209 (2008).

81 Goldsmid, H. J. *Introduction to Thermoelectricity*. (Springer, 2010).

82 Stojanovic, N., Maithripala, D. H. S., Berg, J. M. & Holtz, M. Thermal Conductivity in Metallic Nanostructures at High Temperature: Electrons, Phonons, and the Wiedemann-Franz Law. *Phys Rev B* **82**, 075418 (2010).

83 Kane, C. L. & Fisher, M. P. A. Thermal Transport in a Luttinger Liquid. *Phys Rev Lett* **76**, 3192-3195 (1996).

84 Fazio, R., Hekking, F. W. J. & Khmelnitskii, D. E. Anomalous Thermal Transport in Quantum Wires. *Phys Rev Lett* **80**, 5611-5614 (1998).

85 Krive, I. V. Thermal Transport through Luttinger Liquid Constriction. *Low Temp Phys+* **24**, 377-379 (1998).

86 Bachtold, A., de Jonge, M., Grove-Rasmussen, K., McEuen, P. L., Buitelaar, M. & Schonenberger, C. Suppression of Tunneling into Multiwall Carbon Nanotubes. *Phys Rev Lett* **87**, 166801 (2001).

87 Bockrath, M., Cobden, D. H., Lu, J., Rinzler, A. G., Smalley, R. E., Balents, L. & McEuen, P. L. Luttinger-Liquid Behaviour in Carbon Nanotubes. *Nature* **397**, 598-601 (1999).

88 Kanda, A., Tsukagoshi, K., Aoyagi, Y. & Ootuka, Y. Gate-Voltage Dependence of Zero-Bias Anomalies in Multiwall Carbon Nanotubes. *Phys Rev Lett* **92**, 036801 (2004).

89 Yao, Z., Postma, H. W. C., Balents, L. & Dekker, C. Carbon Nanotube Intramolecular Junctions. *Nature* **402**, 273-276 (1999).

90 Ou, M. N., Yang, T. J., Harutyunyan, S. R., Chen, Y. Y., Chen, C. D. & Lai, S. J. Electrical and Thermal Transport in Single Nickel Nanowire. *Appl Phys Lett* **92**, 063101 (2008).

91 Vavilov, M. G. & Stone, A. D. Failure of the Wiedemann-Franz Law in Mesoscopic Conductors. *Phys Rev B* **72**, 205107 (2005).

92 Peres, N. M. R., dos Santos, J. M. B. L. & Stauber, T. Phenomenological Study of the Electronic Transport Coefficients of Graphene. *Phys Rev B* **76**, 073412 (2007).

93 Dora, B. & Thalmeier, P. Magnetotransport and Thermoelectricity in Landau-Quantized Disordered Graphene. *Phys Rev B* **76**, 035402 (2007).

94 Li, M. R. & Orignac, E. Heat Conduction and Wiedemann-Franz Law in Disordered Luttinger Liquids. *Europhys Lett* **60**, 432-438 (2002).

95 Pop, E., Varshney, V. & Roy, A. K. Thermal Properties of Graphene: Fundamentals and Applications. *Mrs Bull* **37**, 1273-1281 (2012).

96 Saito, K., Nakamura, J. & Natori, A. Ballistic Thermal Conductance of a Graphene Sheet. *Phys Rev B* **76**, 115409 (2007).

97 Abrosimov, V. M., Egorov, B. N., Lidorenko, N. S. & Karandashev, V. A. Dimensional Effect of Transfer-Coefficients in Oriented Films of Bismuth Grown on Polymer Substrates. *High Temp+* **12**, 456-461 (1974).

98 Volklein, F. & Kessler, E. A Method for the Measurement of Thermal-Conductivity, Thermal-Diffusivity, and Other Transport-Coefficients of Thin-Films. *Phys Status Solidi A* **81**, 585-596 (1984).

99 Zhang, Y. B., Tan, Y. W., Stormer, H. L. & Kim, P. Experimental Observation of the Quantum Hall Effect and Berry's Phase in Graphene. *Nature* **438**, 201-204 (2005).

100 Zhang, Y., Ong, N. P., Xu, Z. A., Krishana, K., Gagnon, R. & Taillefer, L. Determining the Wiedemann-Franz Ratio from the Thermal Hall Conductivity: Application to Cu and $YBa_2Cu_3O_{6.95}$. *Phys Rev Lett* **84**, 2219-2222 (2000).

101 Uher, C. & Goldsmid, H. J. Separation of the Electronic and Lattice Thermal Conductivities in Bismuth Crystals. *Phys Status Solidi B* **65**, 765-772 (1974).

102 Rogacheva, E. I., Grigorov, S. N., Nashchekina, O. N., Lyubchenko, S. & Dresselhaus, M. S. Quantum-Size Effects in N-Type Bismuth Thin Films. *Appl Phys Lett* **82**, 2628-2630 (2003).

103 Cheng, Z. G., Zhou, Q. Y., Wang, C. X., Li, Q. A., Wang, C. & Fang, Y. Toward Intrinsic Graphene Surfaces: A Systematic Study on Thermal Annealing and Wet-Chemical Treatment of SiO_2-Supported Graphene Devices. *Nano Lett* **11**, 767-771 (2011).

104 Kim, S., Jo, I., Nah, J., Yao, Z., Banerjee, S. K. & Tutuc, E. Coulomb Drag of Massless Fermions in Graphene. *Phys Rev B* **83**, 161401 (2011).

105 Chae, D. H., Krauss, B., von Klitzing, K. & Smet, J. H. Hot Phonons in an Electrically Biased Graphene Constriction. *Nano Lett* **10**, 466-471 (2010).

106 Faugeras, C., Faugeras, B., Orlita, M., Potemski, M., Nair, R. R. & Geim, A. K. Thermal Conductivity of Graphene in Corbino Membrane Geometry. *Acs Nano* **4**, 1889-1892 (2010).

107 Calizo, I., Miao, F., Bao, W., Lau, C. N. & Balandin, A. A. Variable Temperature Raman Microscopy as a Nanometrology Tool for Graphene Layers and Graphene-Based Devices. *Appl Phys Lett* **91**, 071913 (2007).

108 Freitag, M., Steiner, M., Martin, Y., Perebeinos, V., Chen, Z. H., Tsang, J. C. & Avouris, P. Energy Dissipation in Graphene Field-Effect Transistors. *Nano Lett* **9**, 1883-1888 (2009).

109 Majumdar, A. Scanning Thermal Microscopy. *Annu Rev Mater Sci* **29**, 505-585 (1999).

110 Shi, L. & Majumdar, A. Thermal Transport Mechanisms at Nanoscale Point Contacts. *J Heat Trans-T ASME* **124**, 329-337 (2002).

111 Yu, Y. J., Han, M. Y., Berciaud, S., Georgescu, A. B., Heinz, T. F., Brus, L. E., Kim, K. S. & Kim, P. High-Resolution Spatial Mapping of the Temperature Distribution of a Joule Self-Heated Graphene Nanoribbon. *Appl Phys Lett* **99**, 183105 (2011).

112 Pumarol, M. E., Rosamond, M. C., Tovee, P., Petty, M. C., Zeze, D. A., Falko, V. & Kolosov, O. V. Direct Nanoscale Imaging of Ballistic and Diffusive Thermal Transport in Graphene Nanostructures. *Nano Lett* **12**, 2906-2911 (2012).

113 Menges, F., Riel, H., Stemmer, A., Dimitrakopoulos, C. & Gotsmann, B. Thermal Transport into Graphene through Nanoscopic Contacts. *Phys Rev Lett* **111**, 205901 (2013).

114 Grosse, K. L., Bae, M. H., Lian, F. F., Pop, E. & King, W. P. Nanoscale Joule Heating, Peltier Cooling and Current Crowding at Graphene-Metal Contacts. *Nat Nanotechnol* **6**, 287-290 (2011).

115 Grosse, K. L., Dorgan, V. E., Estrada, D., Wood, J. D., Vlassiouk, I., Eres, G., Lyding, J. W., King, W. P. & Pop, E. Direct Observation of Resistive Heating at Graphene Wrinkles and Grain Boundaries. *Appl Phys Lett* **105**, 143109 (2014).

116 Kim, K., Jeong, W. H., Lee, W. C. & Reddy, P. Ultra-High Vacuum Scanning Thermal Microscopy for Nanometer Resolution Quantitative Thermometry. *Acs Nano* **6**, 4248-4257 (2012).

117 Luo, K., Shi, Z., Varesi, J. & Majumdar, A. Sensor Nanofabrication, Performance, and Conduction Mechanisms in Scanning Thermal Microscopy. *J Vac Sci Technol B* **15**, 349-360 (1997).

118 Menges, F., Riel, H., Stemmer, A. & Gotsmann, B. Quantitative Thermometry of Nanoscale Hot Spots. *Nano Lett* **12**, 596-601 (2012).

119 Kim, K., Chung, J., Won, J., Kwon, O., Lee, J. S., Park, S. H. & Choi, Y. K. Quantitative Scanning Thermal Microscopy Using Double Scan Technique. *Appl Phys Lett* **93**, 203115 (2008).

120 Kim, K., Chung, J., Hwang, G., Kwon, O. & Lee, J. S. Quantitative Measurement with Scanning Thermal Microscope by Preventing the Distortion Due to the Heat Transfer through the Air. *Acs Nano* **5**, 8700-8709 (2011).

121 Shi, L., Plyasunov, S., Bachtold, A., McEuen, P. L. & Majumdar, A. Scanning Thermal Microscopy of Carbon Nanotubes Using Batch-Fabricated Probes. *Appl Phys Lett* **77**, 4295-4297 (2000).

122 Shi, L., Kwon, O., Miner, A. C. & Majumdar, A. Design and Batch Fabrication of Probes for Sub-100 nm Scanning Thermal Microscopy. *J Microelectromech S* **10**, 370-378 (2001).

123 Lee, J., Ha, T. J., Li, H. F., Parrish, K. N., Holt, M., Dodabalapur, A., Ruoff, R. S. & Akinwande, D. 25 Ghz Embedded-Gate Graphene Transistors with High-K Dielectrics on Extremely Flexible Plastic Sheets. *Acs Nano* **7**, 7744-7750 (2013).

124 Li, X. S. *et al.* Large-Area Synthesis of High-Quality and Uniform Graphene Films on Copper Foils. *Science* **324**, 1312-1314 (2009).

125 Johnson, K., Kendall, K. & Roberts, A. Surface Energy and the Contact of Elastic Solids. *Proc. R. Soc. Lond. A* **324**, 301-313 (1971).

126 Butt, H. J. & Kappl, M. Normal Capillary Forces. *Adv Colloid Interfac* **146**, 48-60 (2009).

127 Gomes, S., Trannoy, N. & Grossel, P. Dc Thermal Microscopy: Study of the Thermal Exchange between a Probe and a Sample. *Meas Sci Technol* **10**, 805-811 (1999).

128 Osborne III, K. L. *Temperature-Dependence of the Contact Angle of Water on Graphite, Silicon, and Gold*, Worcester Polytechnic Institute, (2009).

129 Rafiee, J., Mi, X., Gullapalli, H., Thomas, A. V., Yavari, F., Shi, Y. F., Ajayan, P. M. & Koratkar, N. A. Wetting Transparency of Graphene. *Nat Mater* **11**, 217-222 (2012).

130 Shih, C. J., Wang, Q. H., Lin, S. C., Park, K. C., Jin, Z., Strano, M. S. & Blankschtein, D. Breakdown in the Wetting Transparency of Graphene. *Phys Rev Lett* **109**, 176101 (2012).

131 Ishigami, M., Chen, J. H., Cullen, W. G., Fuhrer, M. S. & Williams, E. D. Atomic Structure of Graphene on SiO_2. *Nano Lett* **7**, 1643-1648 (2007).

132 Lin, Y. C., Jin, C. H., Lee, J. C., Jen, S. F., Suenaga, K. & Chiu, P. W. Clean Transfer of Graphene for Isolation and Suspension. *Acs Nano* **5**, 2362-2368 (2011).

133 Nakabeppu, O. & Suzuki, T. Microscale Temperature Measurement by Scanning Thermal Microscopy. *J Therm Anal Calorim* **69**, 727-737 (2002).

134 Chung, J., Kim, K., Hwang, G., Kwon, O., Jung, S., Lee, J., Lee, J. W. & Kim, G. T. Quantitative Temperature Measurement of an Electrically Heated Carbon Nanotube Using the Null-Point Method. *Rev Sci Instrum* **81**, 114901 (2010).

135 Cahill, D. G., Bullen, A. & Lee, S. M. Interface Thermal Conductance and the Thermal Conductivity of Multilayer Thin Films. *High Temp-High Press* **32**, 135-142 (2000).

136 Koh, Y. K., Bae, M. H., Cahill, D. G. & Pop, E. Heat Conduction across Monolayer and Few-Layer Graphenes. *Nano Lett* **10**, 4363-4368 (2010).

137 Kading, O. W., Skurk, H. & Goodson, K. E. Thermal Conduction in Metallized Silicon-Dioxide Layers on Silicon. *Appl Phys Lett* **65**, 1629-1631 (1994).

138 Chien, H. C., Yao, D. J., Huang, M. J. & Chang, T. Y. Thermal Conductivity Measurement and Interface Thermal Resistance Estimation Using SiO_2 Thin Film. *Rev Sci Instrum* **79**, 054902 (2008).

139 Mounet, N. & Marzari, N. First-Principles Determination of the Structural, Vibrational and Thermodynamic Properties of Diamond, Graphite, and Derivatives. *Phys Rev B* **71**, 205214 (2005).

140 Mohr, M., Maultzsch, J., Dobardzic, E., Reich, S., Milosevic, I., Damnjanovic, M., Bosak, A., Krisch, M. & Thomsen, C. Phonon Dispersion of Graphite by Inelastic X-Ray Scattering. *Phys Rev B* **76**, 035439 (2007).

141 Maultzsch, J., Reich, S., Thomsen, C., Requardt, H. & Ordejon, P. Phonon Dispersion in Graphite. *Phys Rev Lett* **92**, 075501 (2004).

142 Oshima, C., Aizawa, T., Souda, R., Ishizawa, Y. & Sumiyoshi, Y. Surface Phonon-Dispersion Curves of Graphite(0001) over the Entire Energy Region. *Solid State Communications* **65**, 1601-1604 (1988).

143 Siebentritt, S., Pues, R., Rieder, K. H. & Shikin, A. M. Surface Phonon Dispersion in Graphite and in a Lanthanum Graphite Intercalation Compound. *Phys Rev B* **55**, 7927-7934 (1997).

144 Hultgren, R. R. & Wagman, D. D. *Selected Values of the Thermodynamic Properties of the Elements*. (American Society for Metals, 1973).